The Dissertation Committee for Michael Louis Kuntzman Certifies that this is the approved version of the following dissertation:

Micromachined In-Plane Acoustic Pressure Gradient Sensors

Committee:

Neal A. Hall, Supervisor

Craig A. Champlin

Mircea D. Driga

Mark F. Hamilton

Dean P. Neikirk

Micromachined In-Plane Acoustic Pressure Gradient Sensors

by

Michael Louis Kuntzman, B.S.; M.S.E.

Dissertation

Presented to the Faculty of the Graduate School of

The University of Texas at Austin

in Partial Fulfillment

of the Requirements

for the Degree of

Doctor of Philosophy

The University of Texas at Austin

May 2014

Dedication

I dedicate this dissertation to my parents, siblings, and friends who have supported me throughout the duration of this work.

Acknowledgements

I would like to thank, first and foremost, my adviser, Neal Hall. I feel privileged to have had the opportunity to study under him. He has consistently challenged me and offered insight into new ways to approach problems. He has also believed in me when, at times, I did not believe in myself. I would like to thank all of the other members of our research team whom I have had the opportunity to work with, particularly Nishshanka Hewa-Kasakarage, Donghwan Kim, Karen Kirk, and Manzur Rahman. I would like to thank the undergraduate researchers whom I have had the opportunity to mentor over the last several years, Gloria Lee, Jonathon Kuntzman, and Alex Roche. I would like to thank Silicon Audio, particularly Ceasar Garcia, Brad Avenson, and Guchlu Oranan, for their support and mentorship. I would like to thank the faculty of the UT Acoustics program, particularly Elmer Hixson for his support and mentorship early in my graduate career.

Additionally, I would also like to thank Donghwan Kim for his help with the generation of the CAD images in Figures 4.3, 6.1, 6.8, and 8.1, Irene Roderick and Douglas Winker for supporting me with the Elmer L. Hixer Endowed Graduate Fellowship in Acoustical Engineering, and DARPA for funding this research.

I would like to thank the friends I have made during my years in Austin, particularly my bandmates Justin Finney, Patrick Boyce, Dolores Diaz, Shelby DuPerier, and Brady Porche. You have been an invaluable source of support and comradeship. I would also like to thank the other close friends that have been supportive throughout my graduate career: Aale Navi, Ariel Sauceda, Aparna Sripada, Jason McDowell, Jonathan Wafford, and Connie Fuhrman.

I would also like to thank my undergraduate adviser, Mahfuza Khatun, without whom I never would have made it this far, as well as the many other professors who I have considered an inspiration along the way.

Last but perhaps most importantly, I would like to thank my parents, Wes and Arlene Kuntzman, and my siblings Bethany and Jonathan Kuntzman. You have all been an invaluable source of support and it would have been very difficult to make it this far without you.

Micromachined In-Plane Acoustic Pressure Gradient Sensors

Michael Louis Kuntzman, Ph.D.

The University of Texas at Austin, 2014

Supervisor: Neal A. Hall

Abstract: This work presents the fabrication, modeling, and characterization of two first-generation acoustic in-plane pressure gradient sensors. The first is a micromachined piezoelectric microphone. The microphone structure consists of a semi-rigid beam structure that rotates about torsional pivots in response to in-plane pressure gradients across the length of the beam. The rotation of the beam structure is transduced by piezoelectric cantilevers, which deflect when the beam structure rotates. Sensors with both 10 and 20-μm-thick beam structures are presented. An analytical model and multi-mode, multi-port network model utilizing finite-element analysis for parameter extraction are presented and compared to acoustic sensitivity measurements. Directivity measurements are interpreted in terms of the multi-mode model. A noise model for the sensor and readout electronics is presented and compared to measurements.

The second sensor is a capacitive sensor which is comprised of two vacuum-sealed, pistons coupled to each other by a pivoting beam. The use of a pivoting beam can, in principle, enable high rotational compliance to in-plane small-signal acoustic pressure gradients, while resisting piston collapse against large background atmospheric pressure. A design path towards vacuum-sealed, surface micromachined broadband microphones is a motivation to explore the sensor concept. Fabrication of surface micromachined prototypes is presented, followed by finite element modeling and experimental

confirmation of successful vacuum-sealing. Dynamic frequency response measurements are obtained using broadband electrostatic actuation and confirm a first fundamental rocking mode near 250 kHz. Successful reception of airborne ultrasound in air at 130 kHz is also demonstrated, and followed by a discussion of design paths toward improve signal-to-noise ratio beyond that of the initial prototypes presented.

A method of localizing sound sources is demonstrated using the piezoelectric sensor. The localization method utilizes the multiple-port nature of the sensor to simultaneously extract the pressure gradient and pressure magnitude components of the incoming acoustic signal. An algorithm for calculating the sound source location from the pressure gradient and pressure magnitude measurement is developed. The method is verified by acoustic measurements performed at 2 kHz.

Table of Contents

List of Tables

List of Figures

Chapter I: Introduction & Motivation

A. About Silicon Microphones

The first microphones fabricated using silicon micromachining techniques were presented in 1983 [1-4]. Since the first commercial shipment by Knowles Electronics in 2003, the microelectromechanical system (MEMS) microphone market has experienced rapid growth, with global revenue projected to jump from $227M in 2010 to $667M in 2015 and global shipments projected to increase from 700 million units in 2010 to 2.9 billion units by 2015 [5].

Commercial MEMS microphones typically operate using the same capacitive transduction principle as macro-scale capacitive (i.e. condenser) microphones used in professional audio and test & measurement applications since the 1940s [6-10]. Like their macro-scale counterparts, capacitive MEMS microphones consist of a conductive, compliant diaphragm or membrane suspended over a conductive, ideally rigid back plate, as shown in Figure 1.1. A parallel-plate capacitor is formed between the diaphragm and back plate and the change in capacitance that results from motion of the diaphragm can be measured using suitable readout electronics. The gap between the diaphragm and back plate is typically on the order of several microns and the back plate is typically perforated to allow air displaced by the diaphragm motion to escape from the gap between the back plate and diaphragm. A small piercing, often located on the diaphragm, serves as an acoustical high-pass filter which prevents the sensor from responding to fluctuations in ambient pressure, which would otherwise cause the sensitivity to drift as a function of ambient pressure. Several noise sources exist in MEMS microphones, including thermal-mechanical noise introduced by acoustical damping in the system [11] and the noise

associated with the readout electronics. Dominant sources of acoustical damping are the pressure-equalization piercing and back plate perforations [8, 12].

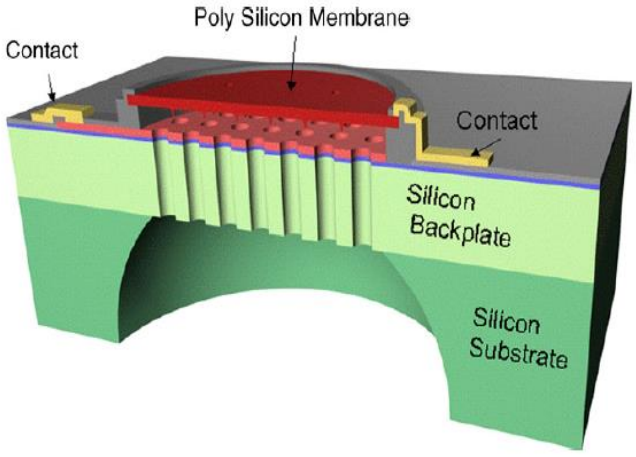

Figure 1.1: Cross section illustration of a MEMS microphone die.
(Adapted from [9] - Used with permission)

B. About Directional microphones

Most currently available MEMS microphones are omnidirectional. However, directional microphones have been shown to improve speech clarity in noisy environments [13-16] and are beneficial in source localization applications [17-19]. Directional microphones are very commonly used in professional audio applications to selectively amplify instruments and vocalists when multiple sound sources exist in close proximity and are of interest in mobile devices to improve background noise rejection [9]. One commonly-used method of obtaining directionality is to use two or more omnidirectional microphones to sample the pressure at two or more points in space and to calculate the pressure gradient by taking the difference signal between the sensors. There are several drawbacks to this approach.

(i) Mismatch in the sensitivity of the sensors will result in error in the measurement.

(ii) The difference signal between the sensors can be very small, so the noise of each sensor must be extremely low.

(iii) The requirement of multiple sensors is costly in terms of required footprint and the cost of the sensors themselves.

To illustrate the requirement for ultra-low noise when this approach is used, consider two omnidirectional microphones separated by a distance, x. The pressure gradient signal between the microphones is $\Delta p = -jkx$, where k is the acoustic wave number. At a frequency of 1 kHz and a spacing of 4 mm, the approximate thickness of a mobile phone, the pressure gradient signal will be 22.7 dB below the acoustic pressure amplitude. Hence, the SNR of the pressure gradient measurement will be 22.7 dB lower than the SNR of the individual microphones. MEMS microphones typically have noise floors in the 30 dBA range, so a total noise in excess of 52 dBA should be expected for a measurement taken using this configuration.

Directional MEMS microphones have been the subject of recent research. Conventional directional microphones consist of a diaphragm that is driven on both sides through ducts separated by some distance, effectively sampling the pressure at two points in space. This method has been applied to MEMS microphones by integrating multiple inlet holes into the package, resulting in directivity pattern that can be varied by altering the number and size of the inlet holes [9]. An innovative, biomimetic approach utilizing an inherently directional sensing structure was developed by Miles et. al, inspired by the hearing mechanism of the fly *Ormia ochracea* [20-22]. The directional sensing structure has inspired optical [23-27], capacitive [28-31], and multi-axis [32, 33] microphone designs. The optical microphone developed by Miles has demonstrated a simultaneous 10-dB lower noise floor and a factor of ten reduction in size compared to state-of-the-art electret condenser microphones (ECMs) used in hearing aid technology [23]. However,

in spite of recent advances in the packaging of optical MEMS microphones [34, 35], challenges still exist to the commercialization of MEMS optical microphone technology.

C. A MICROMACHINED IN-PLANE PRESSURE GRADIENT PIEZOELECTRIC MICROPHONE

The goal of the present work is to explore several novel directional MEMS acoustic sensors [36, 37], which seek to overcome scaling laws which limit the performance of microphones based on traditional macro-scale technology. The first sensor is a piezoelectric microphone [38] inspired by the directional sensing structure developed by Miles et. al. The sensor seeks to integrate the advantages of the inherently directional, biomimetic sensing structure, with the relative simplicity and low cost of piezoelectric MEMS technology as compared to the relatively more complex and costly optical technology. A sketch illustrating the operating principle of the piezoelectric adaptation of the microphone is shown in Figure 1.2. A semi-rigid beam rotates about torsional pivots in response to pressure gradients along the length of the beam. Four piezoelectric cantilever springs with integrated lead zirconate titanate (PZT) thin films transduce the motion of the beam structure. The springs wrap around the side of the device and connect to the end of the rotating structure and hence are referred to in this work as *end-springs*. Figure 1.3 presents labeled micrographs and SEMs of the device. The potential for a low noise sensor results from the structure's high sensitivity to pressure gradients and the reduction in thermal-noise that results from the sensor not requiring a back plate for capacitive sensing.

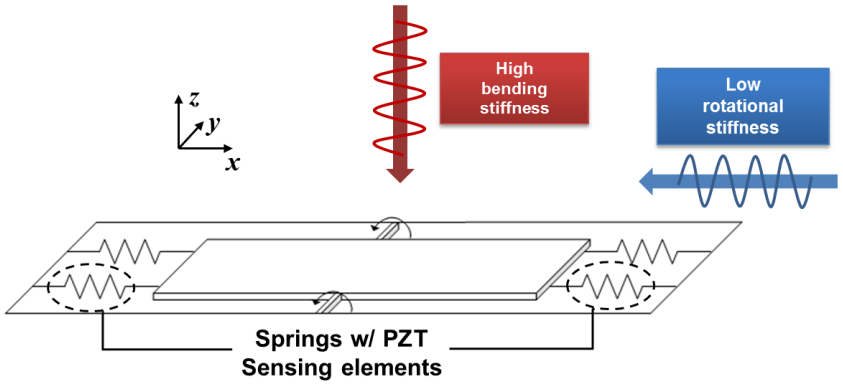

Figure 1.2: Operational schematic of the piezoelectric pressure gradient microphone

It is expected that the piezoelectric version of the microphone will not outperform the optical version with respect to signal-to-noise ratio, but may have the advantage of relatively less complex fabrication and packaging, and as such may be better suited to address high-volume markets where unit cost is critical [7], while potentially maintaining size and performance advantages over current industry solutions. The relative simplicity of the fabrication and packaging compared to other biologically inspired directional microphones [23, 26, 29, 31, 32] may result in a more rapid path to commercialization.

The second sensor is a prototype capacitive, surface-micromachined acoustic pressure gradient sensor which seeks to improve performance beyond what is possible with the piezoelectric microphone, and in that sense, may be considered a future generation of the biologically inspired design. The sensor is a synthesis of the biomimetic sensing structure with capacitive micromachined ultrasound transducer technology (CMUT). This sensor is discussed in Chapter VI.

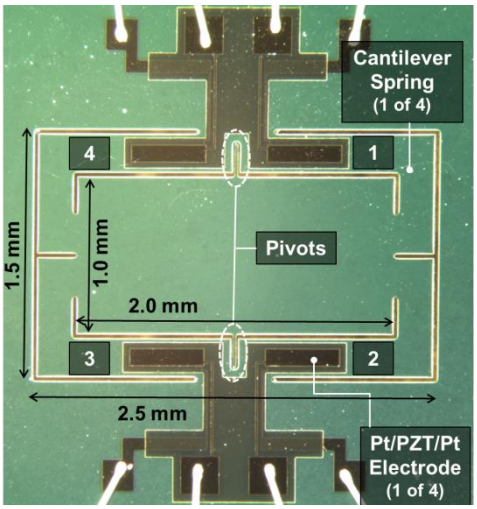

(a)

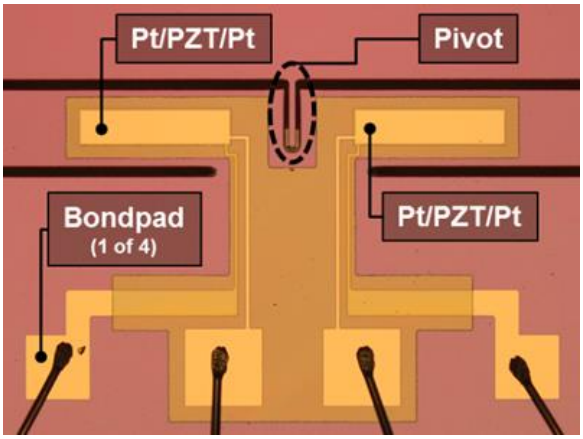

(b)

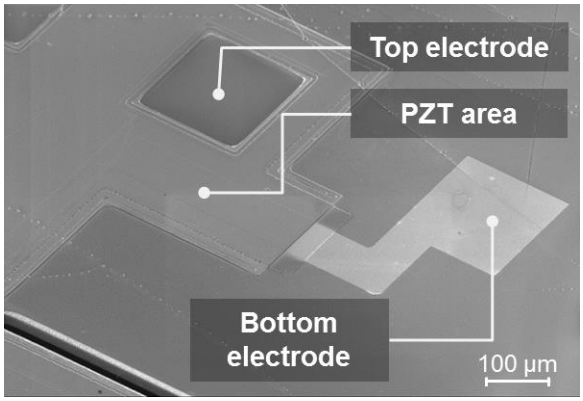

(c)

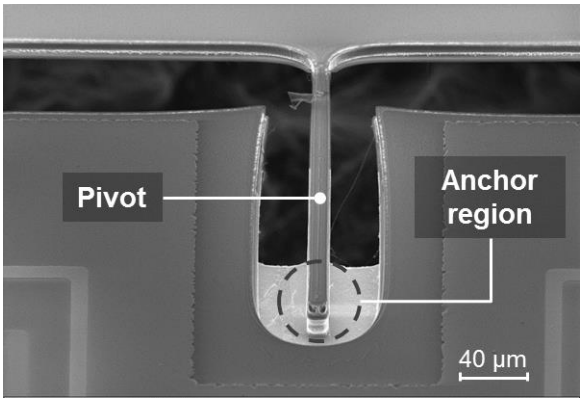

(d)

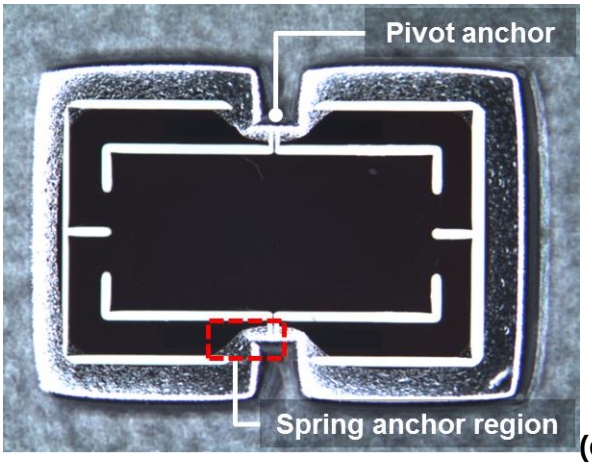

(e)

Figure 1.3: (a) Micrograph of the piezoelectric microphone, (b) micrograph of the pivot and electrode regions, (c) SEM of the bondpad regions, (d) SEM of the pivot region, and (e) micrograph of the through-wafer etch cavity.

Chapter II: Fabrication of the Piezoelectric Microphone

A. The Fabrication Process

The devices were fabricated in the clean room facility at the Microelectronics Research Center (MRC) at the Pickle Research Campus of the University of Texas at Austin. Figure 2.1 illustrates the key steps of the fabrication process, which is the same five-mask fabrication process used for several other devices fabrication by our research team at UT Austin [39-41]. The function of each mask is summarized in Table 2-1. The fabrication process was inspired by previous work in the field of PZT piezoelectric MEMS microphones [42]. The process begins with a 4-inch silicon-on-insulator (SOI) wafer with a 1-μm-thick buried oxide layer. SOI wafers with both 20-μm and 10-μm epitaxial silicon devices layers were used. The wafer is cleaned using a piranha solution before the start of the process. First, 1 μm of silicon oxide is thermally grown at 1050° C, then an additional 3 μm low temperature oxide (LTO) is deposited on both the front and backside of the wafer. The oxide acts as an adhesion layer on the front side and will serve as a hard etch mask during the through wafer etch later in the process. A 180 nm titanium layer is deposited via e-beam evaporation. The titanium layer is then thermally oxidized to form titanium oxide (TiO_x), which acts as a lead diffusion barrier. The bottom electrodes are patterned using Mask #1 with a lift-off process after depositing approximately 120 nm of titanium by DC magnetron sputtering and approximately 40 nm of platinum by RF magnetron sputtering. Micrographs taken after this step are shown in Figure 2.2. The PZT is deposited using a multi-layer sol-gel process, with a ten minute drying step at 450° C and a two minute annealing step at 650° C after each layer. A thirty minute extended annealing step is performed after every two layers. The top electrodes are deposited and patterned with Mask #2 using the same process as the bottom electrodes. A micrograph of a test wafer taken after this step is shown in Figure 2.3. In

this case, the PZT shows some streaking, possibly caused by residue from a previous step remaining on the wafer. The PZT is patterned with Mask #3 using an H_20:HCl:HF = 100:10:1 wet etch solution. A micrograph taken before PZT etch is shown in Figure 2.4, with a measurement of the wet-etch undercut shown in Figure 2.5. In future generations of the design, a dry etch could be used to avoid undercut. The topside of the wafer is patterned using Mask #4 to form the spring and beam structures first etching the TiO_x and SiO_2 using an CHF_3 reactive ion etch (RIE) process, followed by an SF_6 plasma deep silicon etch (DSE) process to etch the silicon device layer, and another CHF_3 plasma RIE process to etch through the buried oxide layer. A micrograph taken after this step is shown in Figure 2.6. A protective photoresist layer is deposited on the topside of the wafer and the backside oxide is pattern using Mask #5 with an RIE process for form a hard mask. A DSE process is then used to etch through the silicon substrate. Remaining photoresist is removed at the end of the process using an O_2 plasma ashing process.

Table 2-1.
Summary of Photolithography Masks

Mask #1	Bottom Electrodes
Mask #2	Top Electrodes
Mask #3	PZT Etch
Mask #4	Device Layer Etch
Mask #5	Handle Wafer Etch

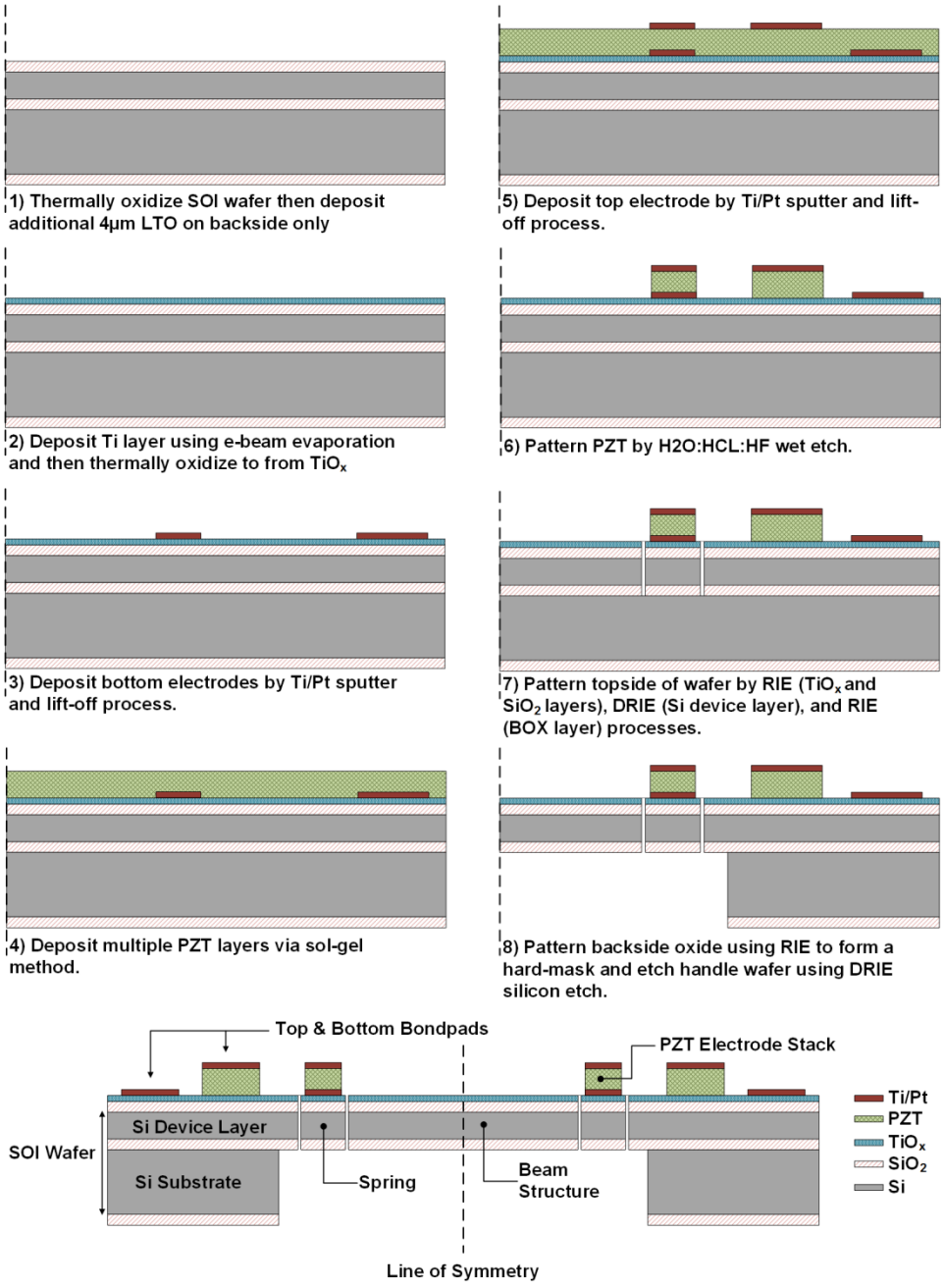

Figure 2.1: Fabrication process flow for the piezoelectric microphone

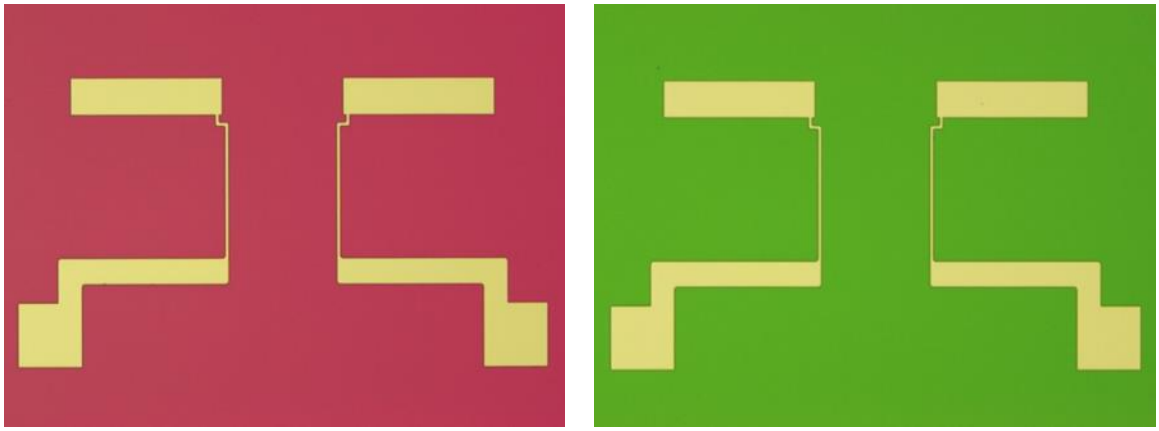

Figure 2.2: Micrographs after bottom electrode lift-off process.

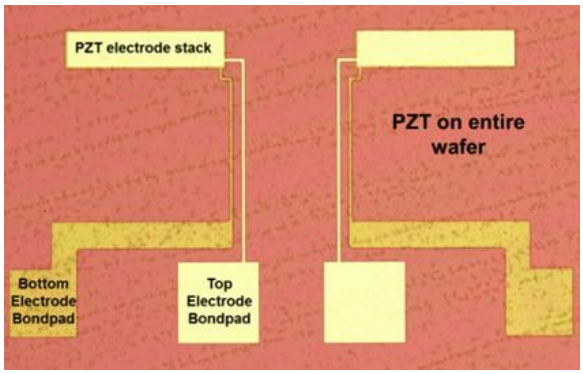

Figure 2.3: Labeled micrograph after top electrode lift-off process.

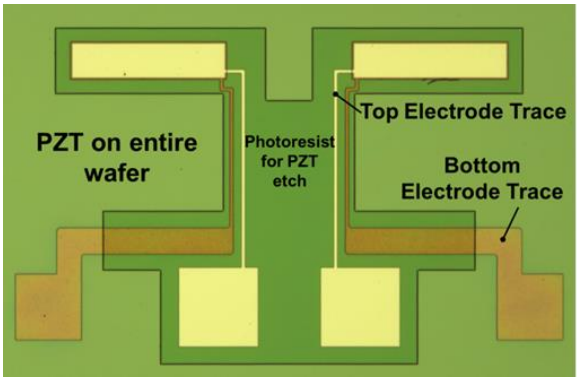

Figure 2.4: Labeled micrograph after PZT etch mask lithography.

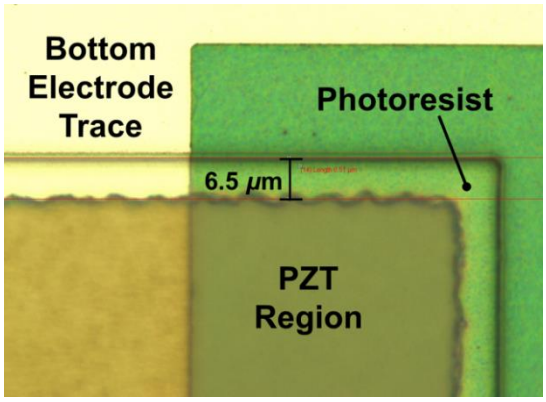

Figure 2.5: Labeled micrograph after PZT etch.

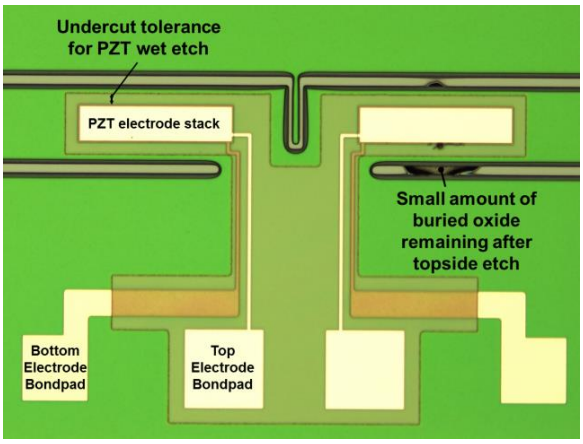

Figure 2.6: Labeled micrograph after topside etch.

B. Fabrication Related Failure Modes

Several potential failure modes of the device were identified during the process of fabricating the devices. Figure 2.7 shows an SEM of a pivot on a device which was over etched. It can be seen that the pivot is too frail and has been fractured near the connection to the beam structure. This was one of the most commonly seen failure modes for the fabricated devices.

Another potential issue is depicted in the SEM shown in Figure 2.8. The PZT layer has relatively high residual tensile stress, which results in the sensing springs tending to bow upwards. If the bowing is sufficiently large, a gap results and acoustic pressure may be equalized on the top and bottom of the beam, resulting lowered acoustic sensitivity. The device in Figure 2.8 was a design variant that included eight piezoelectric cantilever springs. Bowing was not observed to significantly impact the performance of the standard four-springs designs. However, future generations of the device will likely require the use of thinner silicon device layers to maximize compliance and increase sensitivity. For these future devices, it may be necessary to attempt to counteract the stress of the PZT layer by deposition of other layers with stress that tends to act in the opposite manner. For example, oxide tends to have a compressive stress, which would act to the bend the beam downward. By matching the stress of oxide layers deposited on the top of the beam to the stress of the PZT layer, it should be possible to cancel the stress effects and fabricate devices that show little to no bowing. The stress a layer is a function of the layer thickness, deposition temperature, and deposition method. Careful experimentation and optimization of these parameters will likely be necessary for fabrication of future designs. Alternatively, stiffening structures could be integrated into the design to increase the bending stiffness of the beam and counter-act the stress-induced bowing [23].

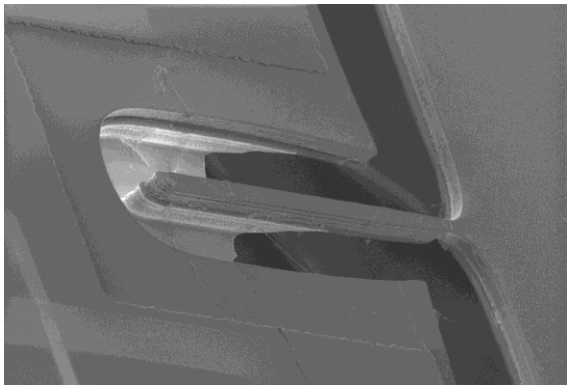

Figure 2.7: SEM of an over etched pivot, showing a fracture which resulted in device failure.

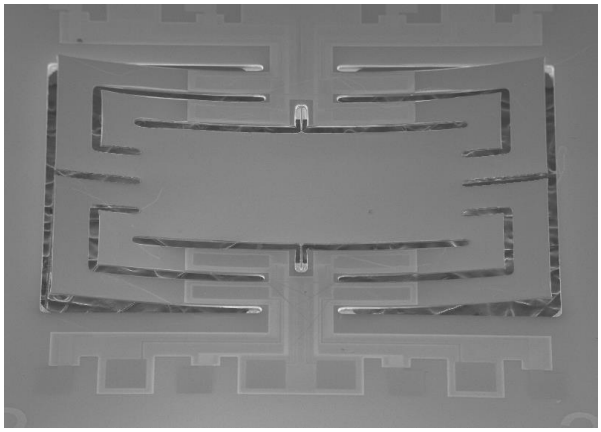

Figure 2.8: An SEM of a device showing bowing due to stress induced by the PZT layer.

Chapter III: Analytical Model for the 1st Mode Sensitivity

The goal of this section is to develop a relatively simple analytical model to estimate the sensitivity of the device based on first principles. It can be useful, particularly during the design phase, to have a purely analytical model for the device sensitivity. For simplicity, the model developed in this chapter takes only the first mode into account. The model developed here will be augmented by a multiple-mode model developed in the next chapter, which offers a more complete description of the device dynamics.

A. FUNDAMENTALS OF PIEZOELECTRICITY

Piezoelectric materials are crystalline materials which exhibit coupling between strain and electric field. An applied strain alters the internal polarization vector of the material and results in the generation of an internal electric field. The generated electric field is the result of internal separation of charge that arises from deformation of the material's non-symmetric crystalline structure. This mechanism is known as the piezoelectric effect. Of the thirty-two crystal classes, twenty-one lack a center of symmetry and are referred to as non-centrosymmetric. Of these twenty-one non-centrosymmetric crystal classes, twenty exhibit the piezoelectric effect. A subclass of piezoelectric material also exhibits the pyroelectric effect. Pyroelectric materials exhibit a change in internal polarization vector when they are heated or cooled, due to expansion or contraction of a non-symmetric crystalline structure. All pyroelectric materials are also piezoelectric, with ten of the twenty piezoelectric crystal classes also exhibiting the pyroelectric effect. A subgroup of pyroelectric materials are also ferroelectric, which means they exhibit a hysteresis-loop relationship between applied electric field and polarization and retain a residual after the removal of an externally applied electric field.

All ferroelectric material are pyroelectric but not all pyroelectric materials are ferroelectric. Common piezoelectric materials used in microfabricated sensors are PZT [42, 43], ZnO [44, 45], AlN [46, 47], and PVDF [48]. Of these materials AlN and ZnO are pyroelectric [49, 50], while PZT and PVDF are both pyroelectric and ferroelectric.

The piezoelectric constitutive equations may be expressed according to IEEE standards [51] as:

$$T_p = c_{pq}^E S_q - e_{kp} E_k \tag{3-1a}$$

$$D_i = e_{iq} S_q + \varepsilon_{ik}^S E_k \tag{3-1b}$$

where c_{pq}^E, e_{kp}, and ε_{ik}^S are elastic, piezoelectric, and dielectric constants, respectively, as noted in Table 3-1. The superscripts E and S indicate the constant is measured under zero electric field (i.e. short-circuit) and zero strain (i.e. clamped) conditions, respectively. The parameters T_p, S_q, E_k, and D_i refer to stress, strain, electric field, and electric displacement, respectively. Subscripts refer to coordinate directions as indicated in Table 3-2.

Table 3-1.
Terms in the Piezoelectric Constitutive Equations

Symbol	Description	Units
T_{ij}	Stress Component	N/m^2
c_{ijkl}^E	Elastic Stiffness constant	N/m^2
S_{kl}	Strain Component	-
e_{kij}	Piezoelectric Constant	C/m^2
E_k	Electric Field Component	V/m
D_i	Electric Displacement Component	C/m^2
ε_{ij}^S	Permittivity Constant	F/m

Table 3-2.
Summary of Index Tensor Notation

Index		Coordinate Direction
i, k	p, q	
1	1	x-direction
2	2	y-direction
3	3	z-direction
-	4	rotation about x-axis
-	5	rotation about y-axis
-	6	rotation about z-axis

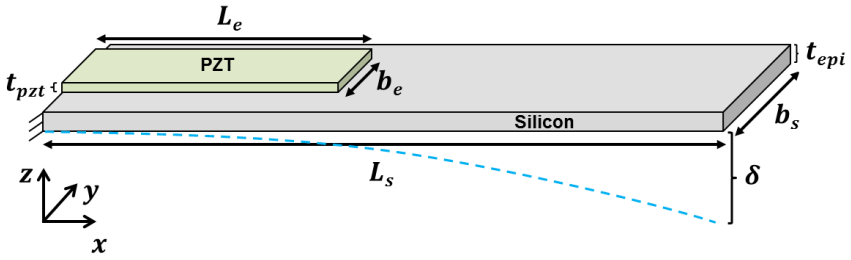

Figure 3.1: An end-spring modeled as a cantilever beam.

B. Transduction Factor and Electrical Sensitivity

A cantilever beam with a thin piezoelectric film over a portion of its surface is depicted in Figure 3.1. As the tip of the cantilever beam deflects, the film has non-zero strain in the 1 and 3 directions and non-zero stress in the 1 and 2-directions. Stress and strain in all other directions are zero. In the short-circuit condition (i.e. $E_3 = 0$), equations (3-1a) & (3-1b) become:

$$0 = c_{31}^{E} S_1 + c_{33}^{E} S_3 \tag{3-2a}$$

$$D_3 = e_{31} S_1 + e_{33} S_3 \tag{3-2b}$$

Solving equations (3-2a) and (3-2b) for D_3 in terms of S_1 yields:

$$D_3 = \left[e_{31} - \frac{e_{33}c_{31}^E}{c_{33}^E}\right] S_1 = e_{31f} S_1 \tag{3-3}$$

The transduction factor for a cantilever beam with a thin-piezoelectric film can be defined as the short-circuit charge resulting for a given tip displacement, which, using the results of equation (3-3), may be expressed as:

$$\phi \equiv \frac{q}{\delta}\Big]_{SC} = \frac{1}{\delta}\int D_3 dA = \frac{b_e}{\delta}\int_0^{L_e} S_1 e_{31f} dx \tag{3-4}$$

where SC refers to the short-circuit case in which charge is allowed to flow between the electrodes to counteract the internally generated electric field, q is the generated charge density $[C/m^2]$ on each electrode, and δ is the tip displacement of the beam. All other geometric variables are defined in Figure 3.1. The strain at the top surface of the beam is given by $S_1 = \frac{t_{epi}}{2}\frac{\partial^2 u}{\partial x^2}$, where t_{epi} is the beam thickness and $u(x)$ is the deflection profile of the beam. The deflection profile of a cantilever beam can be derived from the Euler-Bernoulli equation, $EI\frac{\partial^4 u}{\partial t} = f(x)$, and is given by $u(x) = \left(\frac{3}{2}\frac{\delta}{L_s^2}\right)x^2 - \left(\frac{1}{2}\frac{\delta}{L_s^3}\right)x^3$ under free vibration conditions. Inserting the expressions for S_1 and $u(x)$ into equation (3-4) and solving the integral yields an expression for the transduction factor $[C/m]$ in terms of the device geometry and e_{31f} piezoelectric coefficient:

$$\phi = \frac{3e_{31f}b_e L_e t_{epi}}{2L_s^2}\left[1 - \frac{L_e}{2L_s}\right] \tag{3-5}$$

Noting that $q = C_{eb}V_{oc}$, where C_{eb} is the capacitance of the device when it is physically clamped or *blocked* to prevent motion and V_{oc} is the open-circuit voltage across the capacitance, equation (3-5) can be combined with the definition of the transduction factor from equation (3-4) to define an electrical sensitivity (i.e. voltage output per beam tip displacement) as:

$$S_e = \frac{3h(L_s L_e - \frac{1}{2}L_e^2)b_e}{2L_s^3}\frac{e_{31f}}{C_{eb}} \tag{3-6}$$

The acoustic sensitivity of the device can be defined as the open-circuit output voltage per unit of acoustic pressure, which can be expressed as the product of electrical and mechanical sensitivities as $S_{acst} = S_e S_m$, where S_e has units V/m and S_m has units m/Pa.

C. Mechanical Sensitivity & The Complete Analytical Model

The mechanical response of a rotational system may be expressed as:

$$\theta(\omega) = \frac{M_o/I}{\omega_o^2 + j2\omega_o\omega\zeta - \omega^2} \tag{3-7}$$

where M_o is the applied moment, I is the moment of inertia, and ζ is the damping ratio. Because the device is small compared to a wavelength of sound, the pressure along length of the device due to an incoming plane wave, $p(x,t) = P_o e^{j(\omega t - kx)}$, may be approximated using a two-term Taylor series as:

$$p(x,t) \approx p(0,t) + x\frac{\partial p}{\partial x}\Big]_{x=0} = P_o(1 - jkx)e^{j\omega t} \tag{3-8}$$

where $k = \omega/c_o$ is the acoustic wave number. The moment due to the acoustic pressure acting on the device may be expressed as:

$$M(x,t) = \int FxdA = \int_{-L/2}^{L/2} bxp(x,t)dx \approx -jkP_o I_A e^{j\omega t} = M_o e^{j\omega t} \tag{3-9}$$

where $M_o = -jkP_o I_A$ is the moment resulting from the acoustic pressure and $I_A = \frac{bL^3}{12}$ is the area moment of inertia. L and b in this case refer to the total length and width of the device, respectively. Noting that $I = \frac{mL^2}{12}$ for a cantilever beam and substituting the

expressions for M_o, I_A and I to equation (3-7), the rotational sensitivity $[rad/Pa]$ of the device may be expressed as:

$$S_{rot} = \frac{-jk}{\rho t_{epi} \omega_o^2} \left(\frac{1}{1 - r^2 + 2j\zeta r} \right), r \equiv \frac{\omega}{\omega_o} \tag{3-10}$$

where ρ is the density of silicon and t_{epi} is the beam thickness. Using a small angle approximation to express the mechanical sensitivity as $S_m = \frac{L}{2} S_{rot}$, the open-circuit voltage sensitivity of the device to acoustic excitation can then be expressed as

$$S_{acst} = S_m S_e = \frac{L}{2} S_{rot} S_e = \frac{-3jkLw_e}{4\rho\omega_o^2 L_s^3} \left(\frac{L_s L_e - \frac{1}{2} l_e^2}{1 - r^2 + 2j\zeta r} \right) \frac{e_{31f}}{C_{eb}} \tag{3-11}$$

Equation (3-11) represents an analytical model for the device sensitivity based solely on device geometry and material properties, which are known to a relatively high degree of accuracy, and the e_{31f} piezoelectric coefficient. The value of the e_{31f} coefficient varies for PZT films depending on film quality, poling, and other factors but, as will be discussed in Chapter 5, the value of the e_{31f} coefficient can be directly measured for a given film. Equation (3-11) assumes the first mode resonance frequency is known, either by measurements performed on an existing device, finite-element analysis (FEA), or analytical calculations. The rotational stiffness of the device is a combination of the torsional stiffness of the pivots and the bending stiffness of the cantilever end-springs, so analytical calculations of the first-mode resonance frequency must include both effects unless the contribution of one is determined to be insignificant for the particular device geometry being studied.

D. SUMMARY

This chapter presented the derivation of an analytical model for the first mode acoustic sensitivity, presented in equation (3-11) in terms of a known resonance frequency. The derivation made the assumption that the spring deflection profile matches that of a cantilever beam. This model is useful for quickly estimating sensitivity and is particularly useful in the design phase. However, this model does not include the effect of the second mode on the device response. The interaction of the first and second modes is crucial for the performance of the device, so a model that includes the effects of both modes should be used to verify the intended performance of the finalized design.

Chapter IV: Multi-Mode, Multi-Port Model

A. MOTIVATION

While the model developed in the last chapter is useful for providing insight into design parameters, it does not include the impact of higher order modes on the device response. It is particularly important to understand the impact of the second mode on the device dynamics. This mode responds to uniform pressure signals across the beam structure, giving it an omnidirectional response which can act to alter the directivity pattern in any regions where the second mode contributes significantly to the total device output. When the contribution of the second mode is negligible, a dipole response is achieved. However, as will be discussed in Chapter 7, the contribution of the second mode may be beneficial in certain applications. In any case, the ability to predict and control the contribution of the second mode is essential.

This chapter presents an efficient procedure for constructing a complete system model for multiple-vibration-mode, multiple-port transducers with arbitrarily complex geometries [52][1]. The model is based on a modal coordinate transformation and subsequent construction of a network model for each vibration mode of the device, up to the highest mode of interest. Modal velocity, rather than a particular physical velocity on the structure, is the mechanical flow variable through each modal network. Each mode network contains multiple transformers which represent the multiple transduction ports of the physical system. In many cases, use of a network model and a finite element model are considered mutually exclusive. Either lumped approximations with limited accuracy are used in an electrical network analysis, or the more rigorous finite element model is

[1] Content in this chapter appears in similar form in reference [52]:
M. L. Kuntzman, D. Kim, N. N. Hewa-Kasakarage, K. D. Kirk, and N. A. Hall, "Network modeling of multiple-port, multiple-vibration-mode transducers and resonators," *Sens. Actuators A, Phys.,* vol. 201, pp. 93-100, 2013.

used with all simulations completely contained within the finite element program. The former typically offers more design insight and computationally efficiency, while the advantage of the later is rigor and the ability to handle complex shaped structures. The proposed approach combines advantages of both. Only a discrete set of salient parameters are obtained from a single finite element eigensolution simulation (i.e., modal analysis). Namely, these are modal masses, modal resonance frequencies, and transducer port transformer ratios: defined, for piezoelectric transducers, as the short-circuit charge generated at the transducer port per unity input modal displacement. For capacitive transducers the transformer ratios are defined as the change in charge produced at the transducer port per unity modal displacement under constant bias voltage.

The model presented here has a broad application to many types of MEMS devices which benefit from the capability to accurately and efficiently model multi-mode, multi-port devices. Higher-order vibration modes are deliberately used in RF-MEMS to achieve high frequency and/or high Q oscillations [53-56]. The model presented here presents a systematic way to quantify and control the participation and generation of modes in a vibration by controlling the amplitude and phase of excitation voltages at multiple transducer ports. Another example of multiple-port MEMS transducers is RF-MEMS accelerometers described by Olsson et al. that detect shifts in modal resonant frequencies of a structure due to in plane accelerations [57]. These structures use multiple aluminum nitride (AlN) piezoelectric ports to generate and detect vibration of a tuning fork structure. Yet another example of multiple-port MEMS are multiple-electrode capacitive micromachined ultrasonic transducers (CMUTs) presented by Degertekin et al., which utilize exterior electrodes of a CMUT for biasing and interior electrodes for dynamic actuation and ultrasonic detection [58-61].

B. DESCRIPTION OF MODEL

The modeling procedure is based on two steps: (i) modal analysis and modal coordinate decomposition, and (ii) creating a network for each mode with modal velocity the mechanical flow variable in the network. Multiple transformers are used in each modal network, with each transformer corresponding to a transduction port of the physical system.

(i) Modal Coordinate Transformation

The time dependent displacement $\vec{u}(x,y,z,t)$ of a mechanical structure from equilibrium may be expressed as a superposition of vibratory modes as

$$u(x,y,z,t) = \sum_{i=1}^{M} \vec{\psi}_i(x,y,z)\eta_i(t) \tag{4-1}$$

where $\vec{\psi}_i$ is the *i*-th mode shape of a system. $\vec{\psi}_i$'s are the shape of free vibration eigensolutions to the elastodynamic equations of motion governing the structure with all transducer ports short-circuited (i.e., no coupling to the electrical domain). η_i 's are scalar functions of time, and M is the chosen number of modes to retain in the superposition analysis. This approach breaks down the structure's vibration into a finite degree of freedom system through a transformation to modal coordinates, η_i. A powerful result of normal mode analysis from vibration theory is mode orthogonally. In modal coordinates, elastodynamic equations of motion are decoupled to yield simple second order equations of vibration,

$$\ddot{\eta}_i + 2\zeta_i\omega_n\dot{\eta}_i + \omega_{n,i}^2\eta_i = F_i \tag{4-2}$$

where F_i is a scalar called a modal force and may be evaluated as

$$F_i = \iiint \overrightarrow{\psi_i}(x,y,z) \cdot \overrightarrow{f_b}(x,y,z,t)dV \tag{4-3}$$

where $\overrightarrow{f_b}(x,y,z,t)$ is the total body force per unit volume acting on the structure. For a system with a discrete rigid proof mass responding to acceleration inputs (e.g., many MEMS accelerometers [41, 62-65]), F_i is equal to the dot product of the input acceleration with the modal displacement vector evaluated at the center of mass, $F_i = \vec{\psi}_i(x_c,y_c,z_c)\cdot\vec{a}(t)$.

For a system responding to pressure loading $P(x,y,z,t)$ across the surface of the structure (e.g., MEMS microphones),

$$F_i(t) = \iint \overrightarrow{\psi_i}(x,y,z)\cdot\vec{n}P(x,y,z,t)dA \tag{4-4}$$

where $\vec{n}$ is a unit vector normal to the surface of the structure. The modal force, F_i, is a scalar that depends on external loading and is straightforward to compute, either analytically or computationally. Challenges that might otherwise arise from computing integrals in equations (4-3) and (4-4) are easily avoided using most any modern finite element software that can output these parameters. The directional microphone mode shapes presented in Figure 4.1 are obtained using finite element modeling software. ANSYS, the software used in this study, presents mass-normalized modes which, by definition, mean that mode shapes $\vec{\psi}_i$ have been scaled such that the modal masses, i.e., the coefficients proceeding $\ddot{\eta}_i$ in equation (4-2), are unity. In general, modal mass m_i is provided by

$$m_i = \iiint \rho(x,y,z)\overrightarrow{\psi_i}(x,y,z)\cdot\overrightarrow{\psi_i}(x,y,z)dV \tag{4-5}$$

The above analysis procedure summarized by equations (4-1) through (4-5) is an efficient and powerful technique commonly applied in the analysis of purely mechanical vibratory systems [66-68].

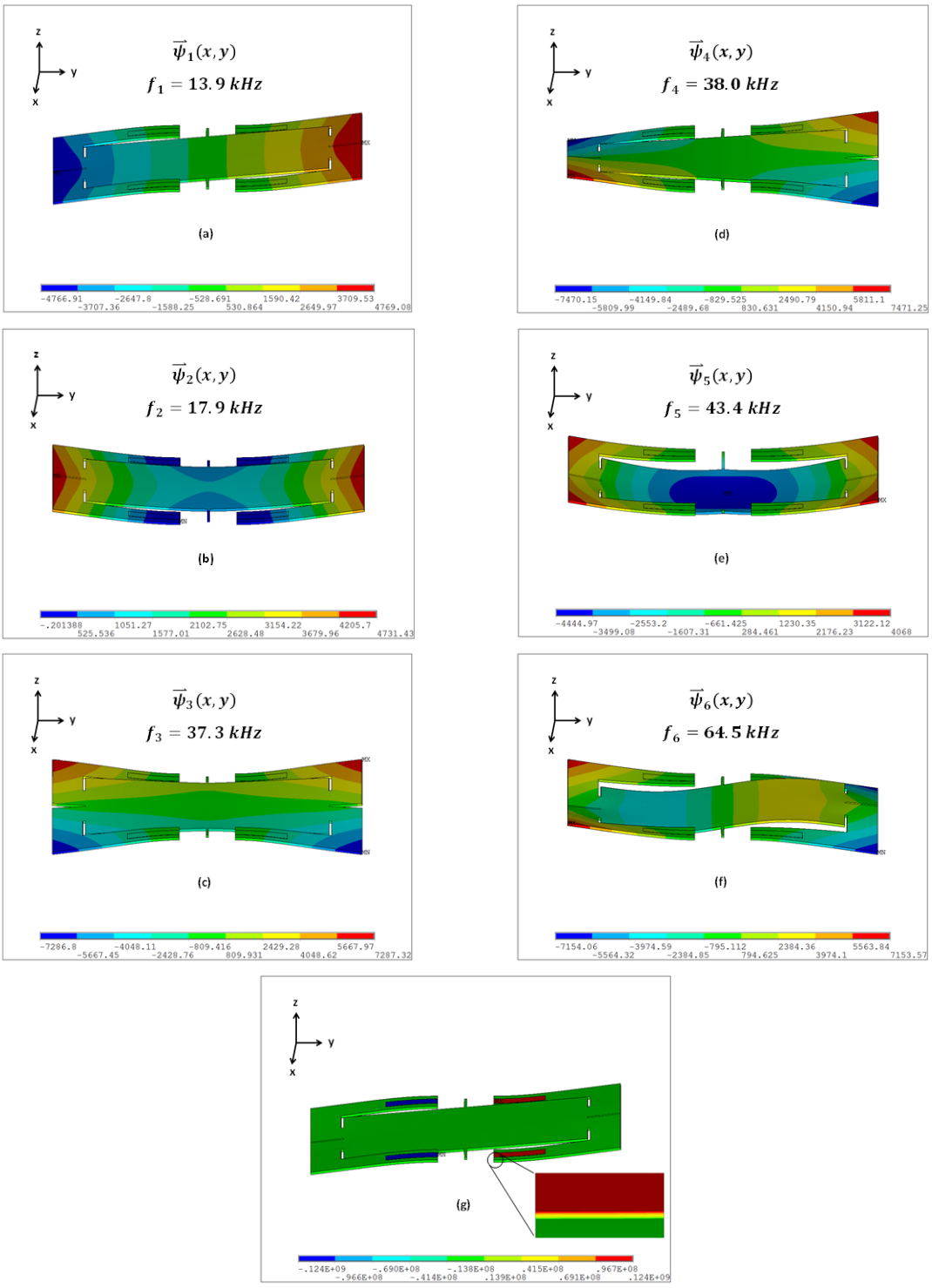

Figure 4.1: (a)-(f) FEA mode shapes for the first six modes and (g) the resulting electric field within the piezoelectric material for the first mode.

(ii) Energy Coupling Using Network Analogs

To incorporate multiple-port electromechanical coupling, an approach is presented which combines the modal coordinate system with network analogs which are pervasive in the study of energy coupling transducers [40, 69-73]. Equation (4-2) may be represented using a simple second-order RLC network model as shown in center section of Figure 4.2, with $\dot{\eta}_i$ (i.e., the modal velocity) as the mechanical flow variable through the network and F_i, the modal force, as the effort variable in the network. Coupling of energy to the piezoelectric ports is represented with the transformers shown in Figure 4.2, each transformer and electrical port in the network corresponding to a physical piezoelectric port labeled in Figure 1.3(a). ϕ_{ij} is used to denote the transformer ratio characterizing electromechanical coupling at the *j*-th port due to structural deformation of the *i*-th vibration mode. Voltage and current at each port follow the same notation. Specifically, V_{ij} and i_{ij} denote voltage and current, respectively, generated at the *j*-th port due to motion of the *i*-th mode. Selection of F_i and $\dot{\eta}_i$ as mechanical variables predefines ϕ_{ij} as the short-circuit charge generated at port *j* per a mechanical modal displacement η_i of unity. Each port, *j*, is also characterized by an electrical capacitance under blocked mechanical conditions, $C_{eb,j}$, as shown in the network of Figure 4.2.

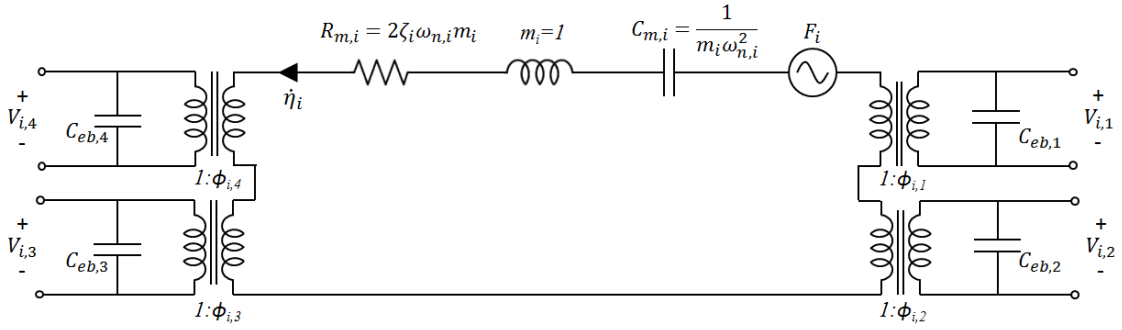

Figure 4.2: Multi-mode, multi-port network model

Figure 4.2 presents a model for a system with four transducer ports (e.g., the piezoelectric in-plane pressure gradient microphone). For any particular mode shape of the physical system, depicted in Figure 4.1, each piezoelectric port has unique coupling depending on the location of the piezoelectric thin film element on the structure and, in particular, the mechanical strain field at the location of the film. Consider the first vibration mode, i.e. $i=1$ in Figure 4.2. With all electrical ports in Figure 4.2 short-circuited, a physical modal displacement $\eta_1 = 1$ results in a short-circuited charge $q_{1,j}$ across each port. This short-circuit charge at each port is, by definition, numerically equal to $\phi_{1,j}$ and is readily obtained from a finite element modal analysis of the physical structure. ANSYS, for example, enables integration of piezoelectric analysis with modal analysis. Figure 4.1(g) shows the electric potential generated at port 1 resulting from $\eta_1 = 1$ under an open terminal condition.

Each modal analysis result presented in Figure 4.1 provides complete information needed to construct the network for that mode. The critical circuit parameters are: modal mass m_i (set to unity), mode compliance $C_{m,i}$ (equal to $1/\omega_{n,i}^2$), and all of the port transformer values $\phi_{i,j}$ which are numerically equal to the short-circuit charge at each port resulting from the modal displacement of unity, as provided by ANSYS. Piezoelectric material properties were initially assumed to be equal to those of PZT-5H [74] and were later replaced with values measured from the fabricated device using methods that will be described in Chapter 5. Mechanical damping is not provided as part of the modal analysis, but if desired can be modeled from first principles in the design stage for each modal displacement profile. Alternatively, a modal damping ratio ζ_i can be chosen for each mode in an ad-hoc manner and/or later fitted to experimental data. In either case, mechanical resistance, $R_{m,i}$, of each mode is equal to $2\zeta_i\omega_{n,i}$. To illustrate utilization of the model, several analysis examples are considered:

a. Sensing

To analyze the response of the sensor to acoustic plane waves arriving in the x-direction, consider that acoustic pressure loading is provided by $P(x,t) = P_0 e^{j(\omega t - kx)}$ with P_o and k the amplitude and wavenumber of the incident sound. All modal forces, F_i, can be computed following equation (4-3), most easily performed within the FEA software package. Because the device is small compared to a wavelength of sound, an incident plane wave along the sensitive axis of the device can be approximated about the pivot location, $x = 0$, by a two-term Taylor series as:

$$p(x,t) \approx p(0,t) + x\frac{\partial p}{\partial x}\bigg|_{x=0} = P_o(1 - jkx)e^{j\omega t} \tag{4-6}$$

Substituting this expression into equation (4-4) yields:

$$F_i(t) = P_o \iint \vec{\psi}_i(x,y)dA - jkP_o \iint \vec{\psi}_i(x,y)xdA = F_{i,unif} - jkF_{i,grad} \tag{4-7}$$

showing the excitation force for each mode can be broken down into two terms, with $F_{i,unif}$ representing the first, uniform loading, term of the Taylor series in equation (4-6) and $F_{i,grad}$ representing the second, gradient loading, term. The mode shapes have already been determined by the FEA modal analysis, so all the information necessary to solve the integrals has been attained. An alternative to solving the integrals is to use a mode-superposition harmonic analysis, in which an applied load is harmonically swept through a specified frequency range and the resulting modal displacements are calculated, to find the modal force components, $F_{i,unif}$ and $F_{i,grad}$. At frequencies far below the natural frequency of the mode, the model displacement for a given load converges to a constant value, given by:

$$F_{i,load}(t) = \omega_{n,i}^2 \eta_{dc,load} \tag{4-8}$$

where *load* is used to represent both the *unif* and *grad* loading cases. The values $F_{i,unif}$ and $F_{i,grad}$ therefore be calculated by applying a constant load, $Po = 1$, and a unity-slope gradient load, $P(x) = x$, respectively, and multiplying the value of $\eta_{dc,load}$ which is converged to at low frequencies by the square of the natural frequency of the mode. The modal FEA results for the first six modes are shown in Figure 4.1. The modal forces calculated by method are given in Table 4-1 along with the natural frequencies and electromechanical coupling factors and extracted from the modal analysis.

In traditional capacitive microphones, a high-pass filter is formed by the RC network of the acoustic vent piercing and back cavity compliance. As mentioned in Chapter 1, the high pass filter is introduced intentionally to prevent sensitivity drift with changes in ambient pressure. For the piezoelectric pressure gradient microphone, a high-pass filter is formed by the acoustic resistance of the slots in the silicon device layer and the back cavity, which are labeled in the CAD rendering in Figure 4.3. However, unlike traditional capacitive MEMS microphones, the cut-off frequency of the high-pass filter for the prototype devices is significantly higher than the audio band. With respect to the second mode, the net acoustic pressure applied to the beam is the difference between the applied uniform acoustic pressure on the top surface of the beam, P_o, and the uniform pressure internal to the back cavity depicted in Figure 4.3, P_{cav}. The simple acoustical network model in Figure 4.4 may be used to solve for the net pressure as

$$P_o - P_{cav} = j\frac{f/f_c}{1 + j\,f/f_c}P_o \tag{4-9}$$

R_{a_slit} represents the acoustical resistance of the slots labeled in Figure 4.3 while C_{a_cav} is the acoustical compliance of the back cavity volume beneath the MEMS die. In conventional microphones the cutoff frequency, f_c, is designed to be below the audio band. For the biomimetic microphone, f_c is greater than 20 kHz, so that the denominator

in equation (4-9) approximately equals unity throughout audio bandwidth. For the simulations presented in the next chapter, the second mode force, F_2, was multiplied by $j\frac{f/f_c}{1+jf/f_c}$ to account for this effect. This effect does not impact the first mode response due to pressure equalization in the back cavity.

Table 4-1.
Simulated Modal Parameters for Acoustic Measurements

	Mode #:	Transformer Ratios, ϕ_{ip}				Simulated Natural Frequency, $f_{n,i}$ (kHz)	Modal Force: DC loading, $F_{i,unif}$	Modal Force: Gradient Loading, $F_{i,grad}$
		Port #1	Port #2	Port #3	Port #4			
Device #1	1	-0.104	-0.104	0.104	0.104	14.0	-0.295e-15*	0.153e-16
	2	0.107	0.107	0.107	0.107	18.4	-0.549e-12	-0.288e-20*
Device #2	1	-0.0841	-0.0841	0.0841	0.0841	8.70	-0.432e-15*	0.516e-16
	2	0.0857	0.0857	0.0857	0.0857	11.5	-0.174e-11	-0.409e-20*

* Non-zero due to numerical round-off in the software.

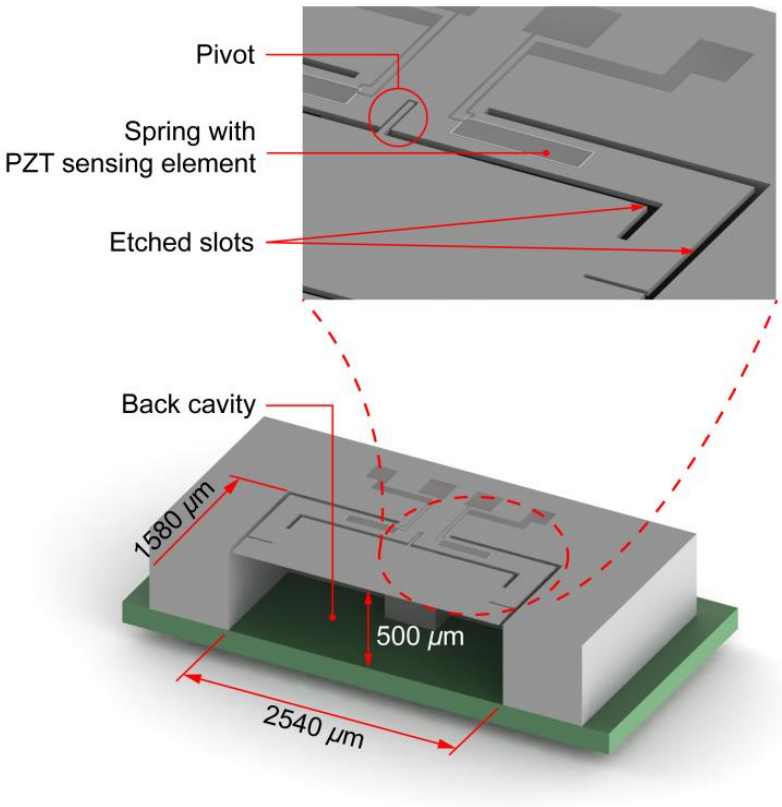

Figure 4.3: CAD rendering of slots and back cavity that form an acoustic high pass filter.

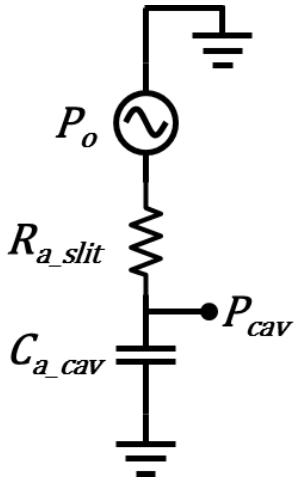

Figure 4.4: Network model representing the acoustic high pass filter formed by the slot resistance and back cavity compliance.

The network for each mode can then be analyzed independently for any parameter of interest, and the results then superimposed. For example, if the short-circuit charge is sensed at all of the ports shown in Figure 1.3(a), as would be the case when using charge amplifiers with ideally zero input impedance, then each mode displacement η_i is given by

$$\eta_i = \frac{F_i C_{m,i}}{1 - r_i^2 + 2j\zeta_i r_i}, \quad r_i \equiv \frac{\omega}{\omega_{n,i}} \tag{4-10}$$

The total charge signal at a particular port j would then be given as the superposition of the charge signal generated by each mode, or

$$q_{sc,j} = \phi_{1,j}\eta_1 + \phi_{2,j}\eta_2 + \cdots \phi_{M,j}\eta_M = \sum_{i=1}^{M} \phi_{ij}\eta_i \tag{4-11}$$

If instead open-circuit voltages are sensed, Figure 4.2 makes clear that each mode is electromechanically stiffened by $C_{eb,j}/\phi_{ij}^2$ terms, which physically arise due to storage of electrical potential energy in the form of charge separation at each piezoelectric port. Kim, et al, recently used similar effects to tune RF oscillators, in which case external capacitors were connected to ports in an AlN MEMS resonator [34]. The proposed model presents a convenient method for quantifying such effects across multiple vibration modes.

b. Actuation

The multi-mode network in Figure 4.2 can also be used to efficiently model the response of the structure to actuation voltages applied at the ports. Most generally, voltage inputs of different amplitude and phase can be applied at each port, and the complex amplitude of the voltage input at each port will affect the extent to which a particular vibration mode is generated or suppressed. Assuming zero external loading, the modal force, F_i, in Figure 4.2 is zero for each mode. Further, there can be only physical

voltage, V_j, applied at each port. Referring to Figure 4.2, the modal force generated by application of a voltage V_1 at port 1 is $\phi_{i1}V_1$, which results from transferring the applied signal to the right side of the transformer. The total modal force generated on the first mode, which determines the participation of mode 1 in the overall response, is then

$$F_1 = \phi_{11}V_1 + \phi_{12}V_2 + \cdots \phi_{1,N}V_N = \sum_{j=1}^{N} \phi_{ij}V_j \tag{4-12}$$

where N is the number of ports of the system. More generally, the complete set of modal forces is computed as

$$\begin{bmatrix} F_1 \\ \vdots \\ F_M \end{bmatrix} = \begin{bmatrix} \phi_{11} & \cdots & \phi_{1N} \\ \vdots & \ddots & \vdots \\ \phi_{M1} & \cdots & \phi_{MN} \end{bmatrix} \begin{bmatrix} V_1 \\ \vdots \\ V_N \end{bmatrix}, \quad \text{or} \quad F_i = \phi_{ij}V_j \tag{4-13}$$

Equation (4-13) represents an $M \times N$ set of equations, and ϕ_{ij} is a system matrix that completely characterizes the mapping of complex actuation voltages to the modal forces acting to drive each mode. In an analysis scenario, modal forces F_i resulting from a particular set of actuation voltages V_j can be computed using equation (4-13). As a design scenario, one may desire to discover the port actuation voltages that produce a desired set of modal forces, F_i, and to do so one would multiply equation (4-13) by the inverse of ϕ_{ij}, denoted $\Phi_{ji} = \phi_{ij}^{-1}$. i.e.,

$$V_j = \Phi_{ji}F_i \tag{4-14}$$

Equation (4-14) can be solved so long as Φ_{ji} is computable. A necessary but insufficient condition is that N be at least equal to or greater than M (i.e., at least as many actuation ports are required as the number of modes one wishes to control the actuation of). Because equation (4-14) enables the selection of modal forces, we refer to $\Phi_{ji} = \phi_{ij}^{-1}$ as

the mode selectivity matrix of a multi-port transducer system. Mode suppression is important, for example, in the design and operation of high frequency micromechanical resonators [5, 35]. Equation (4-14) may also find application in the design of closed loop force-feedback sensor systems, where one wishes to apply feedback to certain vibration modes but not to others (e.g., manipulating only a pair of system poles while leaving others unaffected).

c. Port-to-Port Transfer Functions

For applications such as chemical sensing [36, 37], it may be advantageous to use a multiple port transducer to actuate with one port and sense with another, while monitoring changes in the port-to-port transfer function that result from detection of a particular agent. Port-to-port transfer functions are readily simulated using the networks summarized in Figure 4.2. For example, the transfer function between charge measured at port 2 and an applied actuation voltage at port 1 is determined by solving for q_2/V_1 for each modal network individually and superimposing results. For all ports shorted except port 1, q_2 due to actuation voltage V_1 is provided by

$$\frac{q_{sc,2}}{V_1} = \sum_{i=1}^{M} \frac{\phi_{i,1}\phi_{i,2}C_{m,i}}{1 - \left(\frac{\omega}{\omega_{n,i}}\right)^2 + 2j\zeta_i\left(\frac{\omega}{\omega_{n,i}}\right)} \tag{4-15}$$

C. Model Verification using Port-to-Port Measurements

Model verification is performed by comparing simulated port-to-port transfer functions with measured transfer functions. Port-to-port measurements provide a very clean measurement across multiple modes of resonance, which can be more difficult to accomplish in acoustic measurements. As such, the port-to-port measurements are useful

for verifying the multiple-port, multiple-mode model prior to its application to the intended acoustic operation of the device.

A broadband white-noise input voltage was applied at port 4 while the open-circuit voltage was measured at port 2, with the port numbering following the labels in Figure 1.3(a) A high input impedance non-inverting amplifier (op amp model TI TLE2072, 10-MΩ input impedance, and 100-Ω and 1-kΩ gain resistors to provide 11× closed-loop voltage gain) was used to measure the voltage at port 2, and the 11× gain is later discounted for presentation of results. The fast Fourier transform (FFT) of the port 2 signal is normalized to the FFT of the input spectrum at port 4 to obtain the measured amplitude transfer function presented in Figure 4.3. The procedure was automated and performed using the bin centers feature of the Prism dScope Series III audio analyzer. The port-4-to-port-3 (4-3) transfer function was also measured and is presented in Figure 4.5. Both transfer functions were simulated using the network in Figure 4.2 with circuit parameters summarized in Table 4-2. Figures 4.6 and 4.7 present a comparison of measured and simulated 4-2 and 4-3 transfer functions, respectively. Two simulations are presented for each case, one using the modal resonance frequencies directly from the finite element model and one using resonant frequencies that have been fitted to correspond to peak frequencies in the measured data. Both sets of modal resonance frequencies are summarized in Table 4-2 The presented model accurately predicts the measured response with high quantitative accuracy over a broad frequency range spanning more than four vibration modes of the device. The phase of the 4-2 transfer function was also measured, using a National Instruments PXI-4461 dynamic signal analyzer and a LabVIEW frequency sweep virtual instrument (VI), and presented alongside simulation results in Figure 4.8. Again, network simulation shows highly accurate results across a frequency range covering five vibration modes of the device.

The complex interactions of translation and rotational modes in Figure 4.1 that give rise to the differences in the measured 4-2 and 4-3 transfer functions are captured by the model.

Table 4-2.
Network Parameters for Port-to-Port Measurements

Mode #:	Transformer Ratios, ϕ				ANSYS Natural Frequencies (kHz)	Fitted Natural Frequencies (kHz)
	Port #1	Port #2	Port #3	Port #4		
1	-3.98e-2	-3.98e-2	3.98e-2	3.98e-2	13.9	12.0
2	3.99e-2	3.99e-2	3.99e-2	3.99e-2	17.9	18.0
3	-6.61e-2	6.61e-2	6.61e-2	-6.61e-2	37.3	35.5
4	-6.71e-2	6.71e-2	-6.74e-2	6.73e-2	38.0	36.3
5	2.46e-2	2.46e-2	2.46e-2	2.46e-2	43.4	47.1
6	-4.73e-2	-4.73e-2	4.73e-2	4.73e-2	64.5	64.5

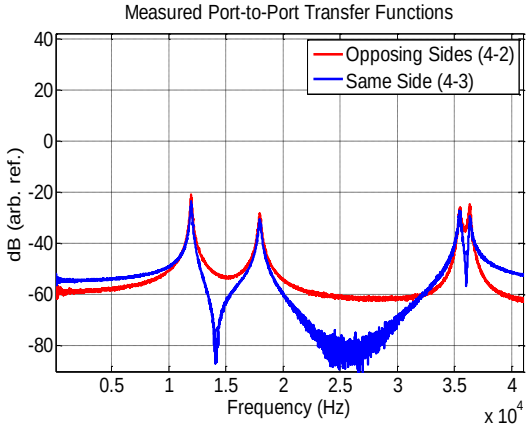

Figure 4.5: Measured port-to-port transfer functions.

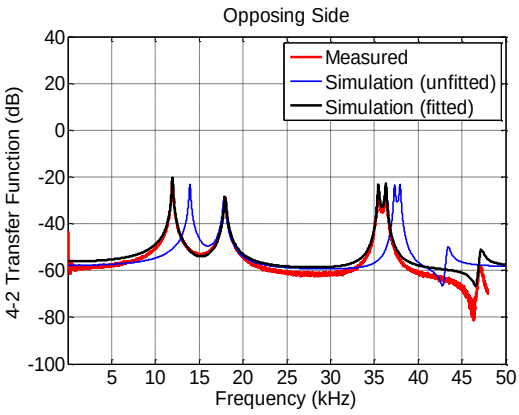

Figure 4.6: Measured and simulated port-4-to-port-2 transfer function.

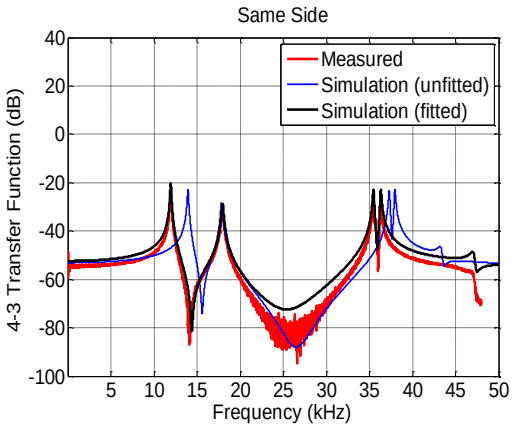

Figure 4.7: Measured and simulated port-4-to-port-2 transfer function.

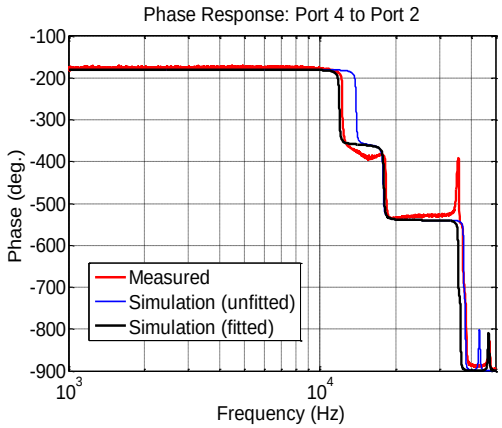

Figure 4.8: Measured and simulated port-4-to-port-2 phase response.

As noted from Figure 1.3(a), the 4-2 transfer function is one in which actuation and detection are on opposing sides of the pivot while actuation and detection are on the same side of the pivot for the 4-3 transfer function. In light of this and the mode shapes presented in Figure 4.1, some interesting differences of the measured transfer functions in Figure 4.5 are intuitive. For the *opposing-side* case, first and second mode contributions are out of phase at frequencies to left of $f_{n,1}$ while they are in phase for the for *same-side* case. This explains why the 4-2 transfer function is lower in amplitude than the 4-3 transfer function at DC. To the right of $f_{n,1}$, the phase of the first mode shifts 180 degrees and first and second modes are in phase for the 4-2 transfer function and out of phase for 4-3 transfer function. This explains the anti-resonance in the 4-3 case and the absence of an anti-resonance in the 4-2 case. Similar reasoning explains the difference in the transfer functions near and in-between modes three and four (i.e., between 35 kHz – 37 kHz) in Figure 4.5.

In this particular case-study, damping was not modeled but rather fitted. The Q of each resonance peak was extracted from the measured transfer function data and used in the networks of Figure 4.2 to generate the simulation. Finally, although not discussed in detail in this work, modeling of direct port-to-port capacitive coupling predicts a level of

−60 dB which is, coincidentally, near the same level as motional coupling in between resonances. The direct port-to-port coupling is due to the insulating oxide and conductive epitaxial silicon plane which resides beneath the piezoelectric ports to form additional parasitic capacitors. This direct coupling has no frequency dependence over the measurement range presented. It has also been included in the simulation results in Figures 4.6 through 4.8. It should be emphasized for clarity that the port-to-port transfer function measurements are not pertinent to the fundamental operation of the piezoelectric microphone device presented. Rather, this measurement was performed as a means to illustrate verification of the device model and also to cleanly extract the Q value and frequency of each mode.

Chapter V: Characterization and Model Verification

A. Packaging and Poling

The devices were mounted into 44-lead chip carriers and wire bonded using a West Bond 7476E wedge-wedge bonder[2]. To pole the PZT, leads were soldered onto the chip carrier and the devices were mounted on a hot plate. An electric field of approximately 10 MV/m was generated in the PZT by the application of 10 V from an external power supply. The devices were poled for 1 hour at 160° C with the potential applied and were allowed to cool to room temperature before the potential was removed. Remaining solder on the chip carriers was removed using solder wick so that the carriers could be inserted into sockets during the device characterization phase.

B. Measurement of Electrical and Piezoelectric Properties

The capacitance for each port is measured using an admittance spectroscopy method [75]. The measurement configuration is shown in Figure 5.1. An AC voltage is applied to the device and the admitted current is measured using a transimpedance amplifier (TIA), allowing the capacitance to be calculated using the expression:

$$C_{eb} = \frac{V_{meas}}{\omega R_f V_{app}} \tag{5-1}$$

where, V_{meas} is the output voltage of the TIA, V_{app} and ω are the magnitude and frequency of the voltage applied to the device, respectively, and R_f is the TIA feedback resistor. This method can determine the capacitance of the sensor with very high accuracy. Because the thickness and lateral dimensions of the PZT electrode stack can also be measured with a high degree of accuracy, it is possible to accurately calculate the

[2] Content in this chapter to appear in similar form in:
M. L. Kuntzman, N. N. Hewa-Kasakarage, A. Roche, D. Kim, and N. A. Hall, "Micromachined in-plane pressure gradient piezoelectric microphones," submitted to the *IEEE Sensors Journal* for publication.

relative permittivity of piezoelectric material. The capacitance and relative permittivity for each device under test are given in Table 5-1. The relative permittivity is calculated from the measured capacitance assuming $\varepsilon_r = C_{eb} t_{pzt} / \varepsilon_o A_{pzt}$.

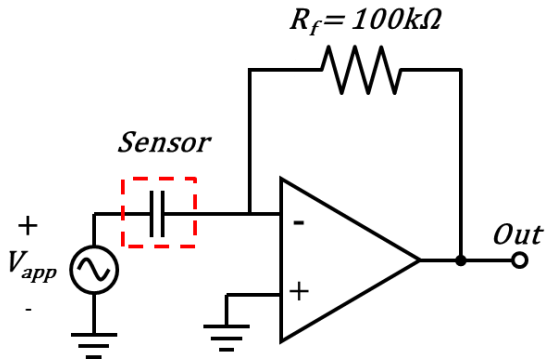

Figure 5.1: Admittance setup for measuring the device capacitance.

Table 5-1.
Measured Electrical and Piezoelectric Properties

Description	Symbol	Device #1	Device #2
Beam Thickness	t_{epi}	20 μm	10 μm
Rotational Beam Dimensions	$b_d \; x \; L_d$	1 x 2 mm	1 x 2 mm
Spring Dimensions	$b_s \; x \; L_s$	250μm x 1mm	250μm x 1mm
Electrode Dimensions	$b_e x \; L_e$	105 x 464 μm	105 x 464 μm
PZT Thickness	t_{pzt}	1.05 μm	1.56 μm
PZT Solution Type	-	Commercial	Homemade
Measured Capacitance	C_{eb}	270 pF	170 pF
Relative Permittivity*	ε_r	657	615
Measured e_{31f} Piezoelectric Coefficient	e_{31f}	4.26 C/m^2	1.62 C/m^2

For piezoelectric devices operating in the 3-1 bending mode, the e_{31f} piezoelectric coefficient determines the voltage produced per induced strain. The sensitivity of the device is proportional to the e_{31f} coefficient, which can vary widely for PZT films [76]. It is, therefore, important to accurately measure this parameter for the fabricated films. Combining equations (3-4) and (3-5) the e_{31f} coefficient of a cantilever beam can be calculated using the expression:

$$e_{31f} = \frac{2L_s^3}{3hw_e\left(L_s l_e - \frac{1}{2}l_e^2\right)}\frac{q}{\delta}\Bigg]_{V=0} \approx \frac{2L_s^3}{3hw_e\left(L_s l_e - \frac{1}{2}l_e^2\right)}\frac{C_{eb}V_{oc}}{\delta} \qquad (5\text{-}2)$$

where q is the short-circuit charge, δ is the spring-tip displacement, C_{eb} is the blocked device capacitance, V_{oc} is the open-circuit voltage output of the device, and all other terms are defined in Table 5-1. The first term of this equation contains only geometric terms which are known to a high degree of accuracy. The expression on the right is not exactly equal to the expression on the left due to capacitive loading introduced when the piezoelectric port is in the open-circuit condition, however, the loading effect was observed to be negligible for this particular device. A measurement of the e_{31f} coefficient can, therefore, be performed by simultaneously measuring the spring deflection and admitted short-circuit current or open-circuit voltage while the device is being electrostatically actuated. A labeled micrograph taken while the device was mounted on the experimental apparatus is shown in Figure 5.2 to illustrate the measurement procedure. A broadband noise signal is applied to one port while the resulting spring-tip deflection is measured using a laser Doppler vibrometer (LDV) and the open-circuit voltage is measured using a high-impedance amplifier at a different port. Noting that $\delta = \int v dt = \frac{v}{j\omega} = \frac{S_{LDV}V_{LDV}}{j\omega}$, where V_{LDV} is the voltage output of the LDV and $S_{LDV}\left[\frac{mm}{s\cdot V}\right]$ is the sensitivity setting of the LDV and discounting the gain of the amplifier,

the resulting displacement and open-circuit voltage is plotted in Figure 5.3. Choosing values at the first mode resonance frequency, where the deflection profile closes matches that of a cantilever beam for which equation (5-2) is valid, the measured displacement is 0.305 nm and the resulting open-circuit voltage is 5.3 μV, giving a measured e_{31f} coefficient value of approximately 4.26 C/m^2 for the 20-μm-thick device. Similar measurements on the 10-μm-thick device yielded an e_{31f} coefficient value of approximately 1.62 C/m^2, as noted in Table 5-1. It should be noted that these values are somewhat lower than is typical for PZT [76], which makes the sensitivity lower than might otherwise be expected. Determining why the e_{31f} coefficient is lower than expected remains future work, but it could be due to non-ideal poling conditions, poor PZT stoichiometry, impurities in the PZT solution, or a variety of other factors. It should be noted that *Device-1* used a commercial PZT solution while *Device-2* used a solution synthesized at UT Austin.

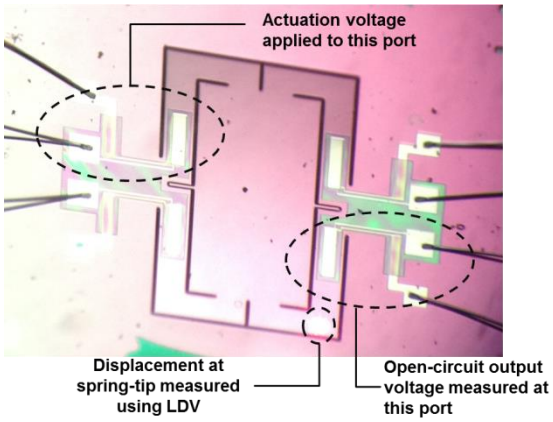

Figure 5.2: Labeled micrograph illustrating e_{31f} experimental apparatus.

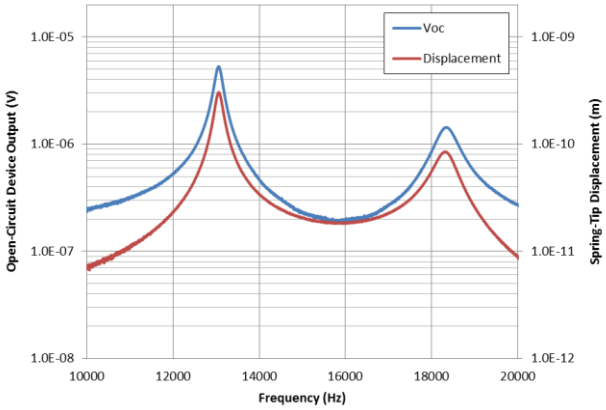

Figure 5.3: Plots of simultaneously measured output voltage and spring-tip displacement used to calculate the e_{31f} value of the PZT films.

C. Acoustic Characterization

(i) Acoustic Packaging

The device was mounted on a three-inch circular PCB with integrated surface-mount readout electronics. A photograph of the PCB designed for the sensor presented in Chapter 6 is shown in Figure 5.4. A similar PCB was designed for the piezoelectric microphone. The PCB was designed to fit within a mesh ball, as shown in Figure 5.5 which provides electromagnetic shielding without interfering with acoustic signals.

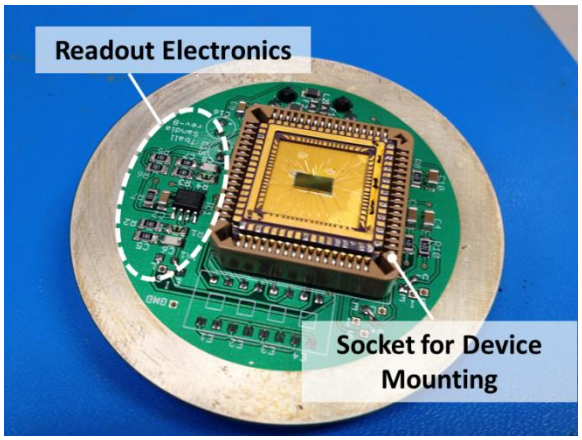

Figure 5.4: Labeled photograph of the PCB designed for acoustic testing.

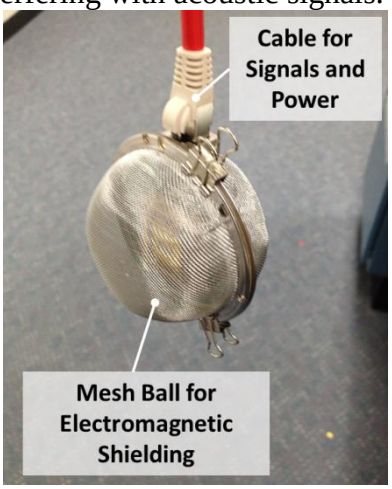

Figure 5.5: The acoustic testing PCB inside the wire mesh shielding ball.

(ii) Sensitivity & Acoustic Frequency Response

The acoustic frequency response of the devices was measured in an approximately 10’x10’x10’ walk-in anechoic facility at the University of Texas at Austin, using the swept sine function of a Prism dScope III audio analyzer, with an Adam A5 studio monitor as an acoustic source and a GRAS 40AC reference microphone for calibration. The acoustic frequency responses measured at a single port of *Device-1* and *Device-2* are shown in Figure 5.6 and 5.7, respectively and compared to both the analytical first-mode model and the full multi-mode model. The measured natural frequency and quality-factor for each mode of each device is given in Table 5-2.

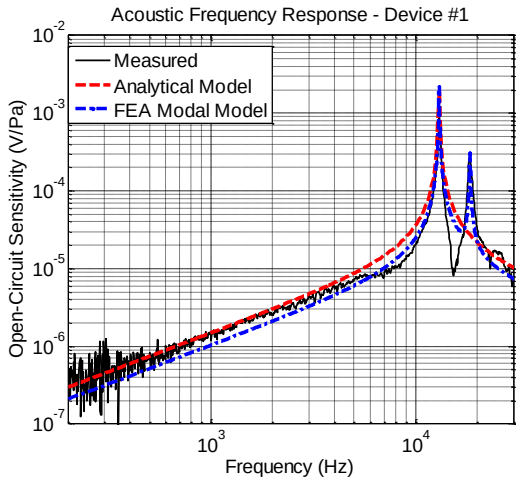

Figure 5.6: Measured and simulated acoustic frequency response of Device-1.

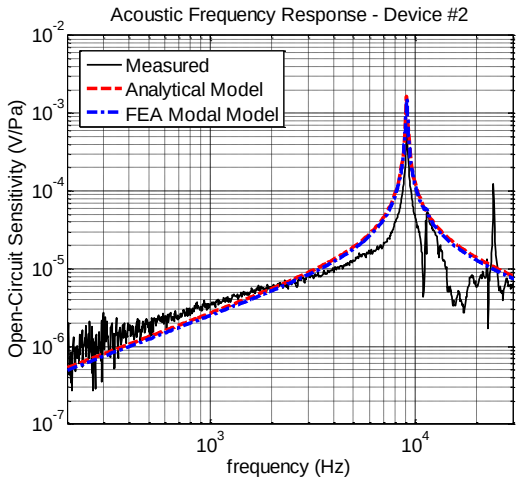

Figure 5.7: Measured and simulated acoustic frequency response of Device-2.

Table 5-2.
Summary of Measured Modal Parameters

	Mode #:	Measured Natural Frequency (kHz)	Measured Quality Factor, Q_i	Damping Factor, ζ_i *
Device #1	1	13.0	71.9	7.00e-3
	2	18.3	35.6	1.41e-2
Device #2	1	9.1	67.7	7.40e-3
	2	11.4	33.8	1.48e-2

*From measured *Q*-factor.

(iii) Directivity

The measured directivity of a single port at 1 kHz is plotted in Figure 5.8. At any given frequency, the output at a given port is proportional to the overall motion of the corresponding spring at that frequency, which is a superposition of the first and second mode contributions. In regions strongly dominated by the first mode, a dipole directivity is expected, while an omnidirectional response is expected in regions strongly dominated

by the second mode. At all other regions, the directivity response is expected to be some combination of dipole and omnidirectional responses, weighted by the ratio of the first and second mode contributions. Noting that a dipole response can be represented with a cosine function [6], the expression for the directivity as a superposition of modes may be expressed as:

$$D(\omega,\theta) = \cos\theta + \frac{V_{2,p}(\omega)}{V_{1,p}(\omega)} = \cos\theta + \alpha(\omega) \tag{5-3}$$

where, $V_{2,p}(\omega)$ and $V_{1,p}(\omega)$ are the contributions of the second and first modes, respectively, to the total output measured at a given port, p. The function $\alpha(\omega) = V_{2,p}/V_{1,p}$ is the ratio of the modal contributions at a given frequency. The measured directivity at 1 kHz plotted in Figure 5.8 is not a perfect dipole because of this effect. The ratio of the first and second mode may be backed out of the measurement by fitting the value of $\alpha(\omega)$ so that equation matches the measured directivity. This fitted, simulated directivity is also plotted in Figure 5.8, showing very good agreement for a value of $\alpha = 1/4.5$, indicating that the first mode contribution is approximately $4.5x$ greater than the second mode contribution at this frequency. The larger lobe of the directivity function, centered at $\theta = 0°$, occurs when the port being measured is facing the source and the first and second modes are in-phase, while the smaller lobe occurs when the measurement port is facing away from the source and the modes are out-of-phase.

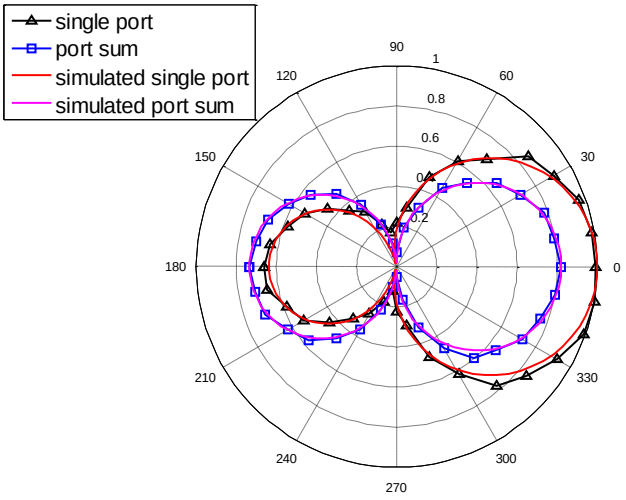

Figure 5.8: Measured and simulated directivity of *Device-1* at 1 kHz.

The directivity function can be altered by summation of ports. Figure 5.8 also shows the case where the directivity is measured while taking the differential output between ports 3 and 4, which are located on opposing sides of the axis of rotation, as labeled on Figure 2a. In this case, the second mode (i.e. common-mode) contribution is cancelled, resulting in a directivity function that much more closely resembles a dipole. Fitting of equation (5-3) to this measurement gives mode ratio of $\alpha = 1/18$, an improvement of approximately 12 dB in second mode rejection compared to the single port measurement. The frequency response of the summed port case is shown in Figure 5.9. Rather than a doubling of signal, as might be intuitively expected, the signal level should be expected to increase from the magnitude of the 0° directivity lobe to the sum of the 0° and 180° lobes, which corresponds to an increase in sensitivity of approximately 65% or 4.3 dB. This closely matches the sensitivity increase of 4.6 dB observed in the measurement at 1 kHz. It should be noted that there is some slight variation in sensitivity between ports. Figure 5.9 shows second-mode rejection of approximately 24 dB, indicating the pair of ports used in this measurement are more closely matched than those used in the directivity plot in Figure 5.8.

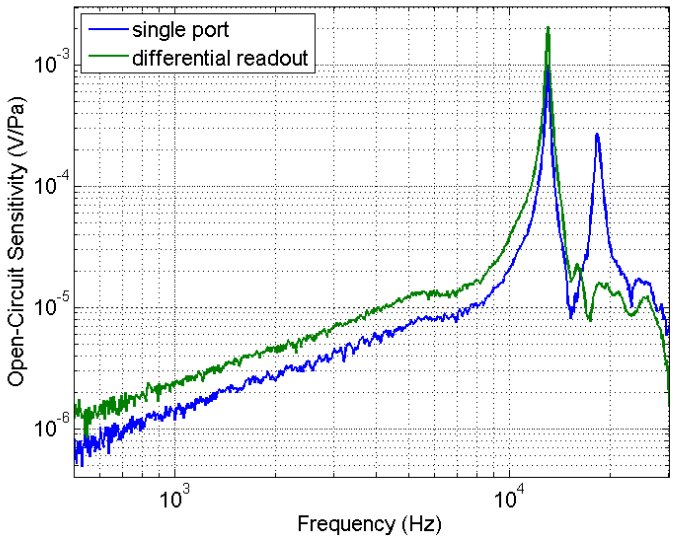

Figure 5.9: Acoustic frequency response of Device-1 with two ports summed for cancellation of the 2nd mode.

(iv) Noise Characterization and Minimum Detectible Signal

The self-noise of a sensor determines the minimum signal level which can be detected. The dominant noise source in capacitive and optical MEMS microphones is often the thermal-mechanical noise due to one or more of the sources of acoustical damping in the system, which include the back plate perforations, the sound inlet hole, and the acoustical vent piercing [12, 34, 77]. In piezoelectric microphones, the dominant noise source is often the Johnson noise associated with the dielectric loss of the piezoelectric material. This dielectric loss is typically quantified by a dissipation factor, $tan\delta$, which is the tangent of the angle between the real and imaginary components of the film impedance [76].

The noise model for the microphone and charge amp readout circuitry is shown in Figure 5.10, which is similar to models presented elsewhere [46, 78, 79]. The electronic noise sources include the current and voltage noise of the operational amplifier, $i_{n,amp}$ and $v_{n,amp}$, respectively, and the Johnson-Nyquist noise of the feedback resistor, $v_{n,Rf}$. The

measured and simulated noise for a single port is shown in Figure 5.11. The noise response is dominated by the feedback resistor noise at low frequencies, the sensor *tanδ* noise between about 400 Hz – 2 kHz, and the op amp voltage noise at high frequencies. When multiple sensing ports are used, the signal-to-noise ratio is expected to increase by approximately the square root of the number of ports, due to the dielectric loss noise at each port being incoherent while the signals are coherent. While the design presented has significantly higher noise than current state-of-the-art technology, it should be noted that the designs presented are not optimized and were intended primarily to provide proof-of-concept of the fabrication process and operating principle. It remains future work to apply the theoretical framework developed in this work to the design of an improved sensor.

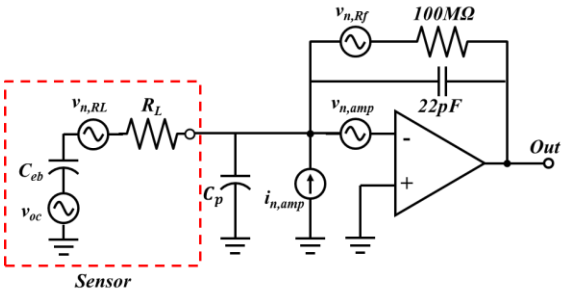

Figure 5.10: Noise model for the charge amplifier circuitry.

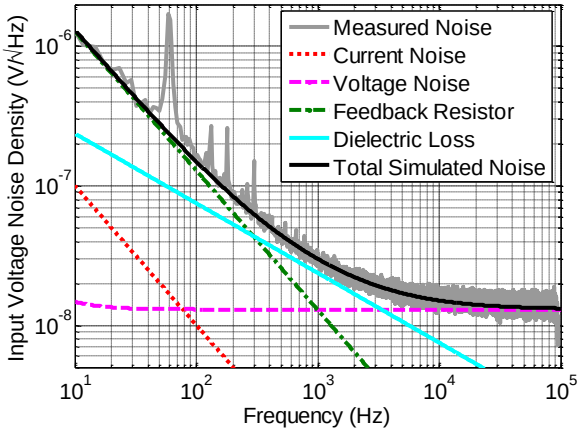

Figure 5.11: Measured and simulated noise at the input of the amplifier.

Chapter VI: A Vacuum-Sealed In-Plane Acoustic Pressure Gradient Sensor

A. BACKGROUND

This chapter introduces another unconventional acoustic sensor[3]. The sensor is motivated by the observation of several limitations to traditional MEMS microphone technology.

(i) The through-wafer etch to form the backside cavity is a bottle-neck in the fabrication process, which increases unit cost.

(ii) Integration of on-chip CMOS electronics allows reduction in overall device footprint by moving from a two-chip solution with separate MEMS and ASIC dies to a single-chip solution where the MEMS and readout electronics exist on the same chip. This reduction in footprint may prove beneficial for future technology as the size of mobile technology decreases and chip density increases. However, integration of on-chip CMOS electronics is made more difficult by the requirement of a through-wafer etch.

(iii) Dissipative mechanisms in mechanical and acoustical systems generate Brownian motion owing to the generalized fluctuation dissipation theorem [80, 81]. The dominant dissipative mechanism in conventional capacitance microphones throughout audio frequencies is viscous air damping introduced by the back plate and acoustical vent resistance. [9, 82].

[3] Content in this chapter to appear in similar form in:
M. L. Kuntzman, D. Kim, and N. A. Hall, "Microfabrication and experimental evaluation of a rotational capacitive micromachined ultrasonic transducer (RCMUT)," submitted to the *J. Microelectromech. Syst.* for publication.

Capacitive micromachined ultrasound transducers (CMUTS) are typically vacuum-sealed, which allows them to avoid all of the problems enumerated above. By removing the air from within the cavity, there is no longer a need for a backside cavity, perforated back plate, or acoustical vent, which eliminates both the bottle neck caused by the through wafer etch and the thermal-mechanical noise introduced by the acoustical damping of the perforated back plate and vent resistance. Also, because CMUTs do not require a through-wafer etch, they can be fabricated using purely surface-machining based process, which allows CMUTS to be fabricated directly on top of CMOS electronics [83, 84].

It is clear that there are potential advantages to adapting CMUT inspired vacuum-sealing technology to an audio frequency sensor. However, because acoustic pressure signals are small in comparison to ambient atmospheric pressure, vacuum-sealed sensors require stiff membranes to avoid collapse under ambient pressure. While stiff membranes are desirable for immersion applications in the MHz frequency range, they reduce sensitivity and result in high input-referred acoustic noise for lower-frequency microphone applications. One design seeking to overcome this challenge and utilize vacuum-sealing in an audio frequency sensor was presented by Hansen, et. al [85]. The sensor consisted of an array of parallel-plate capacitive CMUT devices wired to form an RF transmission line. Incoming acoustic signals cause a change in capacitance of each CMUT element and therefore modulate the propagation speed of transmitted and detected RF signals. Sensing is performed by measuring the phase modulation of the RF carrier signal. The CMUTS forming the transmission line are sealed under vacuum with the goal of reducing the thermal-mechanical noise. Each of the forty-five CMUT units had dimensions of 70 x 190 μm and a first mode resonance of approximately 1 MHz. The total size of the microphone die was approximately 1.3 mm^2. Because CMUTS are

vacuum-sealed, thermal-mechanical noise is minimized and it becomes more critical to design ultra-low noise readout electronics to achieve the best possible SNR. The advantage of the phase modulation detection scheme is increased sensitivity to detection of small changes in capacitance and improved noise performance compared to more traditional readout methods. The improved noise performance is the result of the phase detection method being impervious to parasitic capacitance and the circuitry not requiring large resistor values that are dominant sources of noise in more traditional readout circuitry [46, 78]. It should be noted that the RF detection method developed by Hansen et al. could be applied to arrays of other types of capacitive sensors, including the sensor being introduced in this chapter.

The unconventional acoustic sensing structure presented in this chapter is motivated by the desire to achieve a microphone sealed under vacuum for low thermal-mechanical noise, but with a design path to a higher compliance to acoustic signals than can be achieved with conventional CMUTs. While the sensor is substantially different from the piezoelectric in-plane pressure gradient microphone, it does take advantage of a similar rocking structure and may be modeled using the methods developed in Chapters 3 and 4. In this sense, it can be thought of as a hybrid of the innovative work performed by Miles et. al. [23] with state-of-the-art CMUT technology. The sensor may be thought of as a future generation of the rocking in-plane pressure gradient microphone in that it may offer advantages in size, performance, CMOS compatibility, and simplicity of fabrication over any of the other biologically-inspired designs to date [23, 29, 33, 38].

In what follows, an overview of the sensor construction and operation is presented and followed by a detailed description of prototype device fabrication. Electrostatic and acoustic characterization confirms device models and anticipated device functionality of these first-generation prototypes.

B. Overview of the Sensor

A 3-D computer-aided design (CAD) image of the device structure is presented in Figure 6.1. Two conventional parallel-plate CMUT pistons are connected via a beam that rotates about a pivot. Each piston consists of a rigid bottom electrode fabricated on the substrate and a compliant top electrode for capacitance transduction. Each CMUT is sealed under vacuum as described in more detail subsequently. The coupling beam is designed to be stiff in bending, while offering ideally zero stiffness against rotation about its pivot, as is noted in the schematic in Figure 6.2. As such, the structure is designed to be resistant to collapse under large atmospheric pressure which is applied equally to both pistons, while at the same time being compliant to small acoustic signal gradients along the x-axis of the structure, as labeled in Figures 6.1 & 6.2. Because the sensor only rotates upon pressure imbalance (i.e., pressure gradient), the sensing structure has an inherently directional response to sound. Specifically, if the beam is perfectly rigid, the response is that of a dipole with maximum sensitivity in the x-direction, as labeled in Figures 6.1 & 6.2. Directivity is not the driving motivation behind the innovation but rather an ancillary feature of the device structure, which we term a rotational micromachined ultrasonic transducer (RCMUT) [30].

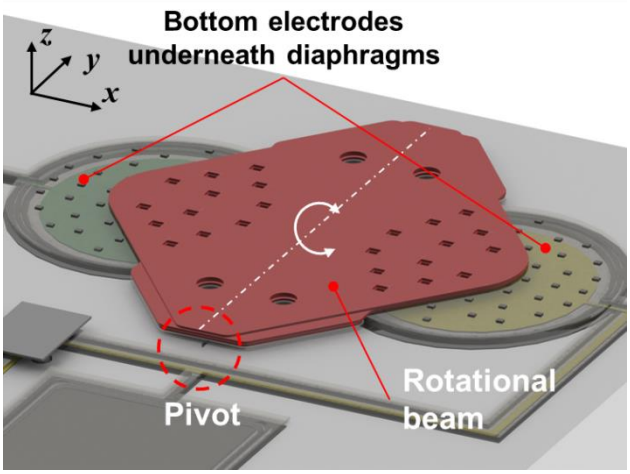

Figure 6.1: CAD rending of the external beam rotational capacitive ultrasound transducer (RCMUT).

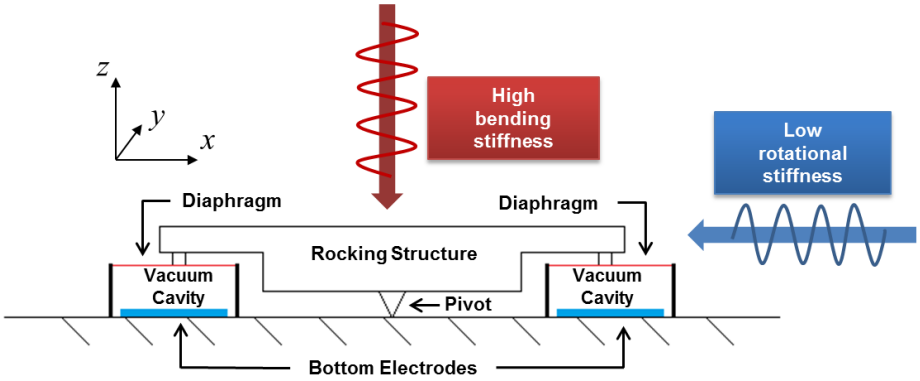

Figure 6.2: Operational schematic of the external beam rotational capacitive ultrasound transducer (RCMUT).

Figure 6.3(a) presents a scanning electron microscope (SEM) image of a fabricated device taken from a top-side view and Figure 6.3(b) presents a side-view SEM of the pivot and beam structure. The beam is diamond-shaped to provide maximum rigidity against flexing and minimal rotational inertia about the axis of rotation. Figure 6.4 presents a micrograph from the topside of a chip containing four RCMUTs aligned along the same axis. Also labeled in Figure 6.4 is a reference microphone, which is a non-vacuum-sealed omnidirectional surface-micromachined microphone with over 250 kHz bandwidth. This structure is modeled, characterized, and described in detail

separately in a pending journal publication [79] and is used in this work as an omnidirectional, on-chip calibration reference for characterizing the RCMUT prototype. The remaining unlabeled structures on the micrograph in Figure 6.4 are not relevant to this work. Figure 6.5 presents an SEM of the reference microphone from the topside. The 630-μm diameter diaphragm region is outlined on the SEM. The outer region of the device is an extended cavity, supported by rigid post structures, which acts to reduce squeeze film effects by providing a larger volume for air displaced by the diaphragm motion to flow into.

Figure 6.6(a) presents a labeled SEM image of an RCMUT from the topside, while Figure 6.6(b) presents an oblique view enabling observation of the circular diaphragm structure and the end of the rotational beam. Structures are labeled on the image which aid in the vacuum-sealing process, as will be explained in the next section. Although not visible in Figure 6.6(b), the tip of the diamond-shaped beam makes contact to the diaphragm at a point near the diaphragm center.

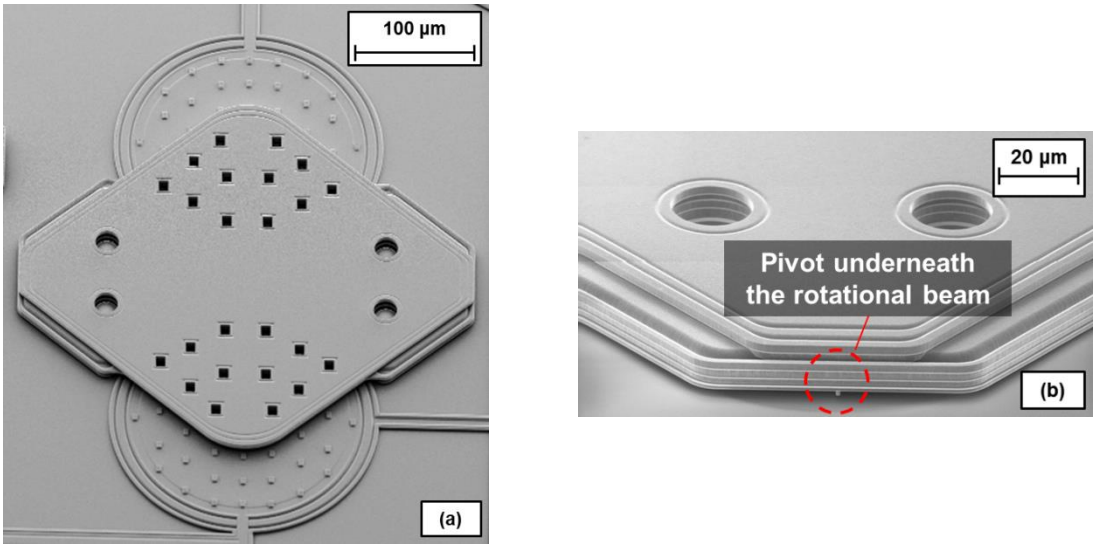

Figure 6.3: SEMs of the Type-1 external-beam RCMUT device (a) from the topside and (b) from a side-angle showing the pivot region.

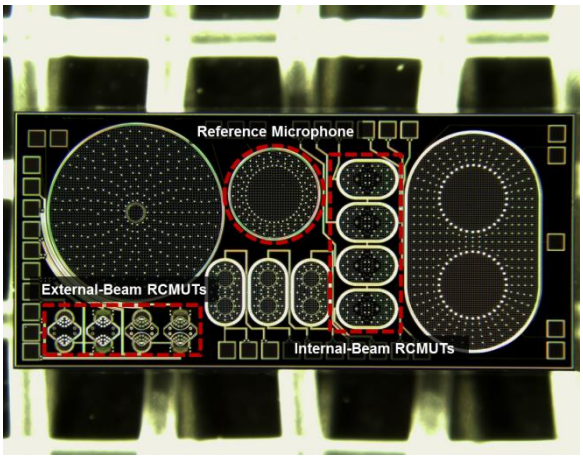

Figure 6.4: Micrograph of the RCMUTs and the reference microphone on the same silicon die.

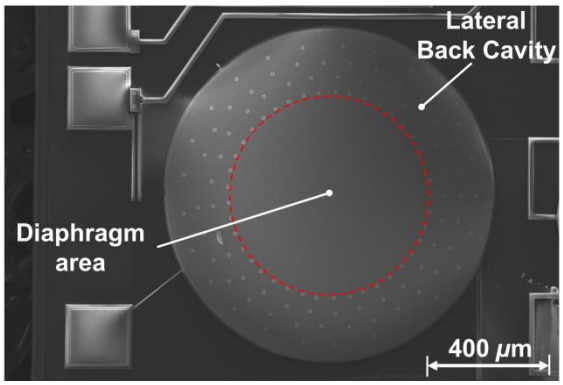

Figure 6.5: SEM image of the omnidirectional reference microphone used for the RCMUT measurement.

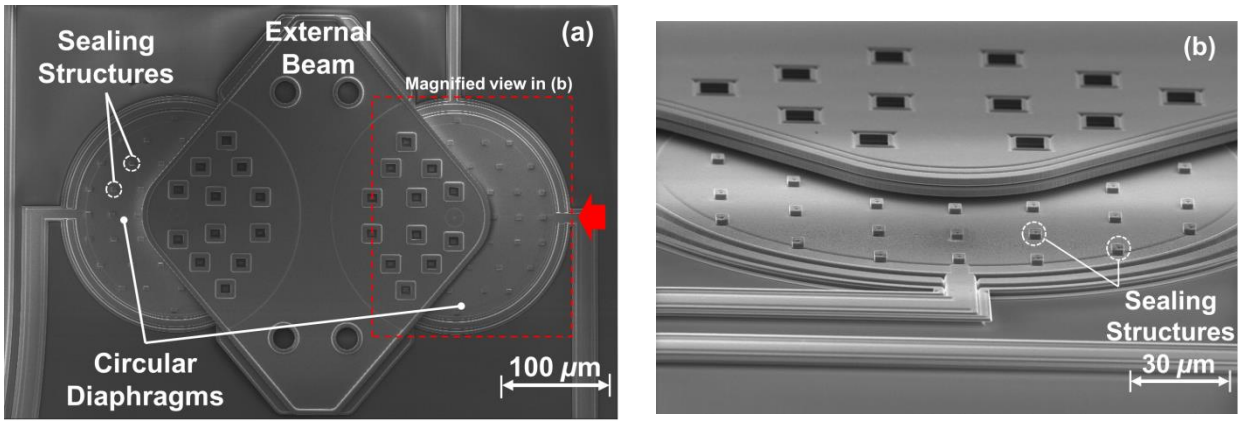

Figure 6.6: Labeled SEMs of (a) the topside view and (b) the diaphragm and beam-end region of an external-beam device.

An operational schematic of another, *internal-beam* variation of the RCMUT design is shown in Figure 6.7, with CAD renderings of the design shown in Figure 6.8. An array of these devices is also labeled on the micrograph in Figure 6.4. In this design, the rocking beam structure is contained within a single vacuum-sealed cavity, rather than externally coupling two independently sealed cavities. This design has the benefit of potentially further reducing thermal-mechanical noise by eliminating the air beneath the rocking beam structure. A labeled SEM taken from the topside of the device is shown in

Figure 6.9. The perimeter diaphragm regions are defined by a ring of support posts which constrain the top membrane from moving. The diameter of each diaphragm region is 200 μm and the overall device dimensions are 718 x 462 μm. The sensor is a three-port device with two independent bottom electrodes ports and one shared diaphragm/beam port. An SEM of the pivot region of a device which was diced to reveal the internal structure is shown in Figure 6.10(a). Figure 6.10(b) is an SEM of the diaphragm region, showing the end of the beam structure and one of the bottom capacitive sensing electrodes. An SEM showing an array of the devices is shown in Figure 6.11.

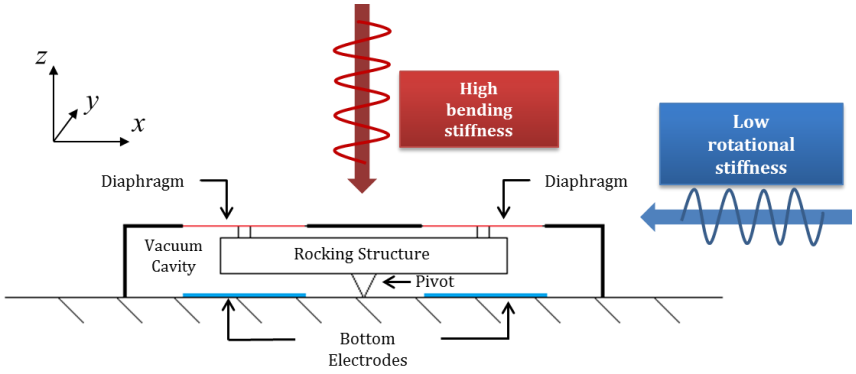

Figure 6.7: Operational schematic of the internal-beam RCMUT.

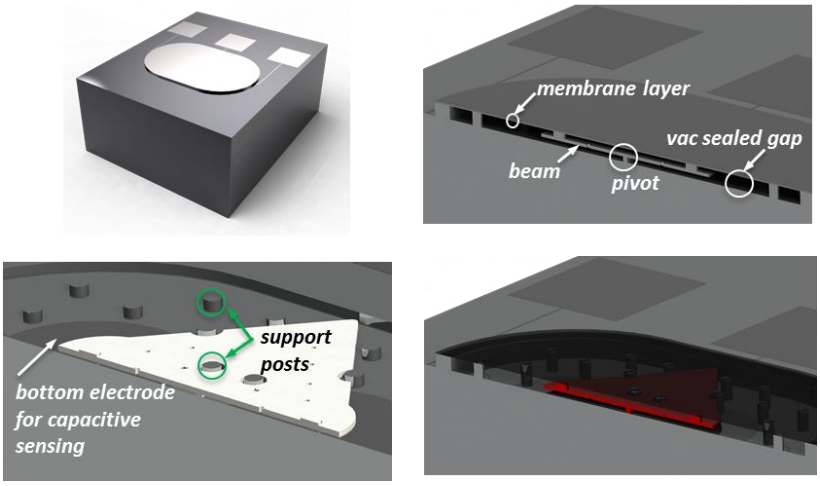

Figure 6.8: CAD rendering of the internal-beam RCMUT design.

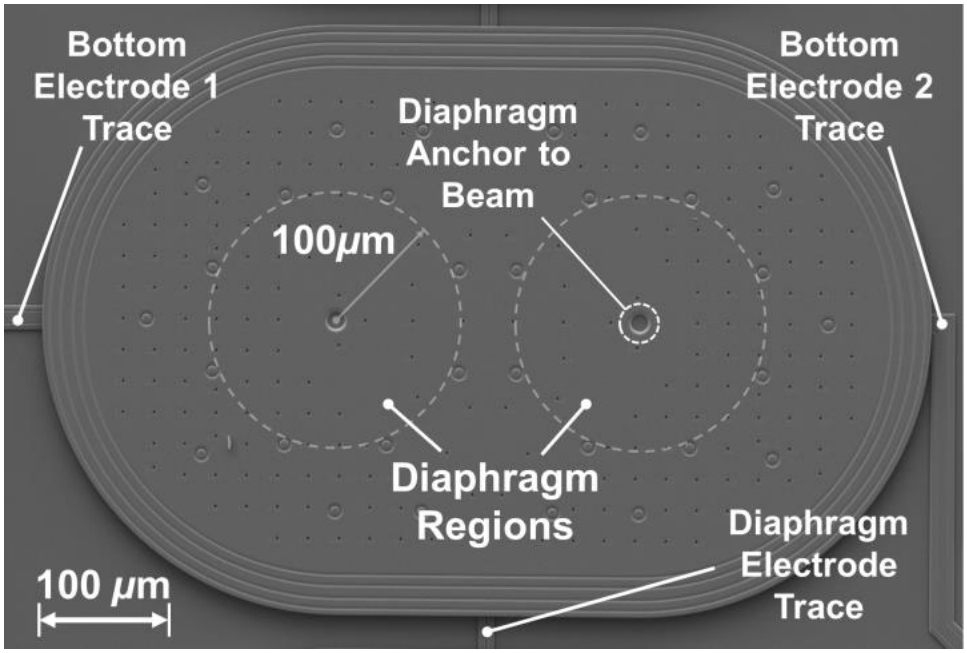

Figure 6.9: Labeled SEM of the internal-beam device taken from the top-side.

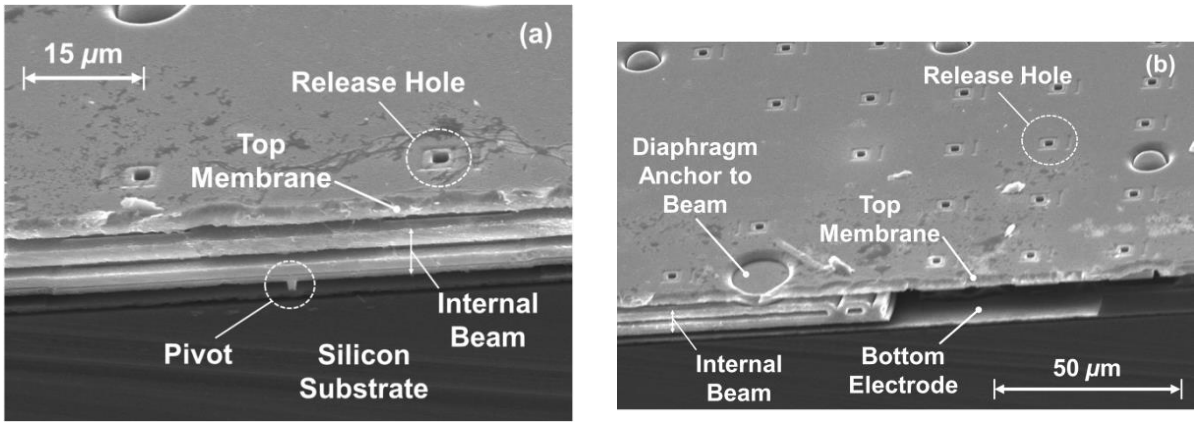

Figure 6.10: Cross-section SEMs an internal-beam device which was diced to reveal the internal structure (a) showing the pivot region and (b) showing the diaphragm region.

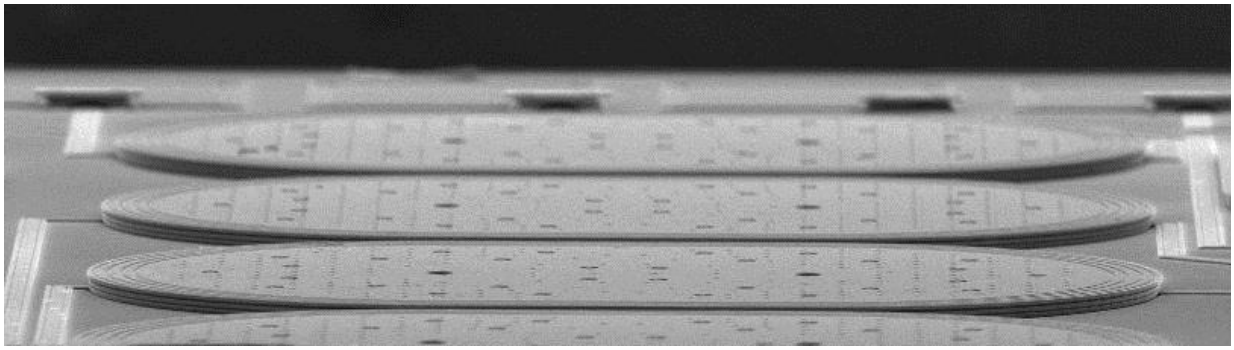

Figure 6.11: An SEM of an array of the internal-beam RCMUT devices.

C. Fabrication of Prototype Devices

(i) External Beam Devices

Both the internal and external-beam vacuum-sealed designs, as well as the omnidirectional reference microphone, were fabricated on a single silicon die using a foundry external to MRC. The foundry uses a standard process comprised of five planar layers of highly doped, conductive, polysilicon alternating with five sacrificial oxide layers. An image of the process layer stack is shown in Figure 6.12. Cross-section sketches of the external-beam device at key steps of the fabrication process are shown in Figure 6.13. The process begins with a low resistivity, n-type, silicon wafer with 0.63 μm of thermally grown silicon dioxide and 0.80 μm of silicon nitride deposited as an insulating dielectric foundation. A 0.3-μm-thick LPCVD polysilicon layer (poly-0) is deposited and patterned to form the bottom electrodes and electrical traces. A 2-μm sacrificial oxide layer (oxide-1) is deposited. The pivot is formed by a 1.5-μm deep timed etch into the oxide, referred to as a *dimple* etch, and followed by a full etch through the oxide to define the diaphragm anchors. A 1-μm-thick polysilicon layer (poly-1) is deposited and patterned; forming the diaphragms and filling in the dimple etch to form the pivot and lower beam section. 2-μm × 2-μm oxide-release holes are patterned in the

poly-1 diaphragms. A 0.3-μm sacrificial oxide layer (oxide-2) is deposited and patterned. The 1.5-μm poly-2 layer is deposited and patterned, adding thickness to the lower section of the beam structure and forming posts for the beam to anchor to the diaphragms. The oxide-3 layer is deposited, combining with the oxide-2 layer to form what will be the gap between the beam and diaphragm. A chemical-mechanical polish (CMP) is performed after the oxide-3 deposition to remove the underlying topology. The remaining 2.25-μm poly-Si 3, 2.0-μm oxide-4, and 2.25-μm poly-4 layers are deposited and patterned, with each layer adding thickness to the upper beam structure. A CMP is performed after the oxide-4 deposition to remove underlying topology.

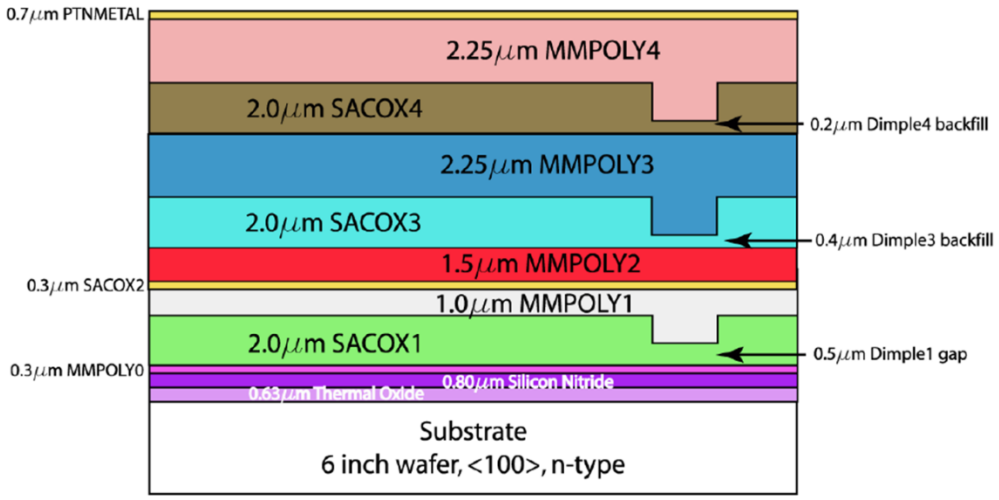

Figure 6.12: The surface-micromachining process layer stack.
(Used with permission - Courtesy of Sandia National Laboratories, SUMMiTTM Technologies, www.mems.sandia.gov)

1) Start with a silicon wafer with a dielectric foundation of SiO_2 and Si_3N_4.

2) Deposit and pattern poly-0 to form the bottom electrodes.

3) Deposit oxide-1 and perform a timed *dimple* etch to form the pivot.

4) Pattern oxide-1 to form diaphragm anchors.

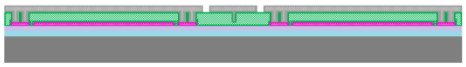

5) Deposit and pattern poly-1 to form the diaphragms.

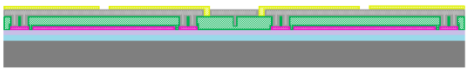

6) Deposit and pattern oxide-2.

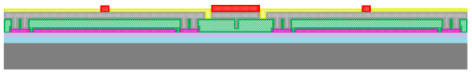

7) Deposit and pattern poly-2 to form the diaphragm contact posts.

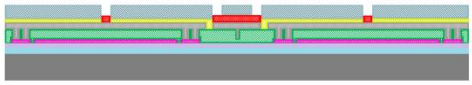

8) Deposit and pattern oxide-3 to add thickness to the beam structure.

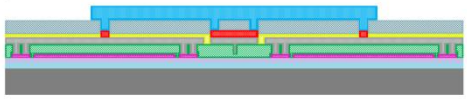

9) Deposit and pattern poly-3 to add thickness to the beam structure.

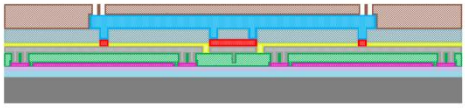

10) Deposit and pattern oxide-4 to add thickness to the beam structure.

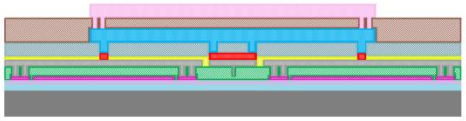

11) Deposit and pattern poly-4 to add thickness to the beam structure.

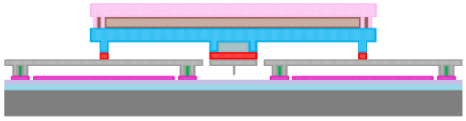

12) Remove the sacrificial oxide using an HF release process.

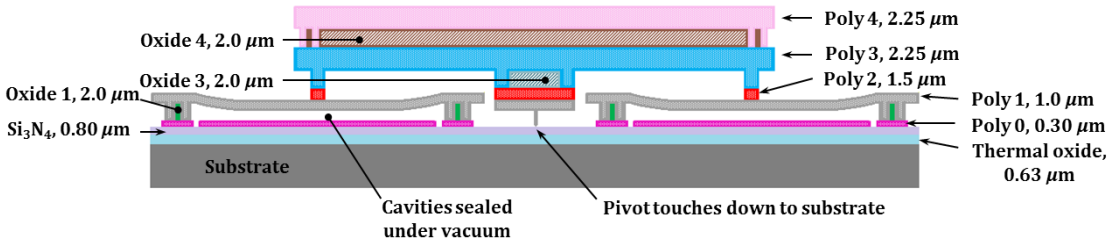

13) Deposit approximately 240 nm of Al_2O_3 by ALD to vacuum-seal the structure.

Figure 6.13: Fabrication process flow for the external-beam RCMUT design.

The process has a minimum etch-hole size of 2 μm. A small rectangle of the poly-2 layer material is patterned above each release hole and anchored to the poly-1 diaphragms. The gap between the poly-2 rectangles and poly-1 diaphragm is 0.3 μm, the thickness of the oxide-2 layer, which is removed after release. These structures are included so that vacuum-sealing can be achieved by depositing a film slightly thicker than 0.3 μm under vacuum, rather than attempting to fill the larger 2-μm release holes, as would otherwise be required. These structures are hence referred to as *sealing structures*. For simplicity, they are not shown in the sketches in Figure 6.13, but they are labeled in the SEM image in Figure 6.6. At the end of the process, a hydrofluoric acid (HF) release etch is performed, which removes any uncaptured oxide and frees the mechanical structure. After the release etch, a post-process atomic layer deposition (ALD) step is used to deposit an approximately 240-nm-thick Al_2O_3 film under vacuum to close the sealing structures, so that the cavities beneath the diaphragms remain sealed under vacuum. SEMS of the sealing-structures before and after the ALD deposition are shown in Figure 6.14(a) & (b), respectively. A gap beneath the structure exposing the release hole can clearly be seen in Figure 6.14(a), while the gap has been closed in Figure 6.14(b).

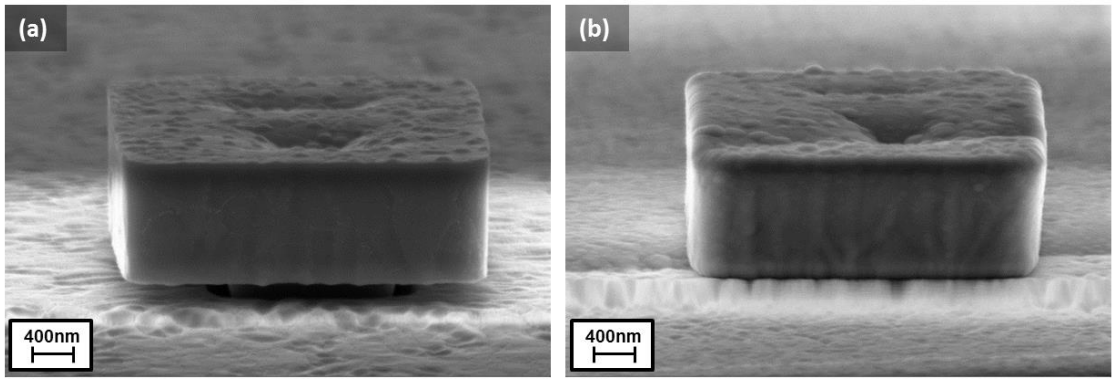

Figure 6.14: Sealing structures of the external-beam design (a) before and (b) after the atomic layer deposition (ALD) of an approximately 240 nm thick Al_2O_3 film.

Two variations of the both the external-beam were fabricated; one that captured and retained the sacrificial oxide within the beam structure, resulting in thicker 11.3-μm-thick beams composed of both silicon and silicon oxide and one that did not retain the sacrificial oxide, resulting in a thinner 7.0-μm-thick beams composed solely of silicon. The thicker beam devices are denoted *Type-1* and the thinner beam devices *Type-2*. The cross-section sketches in Figure 6.13 illustrate fabrication of the *Type-1* devices only.

(ii) Internal Beam Devices

The internal-beam devices are fabricated using the same fabrication process described above. Cross-section sketches of the internal-beam device at key steps of the fabrication flow are shown in Figure 6.15. The internal-beam devices use the poly-4 layer for the top membrane, while the beam is composed of all the layers between poly-1 and poly-3. The sealing structures for the internal-beam devices take the form of *drip-pan* structures beneath the diaphragm, which are fabricated out of the poly-3 layer. These structures are shown in the SEM images in Figure 6.16. In this case, the gap which must be closed during the vacuum-sealing process is the 200 nm thickness of the dimple-4 backfill, as labeled on the process layer stack in Figure 6.12. The ALD sealing process is sufficiently conformal for an approximately 250-nm-thick Al_2O_3 film deposition to close this gap at the bottom of the release hole. The internal-beam devices also have two variations: one which retains the sacrificial oxide within the beam, resulting in a 7.05-μm-thick beam, and one which does not retain the sacrificial oxide, resulting in a 4.75-μm-thick beam. As with the external-beam designs, the thicker beam variation will be denoted *Type-1* and the thinner beam variation is denoted *Type-2*.

1) Start with a silicon wafer with a dielectric foundation of SiO_2 and Si_3N_4.

2) Deposit and pattern Poly-0 to form the bottom electrodes.

3) Deposit and pattern Oxide-1. The pivot is formed using a timed *dimple* etch.

4) Deposit and pattern Poly-1.

5) Deposit and pattern Oxide-2.

6) Deposit and pattern Poly-2 to add thickness to the beam structure.

7) Deposit and pattern Oxide-3.

8) Deposit and pattern Poly-3 to add thickness to the beam structure.

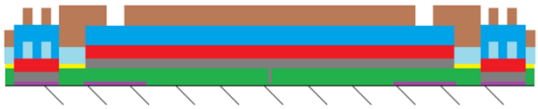

9) Deposit and pattern Oxide-4.

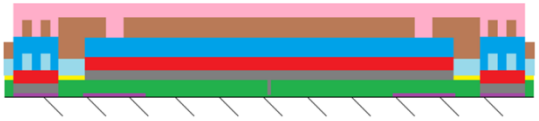

10) Deposit and pattern Poly-4 to form the top membrane.

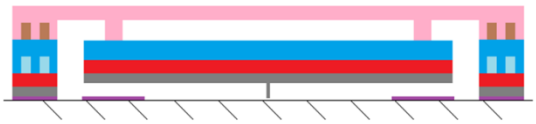

11) Remove the sacrificial oxide using an HF release process.

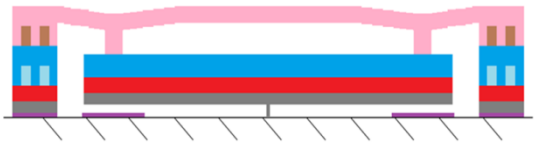

12) Deposit approximately 240 nm of Al_2O_3 by ALD to vacuum-seal the structure.

Figure 6.15: Fabrication process flow for the internal-beam RCMUT design.

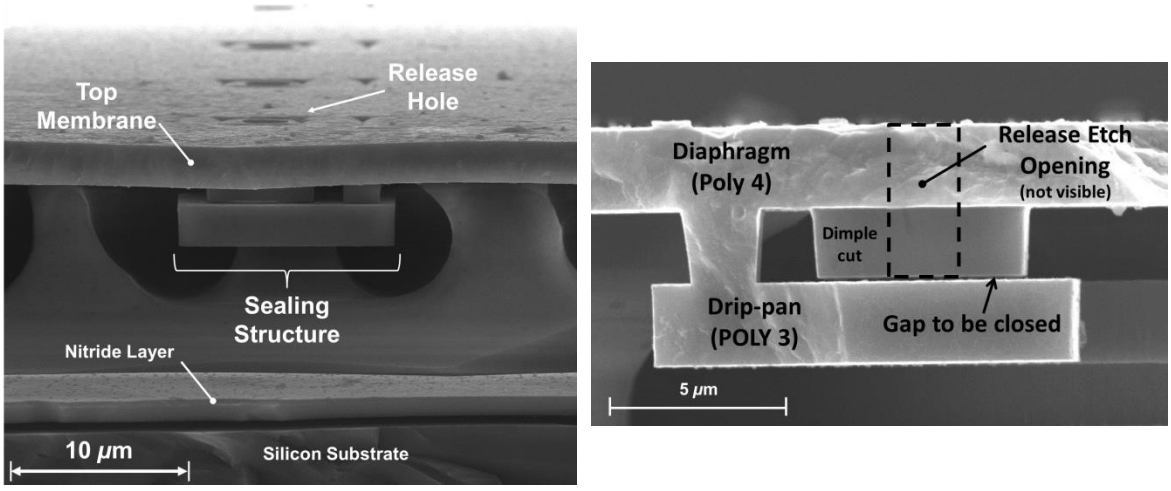

Figure 6.16: Cross-section SEMs of the *drip-pan* structures designed to aid the vacuum-sealing of the internal-beam devices.

D. Modeling and Experimental Evaluation

As noted in the final step of the fabrication process flows depicted in Figures 6.13 & 6.15, the pivot is initially floating upon sacrificial oxide release and touches down after vacuum-sealing due to large atmospheric pressure loading. An accurate model for the deflection of the structure under atmospheric pressure is important in the design phase to ensure the diaphragms do not completely collapse upon sealing, rendering the device useless. Further, modal vibration analysis should take the stress induced by the large deflections resulting from sealing into account. A three-step computation sequence for the sealing deflection and subsequent modal analysis is implemented using ANSYS. A nonlinear solver is required due to the large static deflections in the sealing steps. Referring to Figure 6.17(a), for the *Type-1* external-beam devices, 0.185 atm static pressure is applied to the clamped diaphragms with the beam unconstrained, resulting in 509 nm of diaphragm and beam deflection. This step simulates the pivot touching down to the substrate. Second, the remaining 0.815 atm of ambient pressure is applied to the diaphragms, with the pivot region of the beam constrained from additional vertical

motion. An additional 374 nm of diaphragm deflection occurs as noted in Figure 6.17(b), resulting in a total center-point static diaphragm deflection of 783 nm from the atmospheric loading. The third solution step is modal analysis about the pre-stressed condition using a modal perturbation technique in ANSYS. Figures 6.17(c) and 6.17(d) summarize the first and second eigenmodes, respectively. As desired, the first and fundamental mode is rotational. In a second bending, or *flapping* mode, both diaphragms move in phase.

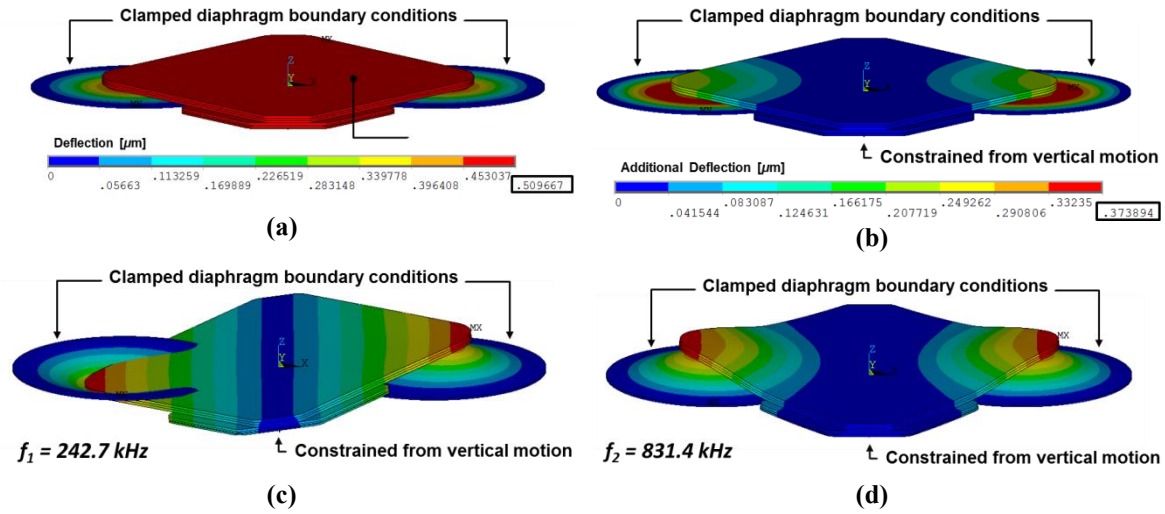

Figure 6.17: Three-step FEA simulation process consisting of (a) simulation of the pivot touchdown, (b) deflection under atmospheric pressure after pivot touchdown, and modal analysis solution for (c) the first mode and (d) the second mode.

(i) Deflection Measurements Upon Sealing

The device model is verified by performing noncontact profilometry measurements on prototypes before and after sealing using a Veeco NT-9100 optical profiler. Figure 6.18(a) presents an image from the optical profiler highlighting the measured cross section, and Figures 6.18(b) and 6.18(c) show the measured profile before and after sealing, respectively. As noted in Figure 6.18(b), the diaphragm profile is

flat before sealing and the center point deflects 805 nm after sealing, just 2.7% difference compared to the simulated value of 783 nm.

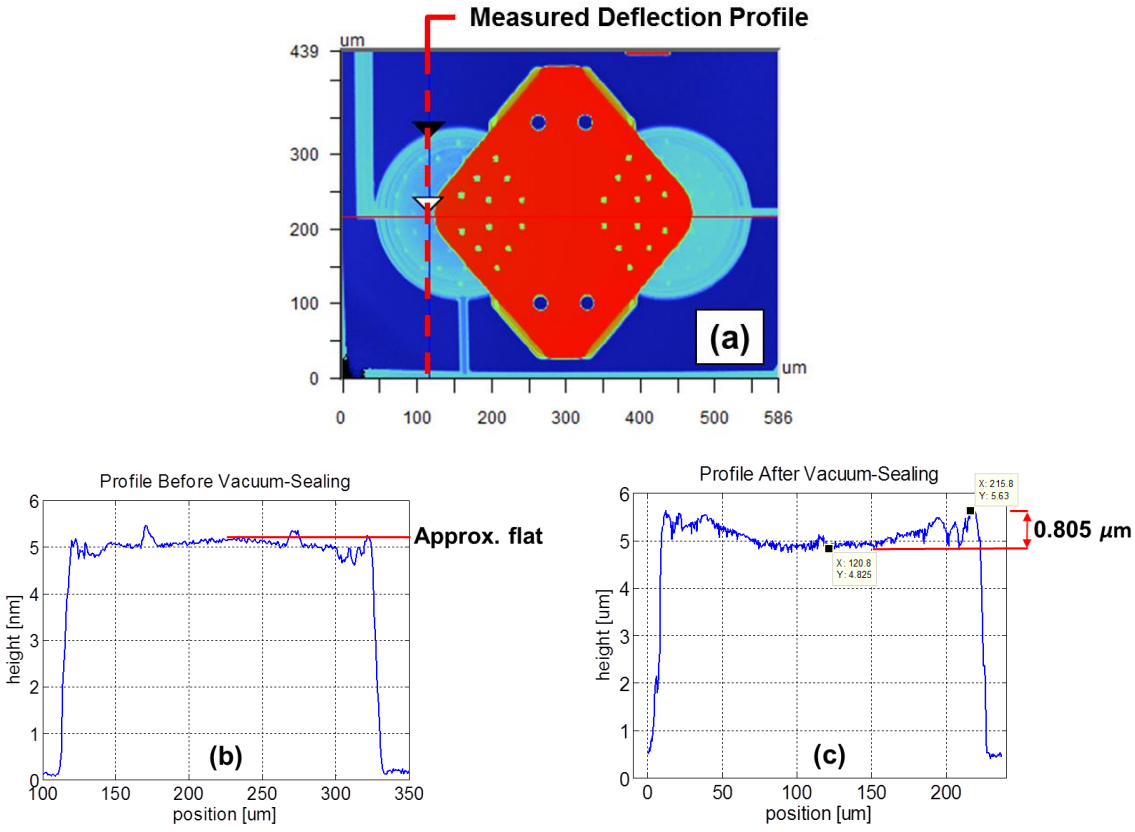

Figure 6.18: Measurement of the device profile with an optical profilometer showing (a) the cross-section to be plotted and the profiles (b) before and (c) after vacuum-sealing.

(ii) Dynamic Frequency Response Measurements

The mode frequencies and overall dynamics of the structure were studied using a laser Doppler vibrometer (LDV) to measure the center-point velocity of the diaphragms while driving them electrostatically using one of the capacitive ports. Figure 6.19 summarizes the measurement configuration. A spectrum analyzer applies an AC actuation signal and sweeps the input frequency while the resulting diaphragm velocity is

measured using the LDV. In the prototype evaluation phase, electrostatic actuation is useful as it enables application of constant amplitude force across a broad frequency range, whereas acoustic evaluation requires careful treatment of diffraction and source limitations, particularly at ultrasonic frequencies. Figure 6.20 presents the measured diaphragm velocity vs. frequency for the two different external beam device types summarized in the Fabrication section. Further, for each device type, the LDV measurement was performed on both the *driven* electrode to which the actuation signal was applied and the *opposing-side* electrode, as labeled in Figure 6.19. There are several interesting features of the measurement: (i) Each response exhibits a first rotational mode and a second bending mode. The rotational nature of the first mode is confirmed using an oscilloscope to observe time-traces of each side of beam and confirming, as shown in Figure 6.21. The traces captured at the first, rotational, mode resonance show a 180° phase difference in diaphragm motion, while the traces captured at the second, bending, mode resonance verify the diaphragms are moving in phase.

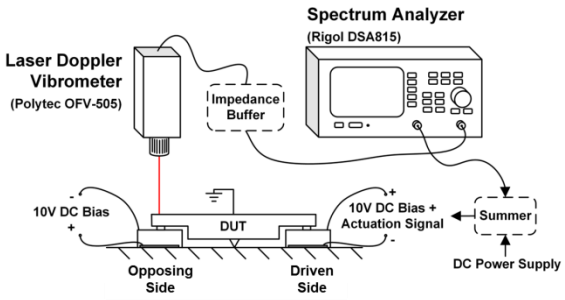

Figure 6.19: Sketch of the setup for measuring electrostatic sensitivity.

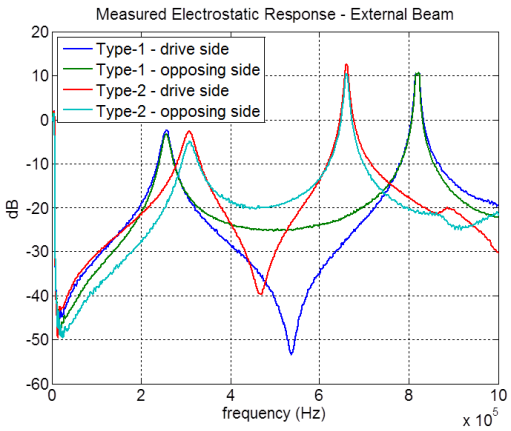

Figure 6.20: Measured electrostatic frequency response of the external-beam devices.

(ii) The *Type-1* oxide beam has a lower first mode resonance and higher second mode resonance as compared to the *Type-2* no-oxide beam device. This observation is in line with intuition, since the oxide-beam is heavier, thereby slowing the first mode, and is stiffer in bending, resulting in a higher second mode frequency. (iii) The presence of anti-resonances in between 400 kHz and 600 kHz for driven side measurements and absence of such anti-resonances for opposing side measurements is explainable. In driven side measurement cases, the diaphragm displacement contributions from the first and second vibration modes are in phase to the left of the fundamental resonance and out-of-phase in between first and second mode resonances, giving rise to the observed anti-resonance.

Similar electrostatic frequency responses for the internal-beam devices are shown in Figure 6.21. Again, the thinner, *Type-2* devices show less separation between the first and second mode frequencies, although the difference is not as stark in this case. Higher-order *twisting* modes are also observed in the *Type-2* response. Both types of internal-beam devices have thinner beams than the external-beam devices, resulting in less separation in the first and second mode frequencies and higher first mode frequencies.

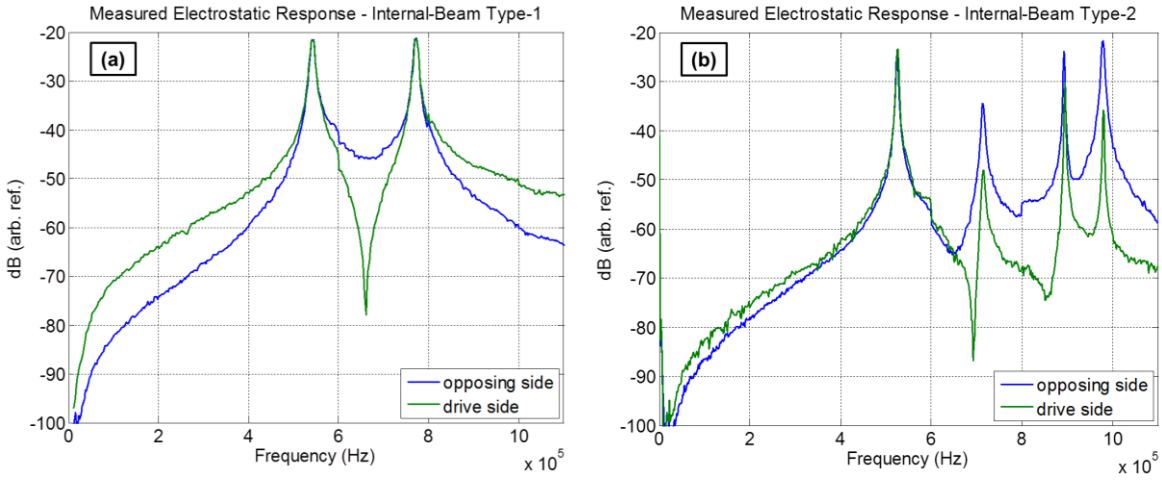

Figure 6.21: Measured electrostatic frequency response of (a) the Type-1 internal-beam devices and (b) the Type-2 devices.

Table 6-1 summarizes the measured first and second mode resonance frequencies, and the corresponding simulated values using the described 3-step finite-element-analysis (FEA) sequence. To assess the importance of the 3-step FEA sequence which takes pre-stresses into account, a simple single-step FEA computation was performed and results are also presented in Table 6-1. The pre-stressed 3-step model results are in closer agreement with measured values. For completeness, resonance Q is also extracted from the measurements and presented in Table 6-1.

Table 6-1.
Measured and Simulated Modal Results

Device Type	**Mode Number**	**Measured Modal Frequencies**	**FEA Simulated Modal Frequencies**		**Measured *Q*-factor**	**Deflection under Atmospheric Pressure**	
			3-step	**1-step**		**Simulated**	**Measured**
External-Beam *Type-1*: 11.3-μm-thick beam	Mode #1 (rotation)	256.5 kHz	242.7 kHz	207.5 kHz	13.9	783 nm	805 nm
	Mode #2 (bending)	818.0 kHz	831.4 kHz	801.7 kHz	126		
External-Beam *Type-2*: 7.0-μm-thick beam	Mode #1 (rotation)	308.2 kHz	288.3 kHz	139.5 kHz	12.1	870 nm	950 nm
	Mode #2 (bending)	659.7 kHz	698.7 kHz	526.3 kHz	75.8		
Internal-Beam *Type-1*: 7.05-μm-thick beam	Mode #1 (rotation)	541.4 kHz	558.2 kHz	617.3 kHz	836	563 nm	330 nm
	Mode #2 (bending)	772.3 kHz	819.3 kHz	889.1 kHz	483		
Internal-Beam *Type-2*: 4.75-μm-thick beam	Mode #1 (rotation)	524.2 kHz	486.2 kHz	496.4 kHz	220	782 nm	1690 nm
	Mode #3 (bending)	714.9 kHz	639.4 kHz	645.8 kHz	155		

(iii) Acoustic Simulation and Measurements

A prototype of the *Type-1* external-beam sensor was configured for capacitive readout of acoustic signals using the circuit in Figure 6.22, configured with discrete surface mount components on a 3-inch diameter circular printed circuit board (PCB) along with the packaged device, as shown in Figure 5.4. C_a and C_b represent the nominal capacitance of two piston diaphragms at opposing ends of a beam, and ΔC is the differential capacitance change resulting from rocking of the beam in response to incoming acoustic pressure gradients. The differential charge, q_{diff}, generated by the device pair flows through feedback network of the charge amplifier with component values summarized in Figure 6.22. ΔC resulting from 1-Pa differential pressure between diaphragms was modeled in ANSYS by computing the capacitance of the pistons at their nominal position after sealing, and again after application 1 Pa pressure to only one of the pistons. The difference in capacitance between states defines a sensitivity of the device in terms of $\Delta C/\Delta P_{diff}$, the change in piston capacitance per 1-Pa differential pressure. For the prototype, $\Delta C/\Delta P_{diff}$ is simulated as 8.5×10^{-19} F/Pa.

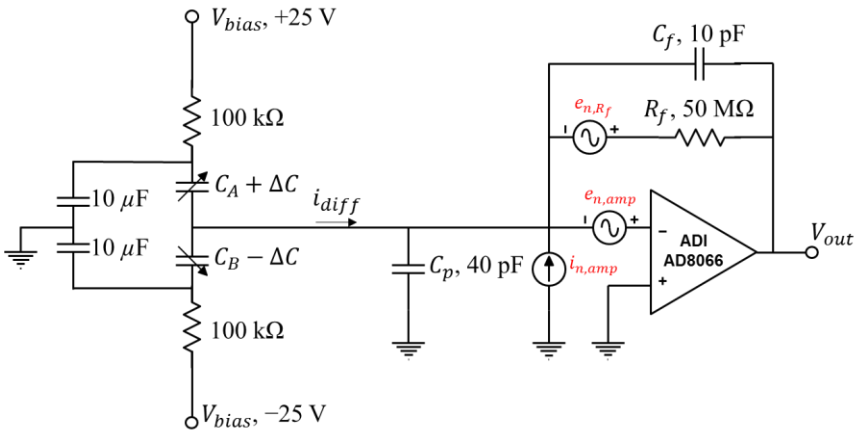

Figure 6.22: Equivalent circuit model of the RCMUT and the dedicated amplifier with noise sources.

The differential pressure generated by an incoming acoustic wave crossing the device depends on acoustic wavelength, or frequency. For plane waves in air, the pressure difference between two points closely spaced compared to a wavelength may be approximated as $|\Delta P_{diff}| = |(dP/dx)\Delta x| = P_0(\omega/c)\Delta x$, where P_0 is the amplitude of the incoming wave, c is speed of sound in air, and Δx is the distance between the points. In summary, the sensitivity of the device defined as ΔC per 1-Pa sound pressure arriving on-axis is,

$$\frac{\Delta C}{P_0} = \left(\frac{\omega}{c}\right) L_{sp} \frac{\Delta C}{\Delta P_{diff}} \quad [\mathrm{F/Pa}] \tag{6-1}$$

where L_{sp} is the spacing between pistons and is equal to 276 μm for the prototype. For the particular charge-amplifier configuration summarized in Figure 6.22, $q_{diff} = 2V_{bias}\Delta C$, where the factor of two results from the differential readout. The simulated amplifier output, V_{out}, in response to a 1-Pa amplitude sound wave (i.e., 94-dB SPL) is presented in Figure 6.23. The 20-dB/decade slope is as expected following equation (6-1). Internal noise sources of the op-amp and Johnson-Nyquist noise of the feedback resistor are also shown in Figure 6.22 and V_{out} due to each of these sources individually are presented in Figure 6.23 along with the total simulated output noise.

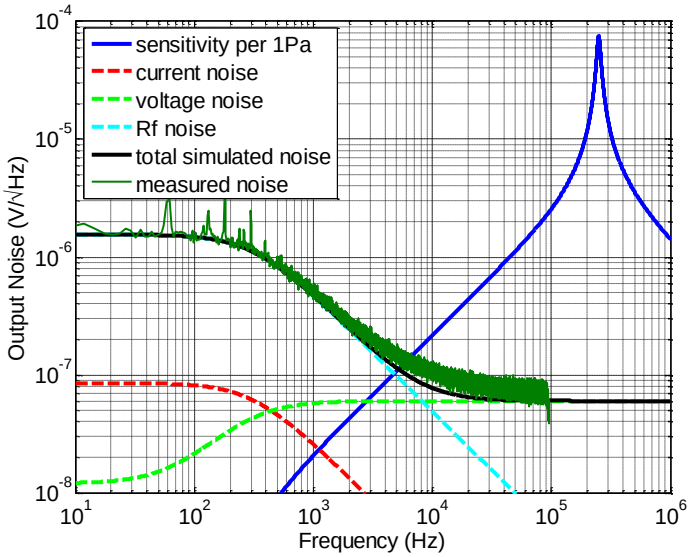

Figure 6.23: Measured noise compared to simulated noise and sensitivity.

Acoustic measurements were performed in a 10' × 10' × 10' walk-in anechoic test chamber to verify successful detection of sound waves. Rigorous acoustic frequency response characterization of this first generation prototype is challenging for several reasons. Characterization at low frequencies is difficult due to poor sensitivity of the prototype. In light of equation (6-1), the sensitivity is proportional to ω and L_{sp}. Referring to the simulated sensitivity and total noise in Figure 6.23, signal-to-noise ratio (SNR) is greater than unity only above 5 kHz. Rigorous acoustic characterization at high frequencies is difficult due to scattering of sound by the PCB-based package, which is designed for maximum versatility in the prototype phase rather than small acoustic form factor. High frequency testing is also difficult due to unavailability of broadband sources at high frequencies. Single tone testing is, however, feasible at high frequencies and verifies successful detection of ultrasonic waveforms. A piezoelectric buzzer was used for testing reception of sound waves. The on-chip reference microphone labeled in Figure 6.4 has a +/- 3 dB bandwidth of 20 Hz – 250 kHz and a known sensitivity equal to 15.1

μV/Pa from calibration against an instrumentation microphone model G.R.A.S. Type 40AC, as described in a pending journal publication [79]. The omnidirectional reference microphone was used as an on-chip calibration reference for the RCMUT tests. A spectrum analyzer, Rigol DSA-815-TG, was used to capture the reference microphone and RCMUT signals at a few discrete ultrasonic frequencies corresponding to narrowband resonances of the piezoelectric buzzer. Figure 6.24 presents the spectrum analyzer output for a measurement near 132 kHz. The computed sensitivity from the measurement is,

$$S_{RCMUT} = \frac{2.71\,\mu\text{V}}{6.92\,\mu\text{V}} S_{Refmic} = 5.9\,\mu\text{V/Pa} \tag{6-2}$$

which is in relatively close agreement with the simulated value at 132 kHz presented in Figure 6.23. The output noise of the sensor was also measured and agrees with predictions following the noise model in Figure 6.23.

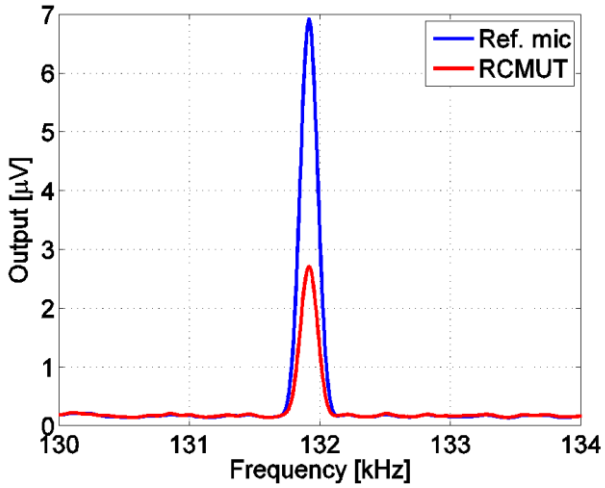

Figure 6.24: Single frequency measurement of the reference microphone and RCMUT at 131.9 kHz.

E. Discussion & Conclusions

The motivation for this work is to explore a new type of surface micromachined microphone in the form of two vacuum-sealed pistons connected by a pivoting beam structure. The driving idea is that vacuum-sealing has the potential to eliminate thermal mechanical noise as a dominant noise contributor in small-scale capacitive microphones, while the pivoting beam between vacuum-sealed pistons decouples in-plane rotational stiffness from bending stiffness. The decoupling is significant as it enables the device to potentially be compliant in response to small in-plane pressure gradients while remaining rigid against the much larger atmospheric background pressure. Initial prototypes were designed as ultrasonic sensors, which successfully demonstrate the device concept and the microfabrication feasibility of a relatively complex MEMS structure. Further, this work presents the successful demonstration of a first-its-kind CMUT, in which the fundamental resonance mode is a rotational or rocking mode. Single devices 500 μm × 400 μm in size successfully resist collapse under vacuum-sealing and respond to airborne ultrasonic pressure gradients, albeit with limited SNR. Specifically, from Figure 6.23, the SNR in a 1-Hz bin at 100 kHz is 34 dB.

In future generations of the capacitive pressure gradient sensor, sensitivity, and hence SNR, can be improved by using an array of sensors summed electrically in parallel as is commonly done with CMUT imaging arrays. The gain in SNR is expected to be proportional to N, since the noise of the prototype is limited by electronic noise and a single amplifier would still be used in the parallel summed array. The single sensor presented occupies 500 μm × 400 μm, so a 2 mm × 2 mm array would fit 20 cells and yield 26-dB higher SNR than an individual prototype sensor. The design challenges encountered in further attempting to increase device sensitivity are illuminated by equation (6-1). Increasing space between pistons, L_{sp}, improves SNR but can also reduce

the structure's ability to resist collapse under atmospheric pressure. Use of thicker beams and/or stiffer materials for the beam is therefore advantageous. $\Delta C/\Delta P_{diff}$ may be thought of as the product of two component sensitivities, as

$$\frac{\Delta C}{\Delta P_{diff}} = \left(\frac{\Delta C}{\Delta h}\right)\left(\frac{\Delta h}{\Delta P_{diff}}\right) \tag{6-3}$$

where h is the area averaged deflection of a piston. For gap-closing type capacitance transducers, $\Delta C/\Delta h = C_0/h_0$, so increasing piston area and decreasing the nominal piston gap height are paths to increasing SNR. The second term in equation (6-3) is the compliance to differential pressure, which is determined by the compliance of the pistons at opposing ends of the beam. Pistons with higher compliance are therefore advantageous, but will also make resilience against collapse more difficult to achieve. The rigorous navigation of this design space to discover achievable SNR is the subject of future work.

Chapter VII: Source Localization using a Single Microphone

A. INTRODUCTION

This chapter describes the application of the sensors developed in this work to the localization of sound[4]. Specifically, it is demonstrated that a single acoustic sensor can be used to track the location of a sound source on a 2-D plane to a high degree of accuracy. The localization mechanism illustrates the biomimetic nature of the sensors presented in this work. It has been discovered that the parasitoid fly *ormia ochracea* has the remarkable ability to detect the direction of incident audible sound even though the fly's hearing mechanism spans only a 1.5 mm distance [86]. At 5 kHz, this distance is much smaller than wavelength of sound in air (approximately 2.2%). Hoy and Miles performed pioneering research aimed at understanding, through experimentation and a mechanical model of the fly's hearing mechanism, how the fly performs the remarkable task [20]. Their work discovered that the hearing structure employed by the fly uses two modes of vibration which serve to amplify interaural time and level differences. The discovery, in turn, inspired several research teams to explore the biomimicry of the design to realize microphones with the same abilities. The unique structure of the hearing mechanism combined with the small size poses significant transduction-related research challenges. Micromachined prototypes employing optical and capacitive transduction have been demonstrated [23, 26, 29, 32, 33]. However, capitalizing on the innovative multiple-vibration-mode structure requires transducing motion of the structure independently at multiple locations, which, to-date, has not been demonstrated with any previous design. Both sensors in this work, however, have the necessary multiple-port readout necessary

[4] Content in this chapter to appear in similar form in:
M. L. Kuntzman and N. A. Hall, "Sound source localization inspired by the ears of the *ormia ochracea*," submitted to *Appl. Physics Lett.* for publication.

to take full advantage of the localization potential of the biomimetic design integrated directly into the sensor design.

This chapter presents sound localization experiments showing the use of the piezoelectric microphone to mimic sound localization by a method presumably similar to that used by the *ormia ochracea*, with simultaneous transduction of orthogonal modes using multiple sensing ports. To our knowledge, this work thus presents the most emulative mimic of the *ormia ochracea* to date, as the prototype is fully integrated, similar in size to the *ormia ochracea*, and with identical capabilities as demonstrated in this chapter through sound localization experiments conducted at 2 kHz. In what follows, the theory of device as applied to sound localization is summarized and followed by a presentation of sound localization experiments. Although the piezoelectric sensor is used in this chapter to illustrate the method, the RCMUT sensor also possesses the necessary multiple-mode, multiple-port nature that the method requires and, as such, is also well-suited to source localization applications using the method presented in this chapter.

B. DEVICE MODEL APPLIED TO SOURCE LOCALIZATION

As was previously noted in Chapter 4, the motion of the structure at any frequency may be described as a superposition of first and second mode vibrations, or $u(x,t) = \eta_1(t)\psi_1(x) + \eta_2(t)\psi_2(x)$ where $\eta_1(t)$ and $\eta_2(t)$ are complex amplitudes of vibration for the first and second modes, respectively. The first vibration mode of the structure is only responsive to the x-component of pressure gradient and is not excited by omnidirectional sound pressure. Conversely, the second mode of vibration is only excited by omnidirectional pressure and is unresponsive to pressure gradients along the x-axis. The device therefore encompasses the underlying principle of operation of the *ormia*

ochracea hearing mechanism as first discovered and presented by Miles and Hoy [20]. Formally,

$$\eta_1 \propto \frac{\partial P}{\partial x} \tag{7-1}$$

$$\eta_2 \propto j\omega P_o \tag{7-2}$$

The leading $j\omega$ term in equation (7-2) arises from the influence of the slot resistance and back cavity compliance, as discussed in Chapter 4.

A planar sound wave traveling in the x-z plane and incident upon the device from angle theta, as depicted in Figure 7.1, may be expressed as

$$p(x,t) = P_o e^{jkx\cdot cos(\theta)} e^{j\omega t} \tag{7-3}$$

where $k = \omega/c$ is the acoustic wave number and c is the velocity of sound in air. The pressure loading onto the device is well approximated by the first-order Taylor series expansion:

$$p(x,t) = p(x,t)\big|_{x=0} + x\frac{\partial p}{\partial x}\bigg|_{x=0} \tag{7-4}$$

such that the loading of the device at any instant is comprised of an omnidirectional pressure component, $P_o e^{j\omega t}$, and a pressured gradient component,

$$\frac{\partial p}{\partial x} = \frac{j\omega P_o}{c}\cos(\theta) \tag{7-5}$$

In light of relations in equations (7-1) and (7-2), first and second mode vibrations are therefore expected to be either in-phase or 180 degrees out-of-phase, depending on $\cos(\theta)$ (i.e. in-phase for waves arriving from the right, and out-of-phase for waves arriving from left).

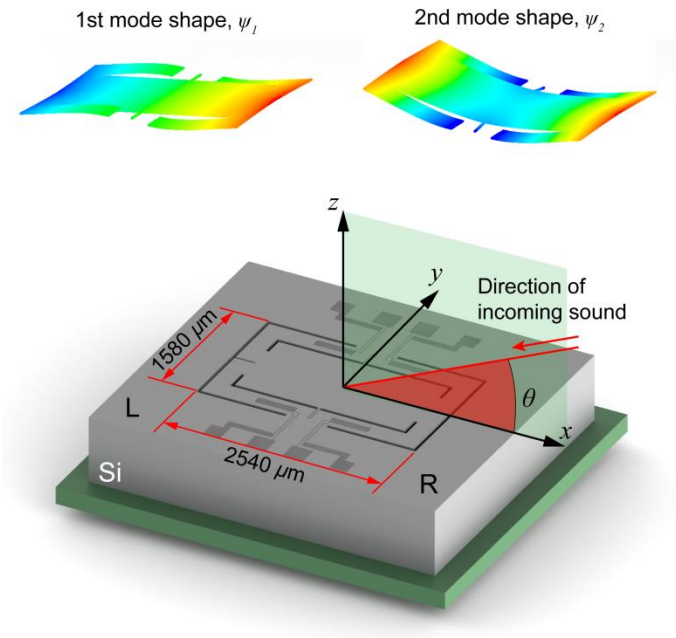

Figure 7.1: Illustration of sound incident on the microphone at an angle, θ, in the x-y plane.

First-mode displacements may be sensed by subtracting signals from the left and right ports as such differential readout cancels second mode displacement signals. Conversely, second-mode displacements may be sensed by summing signals from left and right ports, as this summation cancels differential mode signal. Since port signals are available simultaneously in real-time, both common-mode and differential signals are available in real-time. If the signals are voltages with complex amplitudes denoted V_L and V_R, respectively, the summed and differential signals are expected to follow

$$V_R + V_L = V_{Omni} = P_o S_{omni} \tag{7-6}$$

$$V_R - V_L = V_{grad} = P_o S_{pk} \cos(\theta) \tag{7-7}$$

where S_{omni} is an omnidirectional sensitivity and S_{pk} is the peak on-axis sensitivity of the pressure gradient mode. Two unique features of the device follow from equations (7-

6) and (7-7), with each described separately in the following sections. The first is that the device makes available, simultaneously, different directivity patterns from different sensing ports on the device. The second is the ability to compute, with a single sensing structure, the angle of sound incidence.

C. INDIVIDUAL PORT DIRECTIVITIES

Equations (7-6) and (7-7) may be solved simultaneously to yield expressions for the anticipated signal output from individual ports V_L and V_R. The expressions are

$$V_R = \tfrac{1}{2}\left[S_{omni} + S_{pk}\cos(\theta)\right] \tag{7-8}$$

$$V_L = \tfrac{1}{2}\left[S_{omni} - S_{pk}\cos(\theta)\right] \tag{7-9}$$

Experimental confirmation of anticipated device operation is obtained via individual port directivity measurements performed in an anechoic chamber as summarized in Figure 7.3. Referring to Figure 7.2 either port 1 or 4 may be used for the *right* port, and either 2 or 3 may be used for the *left* port. Short-circuit charge from ports 1 and 2 were input into separate charge amplifiers to produce signals V_R and V_L, respectively, as labeled in Figure 7.3. The studio monitor was used to generate a continuous wave (CW) signal at 2 kHz, and the magnitudes of the V_L and V_R signals were measured at multiple angles of incidence using an FFT-based Prism dScope Series III Audio Analyzer to produce the directivity plots summarized in Figure 7.4. As expected following equation (7-8), the polar response of port 1 has a maximum at an incidence angle of zero degrees and a minimum at 180 degrees. Similarly, as expected following equation (7-9), port 3 has a maximum at 180 degrees, and a minimum at zero degrees. Following equations (7-8) and (7-9), the summed port signals are expected to yield an omnidirectional pattern, $V_R + V_L = S_{omni}$. This summation signal was also made

available in real-time using a summation amplifier, and its signal amplitude also recorded and plotted in Figure 7.4 for each angle of incidence. The measured polar response is not precisely omnidirectional due to imperfections and asymmetries in the prototype, but the measurement demonstrates proof of concept and a unique feature of the device: Multiple directivity patterns are simultaneously made available in real time using multiple sensing ports across the device.

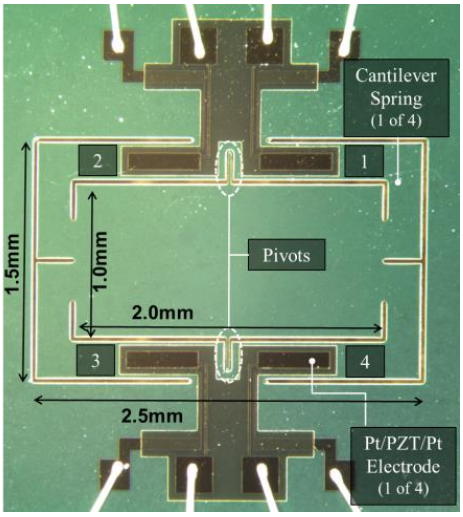

Figure 7.2: Micrograph with port numbers labeled.

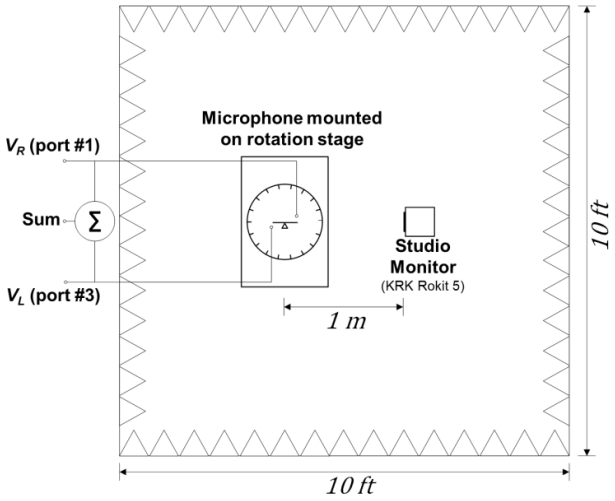

Figure 7.3: Illustration of the measurement setup in the anechoic chamber.

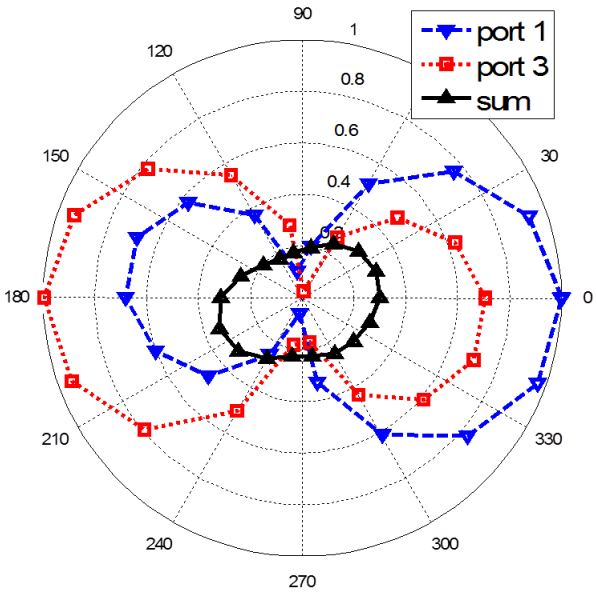

Figure 7.4: Measured directivities at 2 kHz.

D. SOUND SOURCE LOCALIZATION

Simultaneous detection of sound pressure and pressure gradient enables the angle of sound incidence to be computed. Referring to equations (7-6) and (7-7),

$$cos(\theta) = \frac{V_{grad}}{P_o S_{pk}} = \frac{V_{grad}/V_{omni}}{S_{pk}/S_{omni}} = \frac{V_{grad}/V_{omni}}{\left[V_{grad}/V_{omni}\right]_{\theta=0}} \tag{7-10}$$

The final form of equation (7-10) makes use of the fact that S_{pk}/S_{omni} is equal to the measured ratio of V_{grad}/V_{omni} at zero degrees, as can be noted from equations (7-6) and (7-7). The direction of sound incidence may be computed using equation (7-10) and requires measurement of V_{grad} and V_{omni}. Measurements were made at several controlled incidence angles with the results summarized in Table 7-1. The measurement at zero degrees determines the ratio of S_{pk}/S_{omni} as 5.7. For the remaining cases, angle of incidence is computed using equation (7-10). As noted in the final column of Table 7-1,

the measured angle is in close agreement with the known input angle. Table 7-1 data emphasizes the device's ability to unambiguously determine whether sound waves arrive from the left or right of the device. For waves arriving from the right, $|V_R| > |V_L|$, and a positive $\cos(\theta)$ value results. Similarly, waves arriving from the left produce $|V_R| < |V_L|$ and result in negative $\cos(\theta)$ values corresponding to arrival from the left plane.

Table 7-1.
Sound Localization Experiment Results

θ [degrees]	$\lvert V_R \rvert$ [μV]	$\lvert V_L \rvert$ [μV]	$\lvert V_R + V_L \rvert = \lvert V_{omni} \rvert$ [μV]	$\lvert V_R - V_L \rvert = \lvert V_{grad} \rvert$ [μV]	θ_{meas} [degrees]
40	55.74	35.26	20.60	91.00	39.2
80	14.83	2.04	14.72	16.87	78.4
220	34.60	58.17	23.56	-92.77	226.3
240	18.64	37.03	19.74	-55.67	240.4
260	4.42	13.55	16.81	-17.97	259.2
360	73.23	51.57	21.90	124.8	358.7

E. SUMMARY AND DISCUSSION

Resonance frequencies of the prototype device are positioned closely together and near the top end of audio bandwidth. As a result, both mode responses, η_1 and η_2, increase linearly with frequency: η_1 due to an omega term in equation (7-5), and η_2 due to an omega term in equation (7-2). As a consequence, the shapes and relative amplitudes of the directivities in Figure 7.4 are expected to be independent of frequency. Such a design enables localization of broadband sources without the need for spectral processing or digital signal processing. For broadband signals, the use of simple *rms* values for V_{grad} and V_{omni} in equation (7-10) are sufficient for angle computation. We also note that the beam in the presented prototype has two springs at each end which are redundant for

orthogonally sensing the first and second vibration modes. Only two ports are needed, as demonstrated here with use of ports 1 and 3. Future embodiments may extend the device concept to mechanical designs that have a third *torsional* or *twisting* mode of the beam, in which case it may be possible to simultaneously sense gradients in both x and y-directions.

Chapter VIII: Conclusions and Future Work

This work studied two novel MEMS acoustic sensor designs, both inspired by the hearing mechanism of the fly *ormia ochracea* and early microphone designs attempting to mimic the fly's hearing mechanism [20, 23]. The first sensor uses piezoelectric readout to reduce the complexity compared to earlier designs relying on optical readout [23, 26]. The second sensor sought to adapt the biomimetic structure to create a vacuum-sealed acoustic pressure gradient sensor. A vacuum-sealed microphone would have the advantages of greatly reduced thermal-mechanical noise and purely surface-micromachined construction. Prototypes of both sensors were designed, fabricated, and characterized, providing proof-of-concept of both the fabrication and operating principle of the sensors. Both an analytical first-mode and a multi-mode, multi-port model was developed and applied to the sensors, laying down the theoretical framework to explore the design space for future generations of the sensors with improved performance.

The challenge of future generations of both sensors will lay largely in pushing the limits of the fabrication process. The key to improving the performance of both sensors lays in increasing compliance for maximum sensitivity. For the piezoelectric microphone, the springs must be made thinner to increase compliance, without comprising the structural integrity of the device. For the vacuum-sealed sensor, the diaphragms determine the compliance of the first mode. Designs with increased sensitivity will rely on stiffer beam structures, which will allow for larger, more compliant diaphragms. Higher beam stiffness could be achieved by moving from silicon to higher Young's modulus materials, such as diamond or silicon carbide or by increasing the thickness of the beam. To streamline fabrication and avoid long LPCVD film depositions, the beam

structure could feasibly be fabricated using a process in which the rotational beam is patterned from the device layer of an SOI wafer.

The sound localization ability of the biomimetic design was demonstrated using the piezoelectric microphone. The biomimetic structure simultaneously measures pressure magnitude and in-plane pressure gradients. The modal contributions add constructively on the side of the microphone closest to the sound source and destructively on the opposing side of the device. By comparing the signal amplitude at ports on opposing sides of the microphone it is determined whether the sound source is in front of or behind the microphone. The specific angle of source relative to the microphone is then determined by comparing the amplitude of the pressure gradient measurement to the reference omnidirectional pressure magnitude measurement. The angle is calculated from the ratio of the pressure magnitude and pressure gradient measurements. This work demonstrated, for the first time, sound localization in a two dimensional plane using a single, multiple-port microphone. Although not demonstrated in this work, the vacuum-sealed microphone is expected to possess the same sound localization capability.

The sound localization capability of the microphone could be enhanced by combining two of the in-plane pressure gradient microphones with a previously introduced out-of-plane pressure gradient microphone, which was designed using the same fabrication process flow [39], to realize a 3-axis pressure gradient probe. Such a probe would allow the measurement of the 3-dimensional acoustic particle velocity vector at a single point in space, which could allow for new innovations in acoustic localization, noise rejection, and other acoustic signal processing applications.

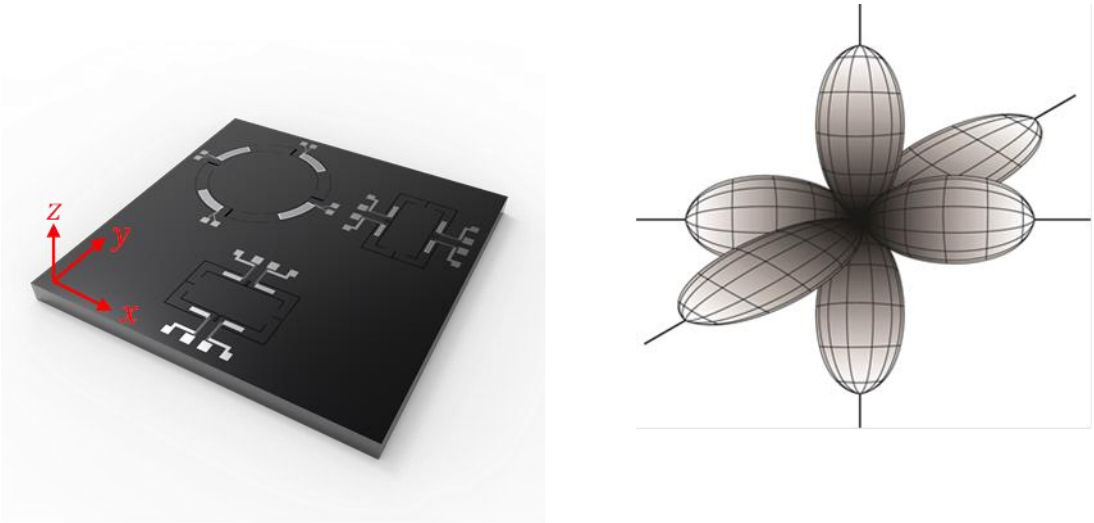

Figure 8.1: CAD rendering of a proposed 3-axis acoustic vector sensor.

Appendix A: ANSYS Scripts

ANSYS Script Modal Analysis of Piezoelectric Microphone

```
!!! Quad wafer Device #1
!!! Geometry built in ansys
!!! MKS units
finish
/clear, nostart
/filename, XY_2014_1kHz

/PREP7
ES_pzt=10e-6   ! element size for PZT volume mesh
ES=40e-6       ! element size for device mesh
nelec=4        ! number of electrode pairs
pi=3.14159265  ! pi

!!!!!!!!!!!!!!!!!!!!!!!!!!!!!!!!!!!!!!!!!!!!!!!!!!
!!!!!!!!!!!!!!!!!! User Input !!!!!!!!!!!!!!!!!

freq=0         ! Frequency for pres differential loading (Harm MSUP analysis)
               ! (freq=0 for DC)
num_div=10     ! num of divisions to use for applying pres dif load
clamped=1      ! (0 for hinged BC; 1 for clamped)

!!!!!!!!!!!!!!! Parameters
!Beam
w=1000e-6      ! beam width
l=2000e-6      ! beam length
t=-20e-6       ! epi layer thickness

!Springs
sw=250e-6      ! spring width
gap=20e-6      ! gap between springs & beam
st=-20e-6      ! spring thickness
dist=230e-6    ! distance from center of beam to start of spring

! Electrode dimensions
Le=464e-6      ! top electrode length
We=105e-6      ! top electrode width
te=1e-6        ! PZT thickness

! Hinge
hw=t           ! pivot width
ht=t           ! pivot thickness
pl=50e-6       ! pivot length
```

```
!!!!!!!!!!!!! Element types & Material Properties
ET,1,solid186                   ! poly silicon
mp,ex,1,160e9                   ! youngs mod, poly (Pa)
mp,dens,1,2330                  ! density, poly (kg/m^3)
mp,nuxy,1,0.23                  ! poisson's ratio, poly

ET,2,solid226,1001              ! PZT (1001=piezoelectric)
MP, DENS, 2, 7500               ! Density of PZT [kg/m^3]

! Anisotropic material properties for PZT-5H (from Gabrielson notes)
C11 = 127E+9                            !C [N/m^2]
C12 = 80.2E+9                           !C [N/m^2]
C13 = 84.7E+9                           !C [N/m^2]
C33 = 117E+9                                    !C [N/m^2]
C44 = 23.0E+9                           !C [N/m^2]
C66 = 23.5E+9                           !C [N/m^2]

TB, ANEL, 2, , , 0                      ! TBOPT 0; stiffness matrix (C_E matrix) [N/m^2]
TBDATA, 1, C11, C12, C13
TBDATA, 7, C11, C13
TBDATA, 12, c33
TBDATA, 16, C44
TBDATA, 19, C44
TBDATA, 21, C66

! Piezoeletric Constant Matrix for PZT-5H
e31 = -6.62                             ! [C/m^2]
e33 = 23.2                              ! [C/m^2]
e15 = 17.0                              ! [C/m^2]

TB, PIEZ, 2, , , 0          ! TBOPT 0; Piezoelectric Stress Matrix ([e] matrix) [C/m^2]
TBDATA, 3, e31
TBDATA, 6, e31
TBDATA, 9, e33
TBDATA, 14, e15
TBDATA, 16, e15

! Permittivity Matrix for PZT-5H
EMUNIT, EPZRO, 8.854E-12                ! Free-space Permittivity [F/m]
TB, DPER, 2, , , 0                      ! Relative Permittivities at constant stain
TBDATA, 1, 1710, 1710, 1430             ! in matrix form

!!!!!!!!!!!!! Build geometry
blc5,0,0,l,w,t                          ! beam
blc5,0,-w/2,hw,2*pl,ht                  ! lower hinge
blc5,0,w/2,hw,2*pl,ht                   ! upper hinge
blc4,-l/2-sw-gap,-gap/2-sw,gap+sw,sw,st ! lower left spring
```

```
blc4,-l/2-sw-gap,-w/2-gap,sw,gap/2+w/2,st
blc4,-l/2-sw-gap,-w/2-gap-sw,sw+gap+l/2-230e-6-Le,sw,st
blc4,-dist-Le,-w/2-gap-sw,Le,(sw-We)/2,st          !below electrode
blc4,-dist-Le,-w/2-gap-(sw-We)/2,Le,(sw-We)/2,st   !above electrode
blc4,dist,w/2+(sw-We)/2+gap,Le,We,st               !under electrode (top right)
vsymm,x,9                                          !mirror under electrode
vsymm,y,9,10                                       !mirror under electrode
vsymm,x,4,8,1                                      !mirror spring x
vsymm,y,4,8,1                                      !mirror spring y
vsymm,y,13,17,1                                    !mirror spring y
allsel,all
vovlap,18,19
vovlap,23,24
vovlap,13,14
vovlap,4,5
vovlap,1,2,3

! Create PZT regions
blc4,dist,w/2+(sw-We)/2+gap,Le,We,te  ! PZT 1, V1
vsymm,x,1                                          ! PZT 2, V2
vsymm,y,1,2                                        ! PZT 3,4: V3,48
allsel,all
vglue,all

!!!!!!!!!!!!! Volume numbers
! Si       all other
! PZT    V4,5,34,35
!!!!!!!!!!!!!!!!!!!!!!!!!!

vsel,s,,,1,3,1
vsel,a,,,48

!!!!!!!! Mesh PZT volumes
type,2
mat,2
MSHAPE,0,3d                  ! 0-quad, 1-triangular
esize,ES_pzt
VMESH,all
allsel,all
vsel,u,,,1,3,1
vsel,u,,,48

!!!!!!!! Mesh Silicon volumes
type,1
mat,1
MSHAPE,1,3d                  ! 0-quad, 1-triangular
esize,ES
```

```
VMESH,all

allsel,all
!Set View
/VIEW,,0,1,0                    ! View axis
/REP
/ANG,,180,XM,1                  ! Rotation angle
/REP
/ANG,,20,XM,1                   ! Rotation angle
/REP

!!!!!!!!!!!!  Apply Mechanical Boundary Conditions
asel,s,,,272                    ! Spring 1 areas
asel,a,,,235
asel,a,,,277
asel,a,,,268                    ! Spring 2 areas
asel,a,,,215
asel,a,,,263
asel,a,,,287                    ! Spring 3 areas
asel,a,,,219
asel,a,,,282
asel,a,,,42                     ! Spring 4 areas
asel,a,,,229
asel,a,,,48
DA,all,all,0                    ! Spring end BCS
allsel,all

*if,clamped,eq,1,then
        /com
        /com CLAMPED PIVOT BOUNDARY CONDITION
        asel,s,,,9              ! hinge BCs
        asel,a,,,16
        DA,all,ux,0
        DA,all,uy,0
        DA,all,uz,0
        allsel,all

*elseif,clamped,eq,0
        /com
        /com HINGED PIVOT BOUNDARY CONDITION

        nsel,s,loc,x,0          ! Hinge 1
        nsel,r,loc,y,w/2+pl
        nsel,r,loc,z,ht/2
        D,all,ux,0
        D,all,uy,0
        D,all,uz,0
```

```
        allsel,all

        nsel,s,loc,x,0                  ! Hinge 2
        nsel,r,loc,y,-w/2-pl
        nsel,r,loc,z,ht/2
        D,all,ux,0
        D,all,uy,0
        D,all,uz,0
        allsel,all
*endif

!!!!!!!!!!!!! Define bottom electrodes and apply BCs
seltol,1e-15
nsel,s,loc,z,0                                  ! Bottom Electrode 1
nsel,r,loc,x,dist,dist+LE
nsel,r,loc,y,w/2+(sw-We)/2+gap,w/2+(sw-We)/2+gap+We
cp,next,volt,all
*get,bot1,node,0,num,min                        ! Get master node

nsel,s,loc,z,0                                  ! Bottom Electrode 2
nsel,r,loc,x,dist,dist+LE
nsel,r,loc,y,-w/2-(sw-We)/2-gap,-w/2-(sw-We)/2-gap-We
cp,next,volt,all
*get,bot2,node,0,num,min                        ! Get master node

nsel,s,loc,z,0                                  ! Bottom Electrode 3
nsel,r,loc,x,-dist,-dist-LE
nsel,r,loc,y,-w/2-(sw-We)/2-gap,-w/2-(sw-We)/2-gap-We
cp,next,volt,all
*get,bot3,node,0,num,min                        ! Get master node

nsel,s,loc,z,0                                  ! Bottom Electrode 4
nsel,r,loc,x,-dist,-dist-LE
nsel,r,loc,y,w/2+(sw-We)/2+gap,+w/2+(sw-We)/2+gap+We
cp,next,volt,all
*get,bot4,node,0,num,min                        ! Get master node


!!!!!!!!!!!!! Select and group top electrode nodes


!*dim,ntop,array,nelec          ! define an array to store bot electrode node numbers
!*dim,Qsc,array,nelec           ! define an array to store Qsc values for each electrode pair
nsel,s,loc,z,te                 ! Top Electrode 1
nsel,r,loc,x,dist,dist+LE
nsel,r,loc,y,w/2+(sw-We)/2+gap,w/2+(sw-We)/2+gap+We
cp,next,volt,all
```

```
*get,top1,node,0,num,min                    ! Get master node

nsel,s,loc,z,te                             ! Top Electrode 2
nsel,r,loc,x,dist,dist+LE
nsel,r,loc,y,-w/2-(sw-We)/2-gap,-w/2-(sw-We)/2-gap-We
cp,next,volt,all
*get,top2,node,0,num,min                    ! Get master node

nsel,s,loc,z,te                             ! Top Electrode 3
nsel,r,loc,x,-dist,-dist-LE
nsel,r,loc,y,-w/2-(sw-We)/2-gap,-w/2-(sw-We)/2-gap-We
cp,next,volt,all
*get,top3,node,0,num,min                    ! Get master node

nsel,s,loc,z,te                             ! Top Electrode 4
nsel,r,loc,x,-dist,-dist-LE
nsel,r,loc,y,w/2+(sw-We)/2+gap,+w/2+(sw-We)/2+gap+We
cp,next,volt,all
*get,top4,node,0,num,min                    ! Get master node

!*do,i,1,nelec
!d,ntop(i),volt,0          ! Top electrodes grounded (effectively short-circuit)
!*enddo

!!!!!! Apply electrode boundary conditions
allsel,all
d,bot1,volt,0
d,bot2,volt,0
d,bot3,volt,0
d,bot4,volt,0

d,top1,volt,0
d,top2,volt,0
d,top3,volt,0
d,top4,volt,0
allsel,all
finish

!!!!!! Define arrays needed to store spring modeshape values !!!!!!!!!!
Ls=L/2-dist                 ! spring length
delx=Ls/div                 ! space between evaluation points
x_loc=dist                  ! start of spring
y_loc=w/2+gap+sw/2          ! y value of middle of spring
*dim,x_nodes,array,div+1    ! array to store spring modeshape values
*dim,s_loc,array,div+1      ! array to store spring location values
seltol,ES/2                 ! no nodes selected if seltol too small
```

```
*do,i,1,div+1
        s_loc(i)=x_loc-dist             ! store position relative to spring start
        allsel,all
        nsel,s,loc,z,0
        nsel,r,loc,x,x_loc              ! select node at position on spring
        nsel,r,loc,y,y_loc
        *get,x_nodes(i),node,,num,min ! Get node at current location
        x_loc=x_loc+delx                ! increment x-location
        /com
        /com x_nodes = %x_nodes(i)%
        /com s_loc = %s_loc(i)%
        /com
*enddo
seltol,1e-15                            ! restore to previous value


!!!!!!!!!!!!!!!Modal Analysis!!!!!!!!!!!!!!!!!!
/SOLU
ANTYPE,MODAL                ! Select modal analysis type
MODOPT,LANB,2               ! Select the Block Lanczos mode-extraction method
MXPAND,2,,,Yes

! Select beam tip master node for modeshape evaluation
allsel,all
nsel,s,loc,x,l/2
nsel,r,loc,y,0
*get,ntip,node,0,num,min       ! Get master node at beam tip
allsel,all

! Apply load for MSUP Harmonic Analysis
*if,freq,eq,0,then
        /com
        /com DC LOADING CONDITION
        seltol,1e-15

        nsel,s,loc,z,,0             ! select surface nodes
        sf,all,pres,1               ! apply 1 Pa pressure
        allsel,all

*elseif,freq,ne,0
        /com
        /com PRESSURE DIFFERENTIAL LOADING CONDITION
        slope=2*pi*freq/343
        sfgrad,pres,,x,0,slope
        nsel,s,loc,z,,0
        sf,all,pres,0               !apply pressure
        allsel,all
```

```
*endif
allsel,all

SOLVE
FINISH

/POST1
SET,LIST,2              ! List Modes
SET,FIRST               ! Display first mode
PLDISP,0                ! Displacement of first mode

!!!!! find short-circuit charge (Qsc) on each pair of electrodes

!!!!!!!!!!! Mode #1
/com,
/com, Electrode short-circuit charge results (mode #1):

*get,Qsc1,node,top1,rf,chrg
/com, - Electrode 1:  Qsc = %Qsc1% [C]

*get,Qsc2,node,top2,rf,chrg
/com, - Electrode 2:  Qsc = %Qsc2% [C]

*get,Qsc3,node,top3,rf,chrg
/com, - Electrode 3:  Qsc = %Qsc3% [C]

*get,Qsc4,node,top4,rf,chrg
/com, - Electrode 4:  Qsc = %Qsc4% [C]

*get,psi_tip3,node,ntip,u,z                    !psi at beam end
/com
/com, - psi at beam end (mode #1) = %psi_tip3%

!!! Find psi (modeshape) values along spring
*dim,SMS,array,div+1   ! array to store spring modeshape values

*do,i,1,div+1
        *get,SMS(i),node,x_nodes(i),u,z          ! Get modeshape value at node
*enddo

/com
/com spring_psi values =
*do,i,1,div+1
        /com node # = %x_nodes(i)%
        /com x = %s_loc(i)%  psi_val = %SMS(i)%
*enddo
```

```
/com
!!!!!!!!!!! Mode #2
SET,next                    ! Display 2nd mode

/com,
/com, Electrode short-circuit charge results (mode #2):

*get,Qsc1a,node,top1,rf,chrg
/com, - Electrode 1:  Qsc = %Qsc1a% [C]

*get,Qsc2a,node,top2,rf,chrg
/com, - Electrode 2:  Qsc = %Qsc2a% [C]

*get,Qsc3a,node,top3,rf,chrg
/com, - Electrode 3:  Qsc = %Qsc3a% [C]

*get,Qsc4a,node,top4,rf,chrg
/com, - Electrode 4:  Qsc = %Qsc4a% [C]

*get,psi_tip3,node,ntip,u,z                    !psi at beam end
/com
/com, - psi at beam end (mode #2) = %psi_tip3%


!!! Find psi (modeshape #2) values along spring
*dim,SMS2,array,div+1 ! array to store spring modeshape values

*do,i,1,div+1
        *get,SMS2(i),node,x_nodes(i),u,z              ! Get modeshape value at node
*enddo
/com
/com spring_psi values =
*do,i,1,div+1
        /com node # = %x_nodes(i)%
        /com x = %s_loc(i)%  psi_val = %SMS2(i)%
*enddo
/com

!!!!!!!!!!! Mode #3
SET,next                    ! Display 3rd mode

/com,
/com, Electrode short-circuit charge results (mode #3):

*get,Qsc1b,node,top1,rf,chrg
/com, - Electrode 1:  Qsc = %Qsc1b% [C]
```

```
*get,Qsc2b,node,top2,rf,chrg
/com, - Electrode 2:  Qsc = %Qsc2b% [C]

*get,Qsc3b,node,top3,rf,chrg
/com, - Electrode 3:  Qsc = %Qsc3b% [C]

*get,Qsc4b,node,top4,rf,chrg
/com, - Electrode 4:  Qsc = %Qsc4b% [C]

*get,psi_tip3,node,ntip,u,z                    !psi at beam end
/com
/com, - psi at beam end (mode #3) = %psi_tip3%

!!!!!!!!!!! Mode #4
SET,next                ! Display 4th mode

/com,
/com, Electrode short-circuit charge results (mode #4):

*get,Qsc1c,node,top1,rf,chrg
/com, - Electrode 1:  Qsc = %Qsc1c% [C]

*get,Qsc2c,node,top2,rf,chrg
/com, - Electrode 2:  Qsc = %Qsc2c% [C]

*get,Qsc3c,node,top3,rf,chrg
/com, - Electrode 3:  Qsc = %Qsc3c% [C]

*get,Qsc4d,node,top4,rf,chrg
/com, - Electrode 4:  Qsc = %Qsc4d% [C]

*get,psi_tip4,node,ntip,u,z                    !psi at beam end
/com
/com, - psi at beam end (mode #4) = %psi_tip4%

!!!!!!!!!!! Mode #5
SET,next                                       ! Display 4th mode

/com,
/com, Electrode short-circuit charge results (mode #5):

*get,Qsc1_m5,node,top1,rf,chrg
/com, - Electrode 1:  Qsc = %Qsc1_m5% [C]

*get,Qsc2_m5,node,top2,rf,chrg
/com, - Electrode 2:  Qsc = %Qsc2_m5% [C]
```

```
*get,Qsc3_m5,node,top3,rf,chrg
/com, - Electrode 3:  Qsc = %Qsc3_m5% [C]

*get,Qsc4_m5,node,top4,rf,chrg
/com, - Electrode 4:  Qsc = %Qsc4_m5% [C]

*get,psi_tip3,node,ntip,u,z                    !psi at beam end
/com
/com, - psi at beam end (mode #5) = %psi_tip3%
allsel,all
finish
```

```
! Import geometry from iges file
! External-beam dual differential microphone
! distances in um

finish
/clear, nostart
/filename, DVM_ext_beam_type_1

! Import iges file
/aux15
ioptn,iges,nodefeat
ioptn,merge,yes
ioptn,solid,yes
ioptn,small,yes
ioptn,gtoler,defa
igesin,'Ansys_Ext_DVM_Jan_2011','igs','Desktop\'
lplot
/PNUM,LINE,1
/REPLOT
finish

/PREP7
!btol,0.05e-5
Po=101325*1e-6
ES=5
nummode=2                    ! number of modes to solve for

!Define layer thickness
p1=1                         !Poly 1
p2=1.5                       !Poly 2
p3=2.25                          !Poly 3
p4=2.25                          !Poly 4
s2=0.3                       !Saccox 2
s3=2                         !Saccox 3
s4=2                         !Saccox 4

!Material Properties
ET,1,solid187                ! poly Si
ET,2,solid187                ! oxide
mp,ex,1,160e3                ! Youngs modulus of Poly Si
mp,dens,1,2.33e-15           ! density PolySi
mp,nuxy,1,0.23               ! poisson's ration PolySi

AL,1,2                       !Left diaphragm          !A1
AL,27,28                     !Right diaphragm                 !A2
```

```
AL,13,14,15,16,17,18,19          !Top left P1 beam                !A3
AL,20,21,22,16,24,25,26          !lower left P1 beam              !A4
AL,39,40,41,42,17,44,45          !Top right P1 beam               !A5
AL,46,47,48,42,24,51,52          !Lower right P1 beam             !A6
AL,3,4                           !Left post                       !A7
AL,37,38                         !Right post                      !A8
AL,5,6,7,8,9,10,11,12            !Left top beam                   !A9
AL,29,30,31,32,24,17,34,35,36    !Right top beam                  !A10

!Add beam areas
aadd,3,4,5,6                     !Lower beam                      !A11
aadd,9,10                        !Upper beam                      !A3
vplot
/pnum,line,0
/pnum,volu,1
/replot

! Extrude diaphragms
vext,1,2,1,,,-p1          !V1,2

! Extrude Lower Beam Surfaces
vext,11,,,,,-p1                  !Poly1                           !V3, Poly1
vext,11,,,,,p2                   !P2                              !V4
/view,,0,-1,0
/REP

! Extrude upper beam surfaces
vext,3,,,,,p2+p3+p4              !All Layers                      !v5
vext,3,,,,,p2                    !All but p4                      !V6
vsbv,5,6                         !Poly 3&4 layer          !V7
/replot

! Extrude posts
vext,7,,,,,p2             !V
vext,8,,,,,p2             !V

! Create pivot
k,1001,-0.5,194.5,-p1            !Corners of pivot
k,1002,0.5,194.5,-p1
k,1003,0.5,-194.5,-p1
k,1004,-0.5,-194.5,-p1
k,1005,0,194.5,-p1-0.5    !point of pivot
k,1006,0,-194.5,-p1-0.5
A,1001,1002,1005                 !A61
A,1003,1004,1006                 !A62
A,1001,1002,1003,1004!A63
A,1002,1003,1006,1005!A64
```

```
A,1001,1004,1006,1005!A65
VA,61,62,63,64,65
allsel,all
vadd,all
allsel,all

! Mesh
type,1
mat,1
MSHAPE,1,3d                    ! 0-quad, 1-triangular
esize,ES
VMESH,all

!Apply Boundary conditions
asel,s,,,5
asel,a,,,6
asel,a,,,10
asel,a,,,12
DA,all,all,0
allsel,all

!!!!!!!!!!!!!!!!!!!!!!!!!!!!!!!!!!!!!!!!!!!!!!!!!!!!!!!!
!!!!!!!!!!!!! 1st Static Analysis, before pivot touchdown !!!!!!!!!!!!!
!Apply pressure

/sol
allsel,all
asel,s,,,4
asel,a,,,9
SFA,all,1,pres,-Po*0.185
allsel,all
antype,0                ! Static analysis
nlgeom,on               ! Large deformation and large strain
pstres,off
solve
allsel,all
asel,s,,,4
nsla,s,1

*get,num_nodes,node,0,count
*get,lowest_node,node,0,num,min
*dim,def1,array,num_nodes
sum1=0
current_node=lowest_node

*do,i,1,num_nodes
        *get,node_def,node,current_node,u,z
```

```
        def1(i)=node_def
        sum1=sum1+node_def
        *get,next_node,node,current_node,nxth
        current_node=next_node
        /com node_def=%def1(i)%
*enddo

def1_avg=sum1/num_nodes
/com def1_avg=%def1_avg%
finish
/post1
/EFACET,1
PLNSOL, U,z, 0,1.0

!!!!!!!! 2nd static nonlinear analysis (after pivot touchdown) !!!!!!!!!!!!!!!
finish
/sol
allsel,all
DL,147,,uz,0
DL,147,,ux,0
DL,147,,uy,0
allsel,all

sfadele,all,1,all
asel,s,,,4
asel,a,,,9
SFA,all,1,pres,-Po*0.815
allsel,all

antype,0                ! Static analysis
upcoord,1,on
nlgeom,on               ! Large deformation and large strain
pstres,on
solve

allsel,all
asel,s,,,4
nsla,s,1
*dim,def2,array,num_nodes
*dim,def_tot,array,num_nodes
sum2=0
sum_tot=0
current_node=lowest_node

*do,i,1,num_nodes
        *get,node_def,node,current_node,u,z
        def2(i)=node_def
```

```
        sum2=sum2+node_def
        *get,next_node,node,current_node,nxth
        current_node=next_node
        /com node_def=%def2(i)%
        def_tot(i)=def1(i)+def2(i)
        sum_tot=def_tot(i)+sum_tot
        /com def_tot=%def_tot(i)%
*enddo

def1_avg=sum1/num_nodes
def2_avg=sum2/num_nodes
def_tot_avg=sum_tot/num_nodes

/com def2_avg=%def2_avg%
/com def_tot_avg=%def_tot_avg%
*vscfun,max_tot_def,min,def_tot
/com max_tot_def=%max_tot_def%
finish
/post1
/EFACET,1
PLNSOL, U,SUM, 0,1.0

!!!!!!!!!!!!!!!!!!!!!!!!!!!!!!!!!!!!!!!!!!!!!!!!!!!
!!!!!!!!Modal Perturbation Analysis!!!!!!!!!!!!!!
/solu
/com    FIRST PHASE OF LINEAR PERTURBATION
antype,,restart,,,perturb  ! Restart at highest substep,
                                    ! from the base nonlinear static analysis
perturb,modal
solve,elform                ! Execute 1st phase of linear perturbation, recovering Kt of NLGEOM,on

/com    SECOND PHASE OF LINEAR PERTURBATION

modopt,lanb,nummode   ! Solve for lowest 3 modes by using block Lanczos
mxpand,nummode,,,yes   ! Expand mode the same time
outres,esol,all
solve          ! Execute 2nd phase of linear perturbation: modal analysis
fini
/post1
file,,rstp
set,list
set,last
```

Appendix B: Matlab Scripts

Multiple-mode model applied to piezoelectric microphone

```
clear all; close all; clc;

f=linspace(10,1e5,10000); om=2*pi*f;
% Device parameters and constants (Device-1)
we=105e-6;          % electrode width
le=424e-6;          % electrode length
t_pzt=1.05e-6;      % pzt thickness

% constants
eps=8.85e-12;       % permittivity of free space
eps_r=657;          % relative permittivity of pzt (measured)
tan_del=0.04;       % tan delta (Gab. notes, PZT5H)

% input PZT leakage resistance%
Ae=le*we;                                   % electrode area [m^2]
% Ceb = eps*eps_r*Ae/t_pzt;                 % PZT stack capacitance [C]
Ceb=280e-12;                                % measured PZT capacitance
RL=1./(tan_del.*om.*Ceb);                   % Parallel leakage resistance [ohms]

%%% input damping ratio
Q1=11938.48/(39.55+32.23)                   % from epoxied prototype
Q2=17948.73/(92.29+76.17)
zeta1=1/(2*Q1)
zeta2 = 1/(2*Q2);

%%% input phi (modal Qsc, from ANSYS - electrode #4)%
phi1 = 0.1045*0.4;
phi2 = 0.1101*0.4;

%input res freq (from ANSYS)
f1 = 13.9e3;    %mode #1
f2 = 17.9e3;    %mode #2
om1=2*pi*f1; om2 = 2*pi*f2;

%%% common-mode loading eta_dc for each mode %%%%
%%% From ANSYS MSUP (XY_MSUP_dc.MCF)
eta1_cm = -0.3073e-15;          % mode 1
eta2_cm = -0.49387e-12;         % mode 2

%%% gradient loading eta for each mode %%%%
%%% eta for differential loading case will have linear freq dependence)
eta1_grad = (0.14675e-13)/1000;     % mode 1
```

```
eta2_grad = (-0.29187e-17)/1000;      % mode 2

%calculate model forces%
F1_cm=eta1_cm*om1^2;                  % common-mode component of modal force
F2_cm=eta2_cm*om2^2;

F1_grad=eta1_grad.*f.*om1^2;          % differential component of modal force
F2_grad=eta2_grad.*f.*om2^2;

F1=F1_cm+j*F1_grad;
F2=F2_cm+j*F2_grad;

% compute etas%
n1=F1./(om1^2-om.^2+2*j*zeta1*om1*om);
n2=F2./(om2^2-om.^2+2*j*zeta2*om2*om);

% Equivalent Electrical Impedance
Ze = (1./(j*om*Ceb)).*RL./((1./(j*om*Ceb))+RL);

% Mass
m = 1;

% Mechanical Compliance
Cm1 = 1/(m*om1^2);
Cm2 = 1/(m*om2^2);

% Mechanical Resistance
Rm1 = 2*zeta1*om1*m;
Rm2 = 2*zeta2*om2*m;

% Equivalent Mechanical Impedance
Zm1 = j*om*m + 1./(j*om*Cm1) + Rm1;
Zm2 = j*om*m + 1./(j*om*Cm2) + Rm2;

% Open Circuit Voltage as a function of input Force TF
Voc1= (F1./phi1).*Ze./(Ze + Zm1/phi1^2);
Voc2= (F2./phi2).*Ze./(Ze + Zm2/phi2^2);
VocTot = Voc1 + Voc2;

figure(1)
loglog(f,abs(Voc1),'b',f,abs(Voc2),'r',f,abs(VocTot),'k')
title('Acoustic Frequency Response')
xlabel('frequency (Hz)')
ylabel('Open-Circuit Sensitivity (V/Pa)')
legend('mode 1 contrib','mode 2 contrib','total',2)
grid on
pedit
```

References

[1] P. R. Scheeper, A. G. H. van der Donk, W. Olthuis, and P. Bergveld, "A review of silicon microphones," *Sens. Actuators A, Phys.,* vol. 44, pp. 1-11, 1994.

[2] M. Royer, J. O. Holmen, M. A. Wurm, O. S. Aadland, and M. Glenn, "ZnO on Si integrated acoustic sensor," *Sens. Actuators,* vol. 4, pp. 357-362, 1983.

[3] D. Holm and G. M. Sessler, "An integrated silicon-electret condenser microphone," presented at the Proc. 11th Int. Congr. Acoustics, Paris, France, 1983.

[4] G. M. Sessler, "Acoustic sensors," *Sens. Actuators A, Phys.,* vol. 25-27, pp. 323-330, 1991.

[5] J. Bouchaud, "MEMS microphones: The digital revolution," IHS iSuppli Corporation, El Segundo, CA, 2011.

[6] J. Eargle, *The Microphone Book*, 2nd ed. Jordan Hill, Oxford: Elsevier, 2004.

[7] P. Loeppert and S. B. Lee, "SiSonic^{TM} - The first commercialized MEMS microphone," presented at the Solid-State Sensors, Actuators, and Microsystems Workshop, Hilton Head, SC, 2006.

[8] A. Dehe, M. Wurzer, M. Fuldner, and U. Krumbein, "The Infineon silicon MEMS microphone," presented at the AMA Conf. 2013 - SENSORS 2013, Nuremberg, Germany, 2013.

[9] A. Dehe, "Silicon microphone development and application," *Sens. Actuators A, Phys.,* vol. 133, pp. 283-287, 2007.

[10] G. W. Elko and K. P. Harney, "A history of consumer microphones: The electret condenser microphone meets micro-electro-mechanical systems," *Acoust. Today*. pp. 4-13, Apr. 2009.

[11] T. B. Gabrielson, "Mechanical-thermal noise in micromachined acoustic and vibration sensors," *IEEE Trans. Electron Devices,* vol. 40, pp. 903-909, 1993.

[12] S. C. Thompson, J. L. LoPresti, E. M. Ring, H. G. Nepomuceno, J. J. Beard, W. J. Ballad, and E. V. Carlson, "Noise in miniature microphones," *J. Acoust. Soc. Amer.,* vol. 111, pp. 861-866, 2002.

[13] A. M. Amlani, B. Rakerd, and J. L. Punch, "Speech-clarity judgements of hearing-aid-processed speech in noise: differing polar patterns and acoustic environments," *Int. J. Audiology,* vol. 45, pp. 319-330, 2006.

[14] P. J. Blamey, H. J. Fiket, and B. R. Steele, "Improved speech intelligibility in background noise with an adaptive directional microphone," *J. Amer. Academy Audiology,* vol. 17, pp. 519-530, 2006.

[15] B. W. Y. Hornsby and T. A. Ricketts, "Effects of noise source configuration on directional benefit using symmetric and asymmetric directional hearing aid fittings," *Ear & Hearing,* vol. 28, pp. 177-186, 2007.

[16] T. Ricketts, P. Henry, and D. Gnewikow, "Full time directional verses user selectable microphone modes in hearing aids," *Ear & Hearing,* vol. 24, pp. 424-439, 2003.

[17] G. Cauwenberghs, A. Andreou, J. West, M. Stanacevic, A. Celik, P. Julian, T. Teixeira, C. Diehl, and L. Riddle, "A miniature low-power intelligent sensor node for persistent acoustic surveillance," in *Proc. SPIE*, 2005, vol. 5796, pp. 294-305.

[18] M. Stanacevic and G. Cauwenberghs, "Micropower gradient flow acoustic localizer," *IEEE Trans. Circuits Syst. I, Reg. Papers,* vol. 52, pp. 2148-2157, 2005.

[19] A. G. Andreou, D. H. Goldberg, E. Culurciello, M. Stanacevic, G. Cauwenberghs, and L. Riddle, "Heterogeneous integration of biomimetic acoustic microsystems," in *IEEE Int. Symp. Circuits Syst.,* 2001, vol. 2, pp. 189-192.

[20] R. N. Miles, D. Robert, and R. R. Hoy, "Mechanically coupled ears for directional in the parasitoid fly *Ormia ochracea*," *J. Acoust. Soc. Amer.,* vol. 98, pp. 3059-3070, 1995.

[21] C. Gibbons and R. Miles, "Design of a biomimetic directional microphone diaphragm," presented at the Proc. Int. Mechanical Engineering Cong. and Exp., Orlando, FL, 2000.

[22] K. Yoo, C. Gibbons, Q. T. Su, R. N. Miles, and N. C. Tien, "Fabrication of biomimetic 3-D structured diaphragms," *Sens. Actuators A, Phys.,* vol. 97–98, pp. 448-456, 2002.

[23] R. N. Miles, Q. Su, W. Cui, M. Shetye, F. L. Degertekin, B. Bicen, C. Garcia, S. Jones, and N. Hall, "A low-noise differential microphone inspired by the ears of the parasitoid fly Ormia ochracea," *J. Acoust. Soc. Amer.,* vol. 125, pp. 2013-2026, 2009.

[24] W. Cui, B. Bicen, N. Hall, S. Jones, F. L. Degertekin, and R. N. Miles, "Optical sensing in a directional MEMS microphone inspired by the ears of the parasitoid fly, Ormia Ochracea," presented at MEMS 2006, Istanbul, Turkey, 2006.

[25] B. Bicen, S. Jolly, K. Jeelani, C. T. Garcia, N. A. Hall, F. L. Degertekin, Q. Su, W. Cui, and R. N. Miles, "Integrated optical displacement detection and electrostatic actuation for directional optical microphones with micromachined biomimetic diaphragms," *IEEE Sensors J.,* vol. 9, pp. 1933-1941, 2009.

[26] H. J. Liu, M. Yu, and X. M. Zhang, "Biomimetic optical directional microphone with structurally coupled diaphragms," *Appl. Physics Lett.,* vol. 93, pp. 243902-3, 2008.

[27] H. Liu, L. Currano, D. Gee, T. Helms, and M. Yu, "Understanding and mimicking the dual optimality of the fly ear," *Sci. Rep.,* vol. 3, 2013.

[28] M. Touse, J. Sinibaldi, and G. Karunasiri, "MEMS directional sound sensor with simultaneous detection of two frequency bands," in *IEEE Sensors*, 2010, pp. 2422-2425.

[29] M. Touse, J. Sinibaldi, K. Simsek, J. Catterlin, S. Harrison, and G. Karunasiri, "Fabrication of a microelectromechanical directional sound sensor with electronic readout using comb fingers," *Appl. Physics Lett.,* vol. 96, pp. 173701-3, 2010.

[30] M. L. Kuntzman and N. A. Hall, "Rotational capacitive micromachined ultrasonic transducers (cMUTs)," *J. Microelectromech. Syst.,* vol. 23, pp. 1-3, 2014.

[31] S. Po-Hsun, C. Jen-Yi, Y. Kai-hsiang, and W. Chia-Yu, "CMOS compatible directional microphone," in *Int. Microsystems, Packaging, Assembly and Circuits Tech.,* 2007, pp. 149-152.

[32] S. Ando, T. Kurihara, K. Watanabe, Y. Yamanishi, and T. Ooasa, "Novel theoretical design and fabrication test of biomimicry directional microphone," in *Int. Solid-State Sensors, Actuators and Microsystems Conf.,* 2009, pp. 1932-1935.

[33] A. P. Lisiewski, H. J. Liu, M. Yu, L. Currano, and D. Gee, "Fly-ear inspired micro-sensor for sound source localization in two dimensions," *J. Acoust. Soc. Amer.,* vol. 129, pp. EL166-EL171, 2011.

[34] M. L. Kuntzman, C. T. Garcia, A. G. Onaran, B. Avenson, K. D. Kirk, and N. A. Hall, "Performance and modeling of a fully packaged micromachined optical microphone," *J. Microelectromech. Syst.,* vol. 20, pp. 828-833, 2011.

[35] M. L. Kuntzman, "Modeling and prototyping of a micromachined optical microphone," M.S.E. Thesis, Dept. Elect. Comput. Eng., Univ. Texas, Austin, TX, 2010.

[36] N. A. Hall, M. L. Kuntzman, and K. D. Kirk, "Differential microphone with sealed backside cavities and diaphragms coupled to a rocking structure thereby providing resistance to deflection under atmospheric pressure and providing a directional response to sound pressure," U.S. Patent Applicat. 13/441,079, Apr. 6, 2012.

[37] N. A. Hall, M. L. Kuntzman, D. Kim, and N. Hewa-Kasakarage, "Acoustic sensor," U.S. Patent Applicat. PCT/US2013/054572, Aug. 12, 2013.

[38] M. L. Kuntzman, J. Gloria Lee, N. N. Hewa-Kasakarage, D. Kim, and N. A. Hall, "Micromachined piezoelectric microphones with in-plane directivity," *Appl. Physics Lett.,* vol. 102, pp. 054109-4, 2013.

[39] D. Kim, N. N. Hewa-Kasakarage, M. L. Kuntzman, K. D. Kirk, S. H. Yoon, and N. A. Hall, "Piezoelectric micromachined microphones with out-of-plane directivity," *Appl. Physics Lett.,* vol. 103, pp. 013502-5, 2013.

[40] D. Kim, N. N. Hewa-Kasakarage, S. Yoon, and N. A. Hall, "On the minimum coupling required for maximum theoretical power capture from vibration energy harvesters," *Appl. Physics Lett.,* vol. 101, pp. 103904-3, 2012.

[41] N. N. Hewa-Kasakarage, D. Kim, M. L. Kuntzman, and N. A. Hall, "Micromachined piezoelectric accelerometers via epitaxial silicon cantilevers and bulk silicon proof masses," *J. Microelectromech. Syst.,* vol. 22, pp. 1438-1446, 2013.

[42] S. Horowitz, T. Nishida, L. Cattafesta, and M. Sheplak, "Development of a micromachined piezoelectric microphone for aeroacoustics applications," *J. Acoust. Soc. Amer.,* vol. 122, pp. 3428-3436, 2007.

[43] H. J. Zhao, T. L. Ren, J. S. Liu, L. T. Liu, and Z. J. Li, "Fabrication of high-quality PZT-based piezoelectric microphone," presented at the The 12th Int. Conf. Solid State Sensors, Actuators and Microsystems, Boston, 2003.

[44] E. S. Kim and R. S. Muller, "IC-Processed piezoelectric microphone," *IEEE Electron Device Lett.,* vol. 8, pp. 467-468, 1987.

[45] E. S. Kim, R. S. Muller, and P. R. Gray, "Integrated microphone with CMOS circuits on a single chip," presented at the Int. Electron Devices Meeting, Washington DC, 1987.
[46] M. D. Williams, B. A. Griffin, T. N. Reagan, J. R. Underbrink, and M. Sheplak, "An AlN MEMS piezoelectric microphone for aeroacoustic applications," *J. Microelectromech. Syst.,* vol. 21, pp. 270-283, 2012.
[47] R. Littrell and K. Grosh, "Modeling and characterization of cantilever-based mems piezoelectric sensors and actuators," *J. Microelectromech. Syst.,* vol. 21, pp. 406-413, 2012.
[48] R. Schellin, G. Hess, W. Kuehnel, G. M. Sessler, and E. Fakada, "Silicon subminiature microphones with organic piezoelectric layers," *IEEE Trans. Elect. Insulation,* vol. 27, pp. 867-871, 1992.
[49] V. Fuflyigin, E. Salley, A. Osinsky, and P. Norris, "Pyroelectric properties of AlN," *Appl. Physics Lett.,* vol. 77, pp. 3075-3077, 2000.
[50] G. Heiland and H. Ibach, "Pyroelectricity of zinc oxide," *Solid State Commun.,* vol. 4, pp. 353-356, 1966.
[51] *IEEE Standard on Piezoelectricity*, ANSI/IEEE Standard 176-1987*,* 1988.
[52] M. L. Kuntzman, D. Kim, N. N. Hewa-Kasakarage, K. D. Kirk, and N. A. Hall, "Network modeling of multiple-port, multiple-vibration-mode transducers and resonators," *Sens. Actuators A, Phys.,* vol. 201, pp. 93-100, 2013.
[53] K. E. Wojciechowski, R. H. Olsson, M. R. Tuck, E. Roherty-Osmun, and T. A. Hill, "Single-chip precision oscillators based on multi-frequency, high-q aluminum nitride MEMS resonators," presented at Transducers 2009, Denver, CO, 2009.
[54] G. Piazza, R. Abdolvand, G. K. Ho, and F. Ayazi, "Voltage-tunable piezoelectrically-transduced single-crystal silicon micromechanical resonators," *Sens. Actuators A, Phys.,* vol. 111, pp. 71-78, 2004.
[55] G. Piazza, P. J. Stephanou, and A. P. Pisano, "One and two port piezoelectric high order contour-mode MEMS resonsators for mechanical signal processing," *Solid-State Electron.,* vol. 51, pp. 1596-1608, 2007.
[56] P. J. Stephanou and A. P. Pisano, "GHz contour extensional mode aluminum nitride MEMS resonators," *IEEE Ultrasonics Symp.,* pp. 2401-2404, 2006.
[57] R. H. Olsson, K. E. Wojciechowski, M. S. Baker, M. R. Tuck, and J. G. Fleming, "Post-CMOS-compatible aluminium nitride resonant mems accelerometers," *J. Microelectromech. Syst.,* vol. 18, pp. 671-678, 2009.
[58] R. O. Guldiken, J. Zahorian, F. Yamaner, and F. Degertekin, "Dual-electrode CMUT with non-uniform membranes for high electromechanical coupling coefficient and high bandwidth operation," *IEEE Trans. Ultrason. Ferroelectr. Freq. Control,* vol. 56, pp. 1270-1276, 2009.
[59] R. O. Guldiken, M. Balantekin, J. Zahorian, and F. Degertekin, "Characterization of dual-electrode CMUTs: demonstration of improved receive performance and pulse echo operation with dynamic membrane shaping," *IEEE Trans. Ultrason., Ferroelectr. Freq. Control,* vol. 55, pp. 2336-2344, 2008.

[60] R. O. Guldiken, J. McLean, and F. Degertekin, "CMUTS with dual electrode structure for improved transmit and receive performance," *IEEE Trans. Ultrason., Ferroelectr. Freq. Control,* vol. 53, pp. 483-491, 2006.
[61] N. A. Hall, R. O. Guldiken, J. McLean, and F. L. Degertekin, "Modeling and design of CMUTs using higher order vibration modes," presented at the IEEE Ultrasonics Symp., 2004.
[62] C. Lu, M. Lemkin, and B. E. Boser, "A monolithic surface micromachined accelerometer with digital output," presented at the IEEE Int. Solid-State Circuits Conf., 1995.
[63] J. Chae, H. Kulah, and K. Najafi, "A monolithic three-axis micro-g micromachined silicon capacitive accelerometer," *J. Microelectromech. Syst.,* vol. 14, pp. 235-242, 2005.
[64] N. C. Loh, M. A. Schmidt, and S. R. Manalis, "Sub-10 cm^3 interferometric accelerometer with nano-g resolution," *J. Microelectromech. Syst.,* vol. 11, pp. 182-187, 2002.
[65] C.-H. Liu and T. W. Kenny, "A high-precision, wide-bandwidth micromachined tunneling accelerometer," *J. Microelectromech. Syst.,* vol. 10, pp. 425-433, 2001.
[66] J. H. Ginsberg, *Mechanical and Structural Vibrations: Theory and Applications*. New York: John Wiley & Sons, 2001.
[67] V. B. Bokil and U. S. Shirahatti, "A Technique for the modal analysis of sound-structure interaction problems," *J. Sound and Vibration,* vol. 173, pp. 23-41, 1994.
[68] F. Daneshmand and E. Ghavanloo, "Coupled free vibration analysis of a fluid-filled rectangular container with a sagged bottom membrane," *J. Fluids Structures,* vol. 26, pp. 236-252, 2010.
[69] H. A. C. Tilmans, "Equivalent circuit representation of electromechanical transducers: I. Lumped-parameter systems," *J. Micromech. Microeng.,* vol. 6, pp. 157-176, 1996.
[70] H. A. C. Tilmans, "Equivalent circuit representation of electromechanical transducers: II. Distributed-parameter systems," *J. Micromech Microeng.,* vol. 7, pp. 285-309, 1997.
[71] S. Roundy, "On the effectiveness of vibration-based energy harvesting," *J. Intelligent Materials Syst. Structures,* vol. 16, pp. 809-823, 2005.
[72] S. B. Horowitz, M. Sheplak, L. N. Cattafesta, and T. Nishida, "A MEMS acoustic energy harvester," *J. Micromech. Microeng.,* vol. 16, pp. 174-181, 2006.
[73] M. Ferrari, V. Ferrari, D. Marioli, and A. Taroni, "Modeling, fabrication and performance measurements of a piezoelectric energy converted for power harvesting in autonomous microsystems," *IEEE Trans. Instrum. Meas.,* vol. 55, pp. 2096-2101, 2006.
[74] A. Erturk and D. J. Inman, *Piezoelectric Energy Harvesting*: Chirchester: John Wiley & Sons, 2011.

[75] D. Kim, N. N. Hewa-Kasakarage, S. H. Yoon, K. D. Kirk, M. Kuntzman, and N. A. Hall, "Electrical admittance spectroscopy for piezoelectric MEMS," *J. Microelectromech. Syst.,* vol. 22, pp. 295-302, 2013.

[76] S. Trolier-McKinstry and P. Muralt, "Thin film piezoelectrics for MEMS: Special issue on electroceramics in micro-electro-mechanical systems (Guest Editor: Nava Setter)," *J. Electroceramics,* vol. 12, pp. 7-17, 2004.

[77] T. Gabrielson, B., "Mechanical-thermal noise in micromachined acoustic and vibration sensors," *IEEE Trans. Electron Devices,* vol. 40, pp. 903-909, 1993.

[78] D. T. Martin, J. Liu, K. Kadirvel, R. M. Fox, M. Sheplak, and T. Nishida, "A Micromachined Dual-Backplate Capacitive Microphone for Aeroacoustic Measurements," *J. Microelectromech. Syst.,* vol. 16, pp. 1289-1302, 2007.

[79] M. L. Kuntzman and N. A. Hall, "A broadband, capacitive, surface-micromachined, omnidirectional microphone with more than 200 kHz bandwidth," *J. Acoust. Soc. Amer.*, to be published.

[80] H. Nyquist, "Thermal agitation of electric charge in conductors," *Physical Review,* vol. 32, pp. 110-113, 1928.

[81] T. B. Gabrielson, "Mechanical-thermal noise in micromachined acoustic and vibration sensors," *IEEE Trans. Electron Devices,* vol. 40, pp. 903-909, May 1993.

[82] M. Füldner and A. Dehé, "Challenges of high SNR (signal-to-noise) silicon micro machined microphones," in *Proc. 19th Int. Congr. Acoust., Madrid*, 2007, pp. 1-6.

[83] J. Zahorian, M. Hochman, T. Xu, S. Satir, G. Gurun, M. Karaman, and F. Degertekin, "Monolithic CMUT-on-CMOS integration for intravascular ultrasound applications," *IEEE Trans. Ultrason. Ferroelectr. Freq. Control,* vol. 58, pp. 2659-2667, 2011.

[84] G. Gurun, P. Hasler, and F. L. Degertekin, "Front-end receiver electronics for high-frequency monolithic CMUT-on-CMOS imaging arrays," *IEEE Trans. Ultrason. Ferroelectr. Freq. Control,* vol. 58, pp. 1658-1668, 2011.

[85] S. T. Hansen, A. S. Ergun, W. Liou, B. A. Auld, and B. T. Khuri-Yakub, "Wideband micromachined capacitive microphones with radio frequency detection," *J. Acoust. Soc. Amer.,* vol. 116, pp. 828-842, 2004.

[86] W. Cade, "Acoustically orienting parasitoids: fly phonotaxis to cricket song," *Sci.,* vol. 190, pp. 1312-1313, Dec. 1975.